Magnetic trapping of molecules via optical loading and magnetic slowing

Citation

Lu, Hsin-I. 2013. Magnetic trapping of molecules via optical loading and magnetic slowing. Doctoral dissertation, Harvard University.

Magnetic trapping of molecules via optical loading and magnetic slowing

A dissertation presented
by

Hsin-I Lu

to
The School of Engineering and Applied Sciences
in partial fulfillment of the requirements
for the degree of
Doctor of Philosophy
in the subject of

Applied Physics

Harvard University
Cambridge, Massachusetts
November 2013

Dissertation advisor Author

John M. Doyle **Hsin-I Lu**

Magnetic trapping of molecules via optical loading and magnetic slowing

Abstract

This thesis demonstrates a new cooling and trap loading technique for molecules, leading to trapping of calcium monofluoride (CaF). Two key principles developed and used are a very slow molecular beam and irreversible loading of a magnetic trap via optical pumping. The cooling of molecules occurs inside a cryogenic buffer-gas cell, where collisions between the molecules and cold, inert buffer gas cool the initially hot molecules. Cold molecules emitted out the cell through an exit aperture enter another slowing cell with a piece of mesh on the final exit aperture. Such a two-stage cell provides slow monohydride (CaH) molecules with a moving velocity of 60 m/s and a flux of 10^9 molecules/pulse. This technique is completely general, and is applied to produce slow beams of atomic potassium and CaF. We direct a slow CaF beam with $v_f = 55$ m/s (velocity width of 45 m/s) into a magnetic trap. The molecular velocity is further decelerated by the magnetic fields to within the capture range of the trap. To achieve irreversible trap loading, we employ two-stage optical pumping near both the trap saddle and the trap center to flip the electronic spin projection of the molecules. With the scattering of two photons, we magnetically trap CaF in its first rotational excited state, $N = 1$, with a trap lifetime exceeding 500 ms. Trajectory simulations are developed to optimize the loading process and simulate the loss of trapped molecules. The attained trap lifetime is limited by elastic collisions with the background ^{3}He gas at a density of 5×10^{10} cm^{-3}. Using this new loading method, we also realized trapping of CaF ($N = 0$) and CaH ($N = 0$). This work provides the platform for future work. We plan to co-load CaH molecules with Li atoms to study cold collisions and cold controlled chemistry inside the trap, which may shed the light on further cooling of molecules using Li as the coolant. Laser cooling of trapped CaF ($N = 1$) may be feasible inside the trap. Magnetic trapping of chemically diverse molecules without closed cycling transitions, including triatomic molecules, may be realized with the scattering of only a few photons.

Contents

Citations to previously published work

Parts of this dissertation cover research reported in the following articles:

1. *Magnetic Trapping of Molecules via Optical Loading and Magnetic Slowing*, H.-I Lu, I. Kozyryev, B. Hemmerling, J. Piskorski, and J. M. Doyle, arXiv:1310.2669 [physics.atom-ph], submitted to PRL (2013).
2. *Spin-Orbit Suppression of Cold Inelastic Collisions of Aluminum and Helium*, C. B. Connolly, Y. S. Au, E. Chae, T. V. Tscherbul, A. A. Buchachenko, H.-I Lu, W. Ketterle, and J. M. Doyle, Phys. Rev. Lett. **17**, 173202 (2013).
3. *The Buffer Gas Beam: An Intense, Cold, and Slow Source for Atoms and Molecules*, N. R. Hutzler, H.-I Lu, and J. M. Doyle, Chem. Rev. **112**, 4803 (2012).
4. *A Cold and Slow Molecular Beam*, H.-I Lu, J. Rasmussen, M. J. Wright, D. Patterson, and J. M. Doyle, Phys. Chem. Chem. Phys. **13**, 18986 (2011).
5. *Cold N+NH Collisions in a Magnetic Trap*, M. H. Hummon, T. V. Tscherbul, J. Kłos, H.-I Lu, E. Tsikata, W. C. Campbell, A. Dalgarno, J. M. Doyle, Phys. Rev. Lett. **106**, 053201 (2011).
6. *Collisional properties of cold spin-polarized nitrogen gas: theory, experiment, and prospects as a sympathetic coolant for trapped atoms and molecules*, T. V. Tscherbul, J. Kłos, A. Dalgarno, B. Zygelman, Z. Pavlovic, M. T. Hummon, H. Lu, E. Tsikata, and J. M. Doyle, Phys. Rev. A **82**, 042718 (2010).

7. *Magnetic Trapping of NH Molecules with 20 s Lifetimes*, E. Tsikata, W. C. Campbell, M. T. Hummon, H.-I Lu, J. M. Doyle, New Journal of Physics **12**, 065028 (2010).
8. *Mechanism of Collisional Spin Relaxation in Triplet-Sigma Molecules*, W. C. Campbell, T. V. Tscherbul, H.-I Lu, E. Tsikata, R. V. Krems, and J. M. Doyle, Phys. Rev. Lett. **102**, 013003 (2009).
9. *Magnetic trapping of atomic nitrogen (^{14}N) and cotrapping of NH ($X^3\Sigma^-$)*, M. T. Hummon, W. C. Campbell, H.-I Lu, E. Tsikata, Y. Wang, and J. M. Doyle, Phys. Rev. A **78**, 050702(R) (2008).
10. *Time-Domain Measurement of Spontaneous Vibrational Decay of Magnetically Trapped NH*, W. C. Campbell, G.C. Groenenboom, H.-I Lu, E. Tsikata, J. M. Doyle, Phys. Rev. Lett. **100**, 083003 (2008).
11. *Magnetic Trapping and Zeeman Relaxation of NH ($X^3\Sigma^-$)*, W. C. Campbell, E. Tsikata, H.-I Lu, L. D. van Buuren, and J. M. Doyle, Phys. Rev. Lett. **98**, 21300 (2007).

Acknowledgments

I would like to thank everyone who has helped and supported me through the graduate school. The completion of this thesis came from the assistance I obtained along the way.

First, I want to thank my advisor, John Doyle. He overlooked my poor spoken English when we first met and gave me a change to work in his group. Because of John's management style, the group atmosphere is extremely friendly and collaborative, which I really appreciate and enjoy. John treats graduate students' opinions with respect and gives us lots of degrees of freedom to perform research. When conducting my final thesis project, the visible and invisible roadblocks along the way almost made me switch directions. John's insights and full support guided us through the bleak period, which eventually led the project to bear fruit.

When I was a young graduate student, I was fortunate to work with Wes Campbell, Edem Tsikata, and Matt Hummon. They taught and trained me how to design an experiment properly. Standing shoulder to shoulder to these talented physicists during data taking, I learned how to carefully identify, critically analyze, and eventually solve the problems. The skills I learned from them became the assets for my thesis project.

I am blessed to work with extremely capable research partners for my thesis project, including Julia Piskorski, Boerge Hemmerling, and Ivan Kozyryev. Julia contributed to the earlier work of developing slow buffer-gas beams, which required numerous measurements to develop a model for the two-stage cell. Boerge joined our experiment as a postdoc. He not only promptly developed the DAQ system but graciously set up two dye lasers from scratch for the experiment. I also benefit from

insightful discussions with him. I would like to specially thank Ivan, who joined the project in the most difficult stage when we were short of manpower. All of the parts in the experiment he designed and built work properly, which highly speeded up the building phase. He is also talented, curious, and persistent. There were countless sleepless nights in the lab to look for trapped molecules or assemble a molecular spectrum. He was always there with me. Without his help, the experiment would not have been possible.

I also gained tremendous helps from the whole Doyle group. I can always find assistance from people in our group. By talking to Dave Patterson, Colin Connolly, and Nick Hutzler, I can find a solution to my problem, gain insights to my research, or come up with a new research direction! I am lucky to be surrounded by such a talented and friendly group of people.

Finally, I want thank my parents and my husband. They always support every decision I made in my life, including studying aboard. I can pursue my dream persistently because they are always on my side.

To my family

Chapter 1

Introduction

In this thesis, we demonstrate a new cooling and trapping method for magnetic molecules. Cold molecules are produced by laser ablation and collisional cooling with the cold, inert He buffer-gas inside a cell. We engineer the design of the buffer-gas cell, in particular its exit aperture, so that the translational energy of the emitted molecular beam is comparable to a magnetic trap with a maximum depth of 4.9 T. We produce calcium monohydride (CaH) molecules, calcium monofluoride (CaF) molecules, and potassium (K) atoms with a peak moving velocity of ~ 60 m/s and a velocity spread of 40 m/s. To load the molecules into the conservative magnetic potential, we employ two-stage optical pumping to invert the spin projection of the molecules (twice). In this fashion, not only do the molecules get decelerated on their way into the magnetic trap, but the spontaneously emitted photons also render the loading process irreversible. We demonstrate magnetic trapping of CaF in its first rotationally excited state ($N = 1$) with a trap lifetime exceeding 500 ms. Magnetic trapping of CaF ($N = 0$) and CaH is observed as well.

To motivate why we are interested developing this method, we will explain in the rest of this chapter the importance of studying cold molecules and cold molecule production methods currently available. In Ch. 2, we will present how we developed and created the slow beams and describe our systematic investigation of the beam properties. The details of the new trap loading scheme will be discussed in Ch. 3. Demonstration of magnetic trapping of molecules will be presented as well. In Ch. 4, we will describe the apparatus of the experiment, including the the buffer-gas cell, magnetic lens, and magnetic trap, etc. We also describe trajectory simulations we developed to understand the loading process and optimize the loading parameters. The algorithm of the simulation and simulation results will be shown in Ch. 5. Finally, we will discuss in Ch. 6 future experiments and physics we can explore using the method developed here.

1.1 Why cold molecules

Molecules are the building blocks of life, ranging from the air we breath to biomolecules inside our body. More than 170 gas-phase molecular species including radicals have been detected in interstellar clouds [1], which are the birthplaces of stars [2]. There are increasing interests in developing new methods in the laboratory to produce cold molecules. One reason is to study the molecular interactions systematically and provide increasingly complex, but controlled, quantum systems.

The simplest molecule consists of two atoms (a diatomic). Compared to a single atom, the additional atom inside the molecule gives rise to new degrees of freedom$-$rotational and vibrational. The typical rotational energy of molecules is $\sim$

1 K. By cooling molecules from room temperature down to ~ 20 K, only a handful of rotational states are populated and one can start accessing cold collision and cold chemistry, including those relevant to interstellar clouds, which have temperatures as low as 10 K [2]. A number of reactions involving radicals and neutral species are found to have large reaction rates at temperatures of ~ 10 K [2–4]. In addition, rotational excitation of the molecules during collisions in the interstellar cloud, followed by the radiative decay, is the dominate cooling mechanism of the gas [5] during the formation of the stars. This too can be studied.

At a temperature of ~ 1 K, the interaction energy of the magnetic (electric) dipole moment of molecules with external magnetic (electric) fields becomes comparable to the molecular translational energy, opening up the possibility of cold controlled chemistry [6, 7]. In addition, an enhanced number of molecules in the lowest rotational states, in combination with a small Doppler broadening at low temperatures, enables precision measurements. For example, the search for the electric dipole moment of electrons has been conducted in cold YbF [8] and ThO molecular beams [9]. Comparing the spectral frequencies of cold OH [10] and CH [11] molecules produced in the laboratory to those of interstellar molecular sources places constraints on the variations of fundamental constants, including the fine structure constant and the electron-to-proton mass ratio.

Further lowering the temperature to < 1 mK, the s-wave (or p-wave) collision dominates and the molecular physics enters the quantum regime. Ultra-cold chemistry has been witnessed in KRb molecules [12]. The long range and tunable electric dipolar interaction, which is absent in atomic systems, provides new handle to control the molecules [13–15]. Employing external electric field for polarizing the electric dipole moment together with microwaves for controlling the molecular rotational states gives rise to novel quantum phases [16–19].

We have pointed out here only a few interesting and exciting research topics enabled by cold molecules. Readers are referred to References [20–23] for a comprehensive review of the field.

1.2 Methods for producing cold molecules

Compared to atoms, molecules are harder to cool also because of the additional internal degree of freedoms. The widely used cooling technique for atoms, laser cooling, relies on a repetitive scattering of photon from the atoms and a number of $\sim 10^4$ momentum kicks from the photons can stop the atoms. After each scattering event, a small fraction of the atoms can decay to dark states and requires a repump laser to pump the atoms out of the dark state. Laser cooled atoms can easily reach a temperature of ~ 100 μK. From such laser pre-cooled atoms, ultra-cold molecules have been created via photo-association (PA) and Feshbach resonance [24–27]. PA optically drives two incoming free atoms to an excited molecular state, which has some probability to decay to bound, electronic ground states of molecules. The latter uses magnetic field to sweep the energy of a bound molecular state across the kinetic energy of the two atoms, and two atoms are converted to the molecular state via the hyperfine interaction with high efficiency. These two methods have created ultracold bialkali molecules successfully. However, molecules containing O, N, C, and H are out of reach due to a lack of easy laser cooling scheme for these fundamentally important atoms. In addition, the associated molecules are in highly excited vibrational states, which are collisionally unstable. Only one polar molecular species–KRb–has been brought into the ro-vibrational ground state so far, using the stimulated Raman adiabatic passage [26].

To access more chemically diverse molecules, one may want to cool the species of interest directly. Relying on adiabatic expansion cooling, supersonic beams offer rotationally cold molecules with translational temperatures of ~ 1 K in the supersonic moving frame (hundreds of m/s) [22]. Cold collision experiments at a relative collisional energy of a few degrees kelvin down to 10 millikelvin have been achieved by crossing or merging two such supersonic beams [28, 29]. However, the experimental interrogation time with the molecules is still limited by the fast moving velocity of the molecules. Several electromagnetic slowing methods have been developed to slow down the supersonic beams. Stark [30–32] (Zeeman [33, 34]) deceleration employ the interaction of the electric (magnetic) dipole moment of the molecules with pulsed electric (magnetic) fields to remove the molecular kinetic energy. More specifically, a series of electrodes (or coils for Zeeman deceleration) can be energized up in sequence and form potential hills for the molecular beam. When the molecule climbs up one of the potential hill and gets decelerated, the field is then switched off. The next electrode can be energized up when the slightly decelerated molecule enters it to remove some more kinetic energy. Since a typical interaction energy of $\vec{p} \cdot \vec{E}$ or $\vec{\mu} \cdot \vec{B}$ is ~ 1 K, it requires hundreds of slowing stages to stop a supersonic molecular beam. Optical deceleration [35] has also been employed on supersonic beams, which uses the interaction between the induced electric dipole moment of molecules with intense optical fields. Among these deceleration methods, only Stark deceleration so far has decelerated the molecular velocity a low enough value (~ 20 m/s) for trap loading and led to trapping [30–32].

Buffer-gas cooling, which exploits elastic collisions of molecules with cold inert gases, offers a general approach to generate cold molecules at a temperature of ~ 1 K [36]. This is the cooling method we adopt in this thesis. It has been applied to more than 20 molecular species, including large molecules (> 5 atoms) [37, 37]. Since only elastic collisions are involved in the cooling process, the method is generally insensitive to the internal structure of the molecules. In addition, it has been shown to cool the molecular rotational degree of freedom efficiently [38, 39]. By employing buffer-gas cooling of magnetic molecules in a buffer-gas cell locating inside a magnetic trap, magnetic trapping of molecules has been realized for CaH, NH, CrH, and MnH [40–42]. However, the constraint on the number of collisions needed during trap loading limits the in-cell buffer-gas loading method to magnetic species with a ratio of elastic to inelastic He-molecule cross sections of $\gamma_{\mathrm{col}} > 10^4$ [43].

In order to combine the advantages of collisional cooling and a low background gas density, low velocity buffer-gas beams were developed [44]. A simplest buffer-gas beam can be formed by introducing a hole (diameter of ~ 5 mm) to a buffer-gas cell, and the cold molecules leave the cell with the flowing buffer gas. Typical "single-hole" or "single-stage" buffer-gas molecular beams have a moderate moving velocity of $v_f \sim 150$ m/s, and a high molecular flux due to hydrodynamic enhancement [39,45]. Compared to supersonic beams, such a moderate moving velocity increases the interaction time with the molecules, enabling a new generation of precision measurement [9] and direct laser cooling of molecules [46–49]. Vibrational states play a major role in laser cooling of molecules. There is no strict selection rules for the vibrational states of the molecules during the optical transition. After each spontaneous emission, multiple vibrational excited states can be populated, increasing the number of dark states. However, a small subset of molecules has been identified with diagonal Franck-Condon factors, which minimize the number of repump lasers experimentally. Direct laser cooling, slowing, and 2D magneto-optical trapping of molecules have recently been demonstrated with single-stage buffer-gas beams [47–49].

1.3 Magnetic trapping with a new slow beam and a new loading method

A typical temperature of cold molecules is 10 mK $-$ 1 K using direct cooling methods. Additional cooling methods are necessary to further reduce the temperature to the quantum regime. Evaporative cooling relies on preferentially removing more energetic molecules near the trap edge and elastic collisions rethermalize the entire trapped sample. Sympathetic cooling removes the kinetic energy of the species of interest via elastic collisions with another coolant. Both cooling methods require a high density of samples and long interaction times, necessitating trapping of molecules. In addition, the shot noise limited sensitivity of the precision measurement is proportional to τ^{-1}, where τ is the interaction time with the molecules. Trapping of molecules would also greatly benefit this type of measurement. We note that evaporative cooling of trapped OH molecules from the Stark decelerated source has been realized recently [50].

A static electromagnetic field maximum cannot exist in free space in three dimensions according to Maxwell's equations. Therefore, molecules must be in low-field seeking states to be trapped in free space. The deepest traps in the laboratory are magnetic traps, which can have a depth of a few tesla for superconducting magnetic traps. This corresponds to a trap depth of $U = -\vec{\mu} \cdot \vec{B} = g_S \mu_B m_S |\vec{B}| \sim$ few Kelvin for magnetic molecules with $m_S > 0$ (low-field seeking state). Such a high trap depth allows trapping the entire distribution of buffer-gas cooled molecules at a temperature of hundreds of millikelvin. However, molecules with $m_S < 0$ (high-field seeking state) have a relative lower energy in the magnetic trap. Collisions between the molecule and the background buffer gas can change the spin projection and cause a trap loss. Therefore, the number of buffer-gas cooled magnetic species is much larger than the number of trapped species using the in-cell buffer-gas loading method. In addition, previous work has demonstrated the necessary removal of the buffer gas after trap loading, but this process remains technically challenging [51].

Loading a buffer-gas cooled beam into a magnetic trap far away from the beam source separates the cooling phase, where the buff-gas density is high, from the trapping phase, where the background density is low. There are two obstacles for direct loading of the single-stage buffer gas beam into a superconducting magnetic trap. First, molecules with a mass of $M \sim 60$ amu carry a kinetic energy of 80 K when moving at 150 m/s, which unfortunately is still well above the capture capability of the deepest available magnetic traps. Second, an irreversible loading scheme is necessary for accumulating magnetic molecules into a conservative potential.

In this thesis, we engineer a new generation of buffer-gas cell, the so called two-stage cell, to produce a slow molecule beam with a kinetic energy comparable to the trap depth of a 4.9 T deep magnetic trap. This two-stage cell design is inspired by a slow Yb source reported in Ref. [44]. When molecules enter the trap and climb up the potential hills, we employ two-stage optical pumping to flip the spin projections of molecules in the trap. The spontaneously emitted photons provide dissipation and create an irreversible loading scheme. This approach is similar to those applied to laser cooled atoms as described in Ref. [52, 53].

We would like to point out several unique features of this new method. Because only a few photon scattering events are sufficient for trap loading, this method has a significant advantage in trapping magnetic molecules with non-diagonal Franck-Condon factors, for which direct laser cooling is poorly suited. In addition, compared to the traditional in-cell buffer-gas loading scheme, the loading step employed here occurs at a low buffer-gas density of $< 10^{12}$ cm^{-3}, making magnetic trapping of low γ_{col} species feasible. This method paves the way for cooling and magnetic trapping of chemically diverse molecules, including polyatomic molecules with more vibrational degrees of freedom than diatomic molecules, which makes laser cooling infeasible. In addition, co-loading atomic species with molecules appears straightforward, providing a platform for studying cold atom-molecule collisions. This also opens up the possibility for sympathetic cooling of molecules, which has been used to cool molecular ions' translational motion using atomic ions [54] and vibrational degree of freedom using laser cooled atoms [55], but has not been demonstrated in neutral molecules.

Chapter 2

Slow CaH, K, and CaF beams from two-stage buffer-gas cell

2.1 Introduction

Since a typical strength of an electro-magnetic trap is on the order of ~ 1 K, the realization of direct trap loading of molecules relies on the production of slow molecules with kinetic energies comparable to the trap depth. A typical supersonic beam (using argon as the carrier gas) has a forward velocity of ~ 600 m/s [56], corresponding to a kinetic energy of 1300 K for molecules with a mass of $M = 59$ amu. Obviously, this beam requires a significant amount of slowing for loading into a trap to be feasible.

Several molecular species emitted from supersonic beams have been Stark-decelerated and loaded into electro-magnetic traps [30–32, 57]. However, slow radicals with high fluxes are hard to attain using this method. A slow buffer-gas cooled

PbO molecular beam was reported in 2005 [58] by adding a small exit aperture on a buffer-gas cell. Since the cooling relies on collisions with the cryogenic buffer gas, the density of the buffer gas used inside the cell is orders of magnitude lower than the supersonic beams. A PbO beam moving at 80 m/s (velocity width of 40 m/s) with a flux of 10^9 molecules per pulse was obtained. The key to obtaining a slow PbO beam is to operate in $d/l \sim 1$ (or effusive) regime, where d is the diameter of the cell aperture and l is the mean free path of the molecule colliding with the buffer gas. d/l also characterizes the number of collisions near the aperture. When a beam is operated in the effusive regime, the number of collisions near the aperture is low and the molecules mostly retain their velocity distribution in the cell. In other words, the forward velocity is given by $v_{f,eff} = v_{p,molecule} = \sqrt{2k_B T_{bg}/M}$, where M and T_{bg} are the mass of the molecule and the temperature of the buffer gas. By contrast, a supersonic beam operates at $d/l >> 1$ regime. The extraction efficiency (or a ratio of the molecular number in the beam to that in the cell) of an effusive beam, $E_{\text{ext}} = N_{\text{beam}}/N_{\text{cell}}$, is governed by the ratio of area of the aperture to the surface area of the cell, yielding $E_{\text{ext}} \sim 10^{-3}$.

A second generation of buffer-gas beam was achieved for O_2 molecules with high flux in Ref. [44], where the diffusion time (τ_{diff}) is larger than the pump out time (τ_{pump}) of the cell. This is realized by choosing the flow, size of the exit aperture, and the cell dimension appropriately. An extraction efficiency of $\sim 10\%$ was attained when $\beta = \frac{\tau_{\text{diff}}}{\tau_{\text{pump}}} > 1$ or in the hydrodynamic regime. More explicitly, β can be expressed in terms of the area of the aperture A_{aperture}, length of the cell L_{cell}, and l as $\beta = kA_{\text{aperture}}/4lL_{\text{cell}}$, where k is a dimensionless constant of order unity [44].

In the $\beta > 1$ regime, the number of collisions near the aperture is naturally larger than one, or $d/l > 1$. After multiple collisions between the molecules and the fast, forward moving buffer gas, the molecules are boosted to the moving velocity of the light buffer gas, or $v_{f,boost} = v_{p,bg} = \sqrt{2k_BT_{bg}/m_{bg}}$. Therefore, a hydrodynamically enhanced beam with high molecular flux comes at the price of a boosted molecular velocity. A typical hydrodynamic beam has a peak forward velocity of ~ 150 m/s, corresponding to a kinetic energy of 80 K for $M = 59$ amu. This requires multiple slowing stages to slow the molecules enough for trap loading.

An advanced cell design was reported in Ref. [44] in an attempt to alleviate the beam boosting. The idea is as follows. A hydrodynamic beam offers a high molecular flux but the forward velocity needs to be slowed down. One way to slow down the boosted molecules emitted from a single-stage cell is to re-scatter molecules with a rare field cold buffer gas. A 2nd cell (or slowing cell) with a lower buffer-gas density than the 1st cell was attached to the original 1st cell. The density in the 2nd cell is just high enough to thermalize (or slow down) the boosted molecules. In addition, the final exit aperture on the 2nd cell is covered up by a piece of mesh with a pore size of 140 μm to create a near-effusive beam (or $d/l << 1$). A slow Yb beam moving at 35 m/s (12 K in energy) was generated from this two-stage cell with an extraction efficiency of 1%. This two-stage cell design and results shed light on the production of a slow molecular beam with a lower moving velocity.

Motivated by the work in Ref. [44], we build a two-stage cell for producing cold CaH molecules. We start by optimizing the performance of the CaH beam in a single-stage cell to ensure that a hydrodynamic regime is reached. A 2nd cell is then attached. We investigate systematically how the properties of the CaH beam change with the density inside the 2nd cell and the geometry of the mesh. We obtain a qualitative understanding of the role the slowing cell and the mesh geometry by measuring the longitudinal velocities of the CaH beam outside the 1st and 2nd cells. Two-stage cell designs yield a slightly boosted CaH beam with $v_f = 65$ m/s (velocity width of 40 m/s), a near effusive CaH beam with a longitudinal temperature of 3.6 K, and a potassium beam.

Using an optimized two-stage cell design for slow CaH molecules, we set out to load CaF molecules into the magnetic trap, owing to a reported large ablation yield of CaF molecules. Characterizations of the CaH beams were performed in a single chamber. To perform the trap loading experiment, we expand the chamber to accommodate a superconducting trap, which is located 30 cm from the cell (See Chaper 4). In addition, a magnetic lens is installed 6 cm relative to the cell to collimate the CaF beam. The CaF beam properties are characterized 30 cm downstream. Using the identical two-stage cell which yields a slow CaH beam does not initially provide slow CaF molecules. Through adjustments to the cell geometry, we eventually obtain a slow CaF beam with $v_f \sim 55$ m/s (velocity width of ~ 45 m/s).

In contrast to a supersonic beam or a hydrodynamically enhanced buffer-gas beam, the number of He-molecule collisions inside the slowing cell and near the final exit aperture of the two-stage cell is of order unity. Considering the elastic collision between a He atom (at 4 K) moving at 128 m/s with the molecule at rest, each collision can impart a maximum velocity change of 23 m/s for CaH and 16 m/s for CaF. Given a typical forward velocity of $v_f = 60$ m/s of the two-stage beam source, the number of collisions in the beam is < 10. Therefore, obtaining a slow beam requires the fine-tuning of the experimental parameters. We would like to summarize the key elements for achieving a slow beam.

- Lowering the cell temperature. This reduces the velocities of the buffer gas and the molecules.
- Reducing the number of He-molecule collisions right near the cell exit aperture. This alleviates the beam boosting. Adding the slowing cell with roughly an order of magnitude lower He density than the 1st cell reduces the He density in the final collision region. Collisions inside the slowing cell further slow the molecules emitted out of the 1st cell.
- Adding a mesh on the 2nd cell aperture. This introduces helium flow counter to the molecular flow inside the 2nd cell, which adds to slowing. This mesh also makes the He density profile more divergent just after the mesh, which further reduces the He-molecule collisions and boosting in the beam region.
- Using ^{3}He buffer gas. When the cell is below the superfluid temperature of ^{4}He (during laser ablation), there might not be enough buffer gas for thermalization in the 1st cell and slowing inside the 2nd cell. Using ^{3}He buffer gas in this case can provide the appropriate amount of ambient He buffer gas for slowing.

The rest of the chapter is organized as follows. Section 2.2 describes the extraction efficiency of a single-stage cell for three different aperture sizes, and describes the properties of the hydrodynamic CaH beam. In Section 2.3, we characterize the properties of the slowing cell and mesh. In Section 2.4, we present the modifications for the two-stage cell to produce a slow CaF beam. We generate slow CaF molecules in three lowest rotational states for the trapping experiment.

2.2 CaH beam from single-stage cell

2.2.1 Extraction efficiency of single-stage cell at 4 K

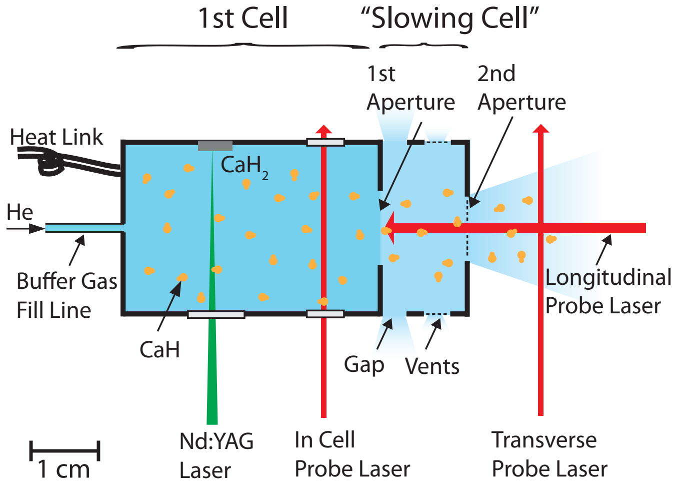

Figure 2.1: Schematic of the two-stage cell [59]. Continuously flowing ^{4}He gas through the fill line maintains a constant He density in the cell. A gap separating the two cells and the venting ports on the side reduce the He density in the slowing cell. The venting ports with dimensions 12 mm by 3 mm are covered with a 36% transparent mesh. A copper mesh covering a final exit aperture transmits CaH and He through its pores. The surface of the mesh can deflect He while absorbing CaH due to an insufficient vapor pressure of CaH radicals at low temperatures.

The schematic of the two-stage cell, which is made out of oxygen-free copper (C10100), is shown in Fig. 2.1 [59]. Inside the first cell, CaH ($^2\Sigma^+$) molecules are produced from laser ablation of a CaH_2 solid precursor with a pulsed Nd:YAG laser, which has a pulse energy of $5 - 10$ mJ and 4 ns duration. We flow ^{4}He continuously into the first cell via a fill line. After laser ablation, molecules thermalize with He and are extracted out of the first cell along with the flowing buffer gas.

The first cell is 1″ in inner diameter and 1.5″ in length with a square aperture in the front. To ensure the CaH beam emitted from the 1st cell operates in the hydrodynamic regime, we first measure the extraction efficiency of the single-stage cell using three different aperture sizes. In this study, the 2nd cell is removed and the 1st cell is cooled to 4 K by a pulsed tube cooler. CaH in its ro-vibrational ground state is detected via the $X^2\Sigma^+(v = 0, J = 1/2) \rightarrow A^2\Pi_{1/2}(v' = 0, J' = 1/2)$ transition at 14393.36 cm^{-1}. Here, we denote the quantum numbers in the electronic excited state as v' and J'. Laser absorption spectroscopy is performed in the first cell to monitor the production yield and outside the cell exit aperture to measure the beam number .

The extraction efficiencies measured for three square apertures with dimensions of 3.5 mm × 3.5 mm, 5 mm × 5 mm, and 7 mm × 7 mm are shown in Fig. 2.2, Fig. 2.3, and Fig. 2.4, respectively. We notice that the CaH beam number for the cell with 3.5 mm aperture drops below our detection sensitivity at flows > 10 sccm. At the low flow range between $0 - 10$ sccm, the extraction efficiency of the 3.5 mm aperture is roughly an order of magnitude lower than the other two aperture sizes. For larger apertures, the extraction efficiency saturates at high flows. The 7 mm aperture gives a largest CaH beam number of 2.2 $\times 10^{10}$ at 20 sccm, corresponding to an extraction efficiency of 15%. Therefore, we use this 7 mm aperture in the two-stage cell design for producing CaH beams.

The ratio of diffusion time to pump out time can be expressed in terms of buffer

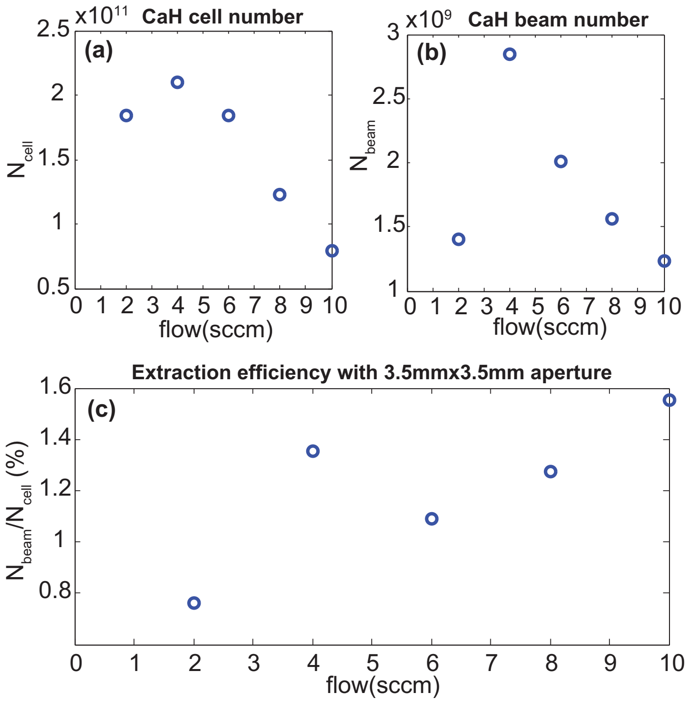

Figure 2.2: (c) Extraction efficiency of the single-stage cell with a 3.5 mm by 3.5 mm aperture as a function of flow. CaH number measured in the cell and molecular beam number measured at 3 mm outside the cell exit aperture are shown in (a) and (b), respectively. CaH beam number at a flow larger than 10 sccm is below our detection sensitivity.

gas flow f as $\beta \sim \frac{\sigma_{\rm el} f}{L_{\rm cell} v_{\rm bg}}$, where $\sigma_{\rm el}$ is the elastic cross section of the molecules colliding with the buffer gas and $v_{\rm bg}$ is the velocity of the buffer gas in the cell [56]. In this expression, there is no explicit dependence on the size of the aperture. Increasing the flow should reach the hydrodynamic regime for a given cell dimension according to this expression. However, we find the extraction efficiency of the single-stage cell does depend on the size of the aperture based on Fig. 2.2 to Fig. 2.4. This is unexplained.

We also notice a peculiar behavior of the dependence of the ablation yield on the flow or ^{4}He density in the cell (Fig. 2.2(a) to Fig. 2.4(a)). The ablation yield first increases with the ^{4}He density due to an increased amount of collisions which can stop the ablation plume. However, a decreasing ablation yield at high flows suggests that a certain reaction (or decay) process affects the production of CaH at high ^{4}He densities.

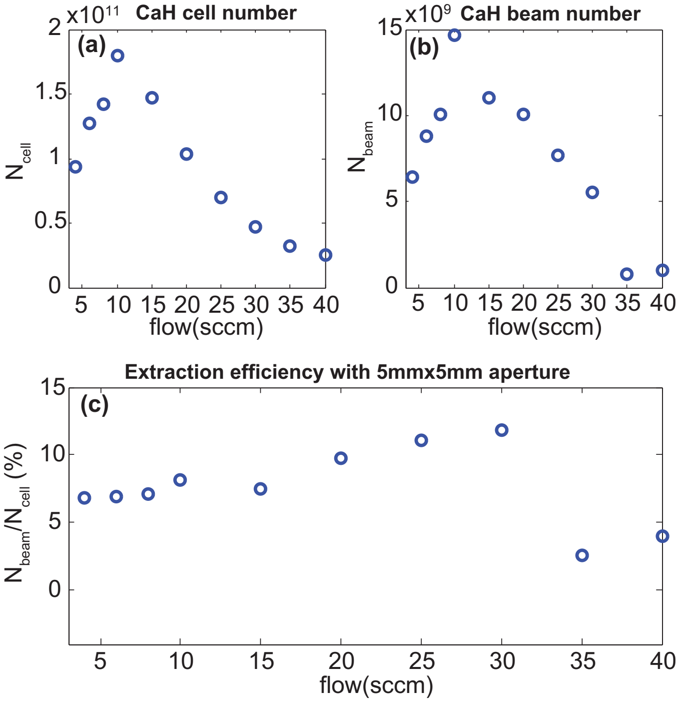

Figure 2.3: (c) Extraction efficiency of the single-stage cell with a 5 mm by 5 mm aperture vs. flow. CaH numbers in the cell and in the beam are shown in (a) and (b), respectively.

2.2.2 Velocity distributions of CaH of single-stage cell at 4 K

Using the 7 mm aperture, we measure other beam properties of the single-stage cell. The translational temperature of CaH in the cell, $T_{\mathrm{CaH,cell}}$, is obtained by fitting the absorption spectrum with a Gaussian lineshape. Although the cell is cooled by a pulsed tube cooler to a base temperature of 4 K, $T_{\mathrm{CaH,cell}}$ is fitted to be 7.4±0.3 K at

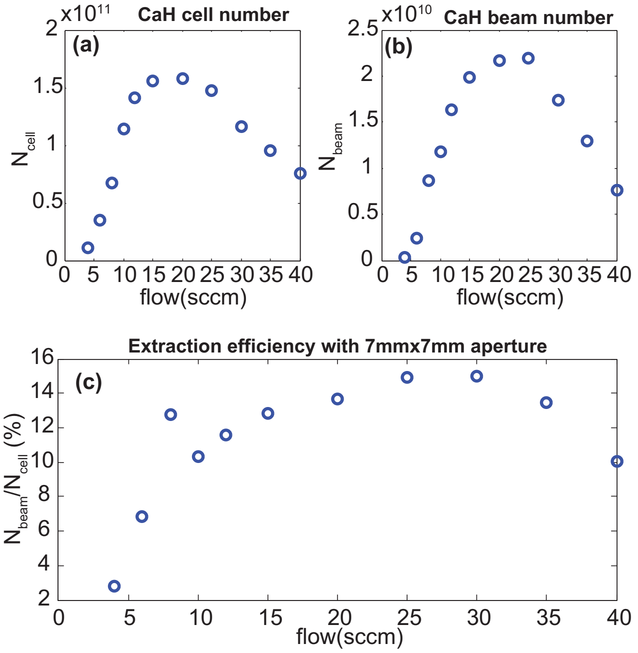

Figure 2.4: (c) Extraction efficiency of the single-stage cell with a 7 mm by 7 mm aperture vs. flow. CaH numbers in the cell and in the beam are shown in (a) and (b), respectively.

a flow of 20 sccm and using a YAG energy of 11 mJ. To extract the full width at half maximum (FWHM) of the transverse velocity distribution, δv_t, we fit the transverse beam spectrum with a Gaussian lineshape of the form $f_t(v) \propto e^{-v^2/(0.36\delta v_t^2)}$, yielding $\delta v_t = 107$ m/s.

Forward velocities of the molecular beam are determined by comparing the Doppler shifts of fluorescence spectra induced by a longitudinal probe laser (Fig. 2.1) relative to the absorption spectrum obtained in the cell. The fluorescence induced by the longitudinal probe laser is collected by a CCD camera. We fit the fluorescence spectra with a Gaussian lineshape of the form $f_l(v) \propto e^{-(v-v_{\mathrm{f},1})^2/(0.36\delta v_l^2)}$, where δv_l is the FWHM of the longitudinal velocity distribution. At the same experimental conditions, the forward velocity of CaH is measured to be $v_{\mathrm{f},1} \sim 160$ m/s with $\delta v_l = 74$ m/s.

2.2.3 Velocity distributions of CaH of single-stage cell at 1.8K

Cooling the cell to a lower temperature reduces the temperature and the velocity of the buffer gas. Before moving on to the two-stage cell design, we connect the single-stage cell to a helium pumped reservoir (so called "1K pot") for cooling the cell to a base temperature of 1.8 K. At a flow of 3 sccm and YAG energy of 5 mJ, we obtain $T_{\mathrm{CaH,cell}} = 4.1 \pm 0.2$ K, $v_{\mathrm{f},1} = 127$ m/s, and $\delta v_t = 88$ m/s. The most probable velocity of CaH at a temperature of 4.1 K should be $v_{\mathrm{p,CaH}} = 41$ m/s; by contrast, ^{4}He atoms have a moving velocity of $v_{\mathrm{p,He}} = 130$ m/s at the same temperature. Given the measurement, the CaH molecules certainly undergo multiple collisions with ^{4}He in the beam so that $v_{\mathrm{f},1}$ is equal to the moving velocity of ^{4}He, i.e. it is "fully boosted".

2.3 Engineering a two-stage cell to produce slow CaH and K beams

Cooling the single-stage cell down to 1.8 K reduces $v_{f,1}$ down to 127 m/s. However, this still corresponds to a kinetic energy of 40 K for CaH. Our superconducting magnetic trap has a maximum depth of 4.9 T, yielding a depth of 3.3 K for one Bohr magneton molecule. Implementing a two-stage cell to further reduce the moving velocity of molecules is necessary.

2.3.1 CaH beams with a two-stage cell at 4 K

The slowing cell has internal dimensions of 1″ diameter and $\frac{3}{8}''$ length with an exit aperture of 9 mm diameter. There are two venting ports on the side of the slowing cell (Fig. 2.1) to leak out some buffer gas. These venting ports have dimensions 12 mm by 3 mm and are covered with a 36% transparent mesh. The length of the gap between the two cells can be adjusted so as to lower ("tune") the density in the 2nd cell (or slowing cell). The exit aperture of the 2nd cell is covered with a piece of copper mesh in an attempt to create a near effusive environment such that molecules inside the slowing cell can experience collisions against the flow direction with He bouncing from the mesh.

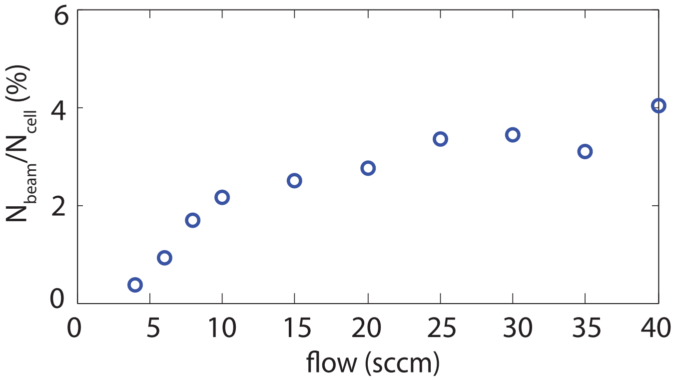

Figure 2.5: Extraction efficiency of the two-stage cell (4 K) with a gap of 0.9 mm and a 36% transparent mesh on the 2nd aperture.

As a first attempt to understand the two-stage cell, we operate the cell at 4 K (before cooling to our final running temperature of 1.8 K). The gap distance of 0.9 mm and the (2nd aperture) mesh with pore size of 0.8 mm and 36% transparency are used. E_{ext} is measured as a function of flow as shown in Fig. 2.5. An extraction efficiency lower than that of a single-stage cell is expected, owing to the mesh blocking part of the molecular flow. At a buffer-gas flow of 15 sccm, YAG energy of 11 mJ, and a cell base temperature of 4 K, we obtain $T_{\text{CaH,cell}} = 10.9 \pm 0.7$ K, $\delta v_t = 90$ m/s, $\delta v_l = 50$ m/s, and $v_{\text{f},2} = 113$ m/s. $v_{\text{f,CaH}}$ drops from 160 m/s with a single-stage cell to 113 m/s with a two-stage cell. A natural step to further slow the beam is to cool the two-stage cell down to 1.8 K.

2.3.2 Effect of the density in the 2nd Cell (1.8K)

When the two-stage cell with a gap distance of 0.9 mm and 36% transparent mesh is cooled to 1.8 K, we measure the beam velocities, as shown in red circles and squares in Fig. 2.6(a). The moving velocities of CaH outside the 1st cell and 2nd cell can be measured since the longitudinal detection laser illuminates the 1st cell (Fig. 2.6(b)) and the CCD camera can spatially distinguishes the location of the fluorescence signal. $T_{\text{CaH,cell}} = 4.4 \pm 0.2$ K is measured at a YAG energy of 5 mJ, yielding a thermal velocity of CaH in the cell of 42 m/s. The measured $v_{\text{f},1} \sim 50$ m/s is close to the thermal velocity of CaH molecules in the cell, yet $v_{\text{f},2} > 80$ m/s indicates there is still multiple collisions near the 2nd aperture. The overall open area of the 2nd cell, $A_{\text{2nd cell}}$, which includes the area of the gap, venting ports, and 2nd aperture covered with mesh, is a factor of $3.5 = \frac{A_{\text{2nd cell}}}{A_{\text{1st aperture}}}$ larger than the size of the 1st aperture. To reduce the ^{4}He density in the slowing cell further as well as the amount of collisions near the 2nd aperture, we increase the gap distance to 2.8 mm, yielding $\frac{A_{\text{2nd cell}}}{A_{\text{1st aperture}}} = 9.4$.

Data depicted in blue circles and squares in Fig. 2.6(b) are the forward velocities of CaH from the two-stage cell with a 2.8 mm gap. Although $v_{\text{f},1} \sim 55$ is slightly

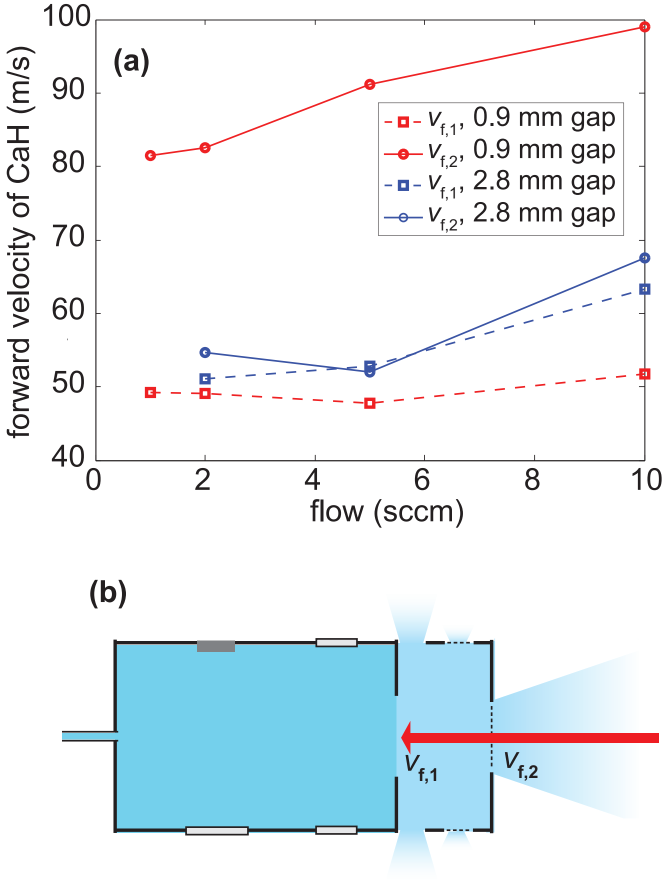

Figure 2.6: (a) Forward velocity of CaH measured outside the first cell, $v_{\mathrm{f},1}$, and 2nd cell, $v_{\mathrm{f},2}$, as a function of flow for two gap distances. Data plotted in blue (red) is taken for a gap distance of 2.8 mm (0.9 mm). Here, the mesh on the 2nd aperture has a pore size of 0.8 mm with a transparency of 36%. YAG energy is 5 mJ. (b) Schematic of the cell indicates where the forward velocity is measured. $v_{\mathrm{f},2}$ is measured at 3 mm from the 2nd aperture.

larger than the case of a 0.9 mm gap, the final beam velocity $v_{\mathrm{f},2} \sim 60$ m/s shows an insignificant amount of boosting. We attribute this to a reduced amount of collisions in the beam which mitigates the beam boosting. We would like to know the ^{4}He density in the 2nd cell with a 2.8 mm gap. To answer this question, the dynamics of CaH molecules in the 1st cell needs to be analyzed in order to estimate the ^{4}He density in the first cell.

2.3.3 ^{4}He density in the 1st cell

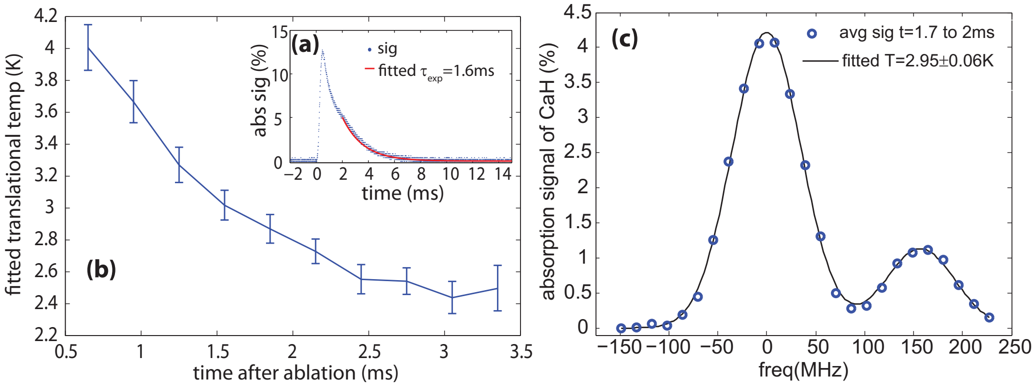

Figure 2.7: Thermalization dynamics of CaH in the first cell. (a) On-resonance absorption signal of CaH. A single exponential fit is used to extract the decay time of CaH when molecules thermalize to the buffer gas. (b) Fitted CaH translational temperature as a function of time after ablation. (c) Absorption spectrum between $1.7 - 2$ ms after ablation. The fitted doppler temperatures over different time windows are plotted in (b).

Fig. 2.7(a) plots the absorption signal of CaH after laser ablation [59]. The number of CaH molecules in the first cell decays in time due to the diffusion to the cell wall and extraction into the second cell. The measured decay time τ_{exp} is related to the diffusion time τ_{diff} and the emptying time of the first cell τ_{pump} by a simple relation $\tau_{\mathrm{exp}}^{-1} = \tau_{\mathrm{diff}}^{-1} + \tau_{\mathrm{pump}}^{-1}$, where τ_{pump} can be calculated based on the geometry of the first cell. τ_{diff} is determined to be 2 ms at 2 sccm flow, corresponding to a ^{4}He density of 3×10^{15} cm^{-3}, if the estimated diffusion cross section of 10^{-14} cm^2 between CaH and He is used.

The overall open area of a 2nd cell with a gap of 2.8 mm is a factor of 9.4 larger than the area of the 1st aperture, giving a ^{4}He density in the 2nd cell of $n_2 \sim 3 \times 10^{14}$

cm^{-3} at 2 sccm flow.

2.3.4 Role of the slowing cell

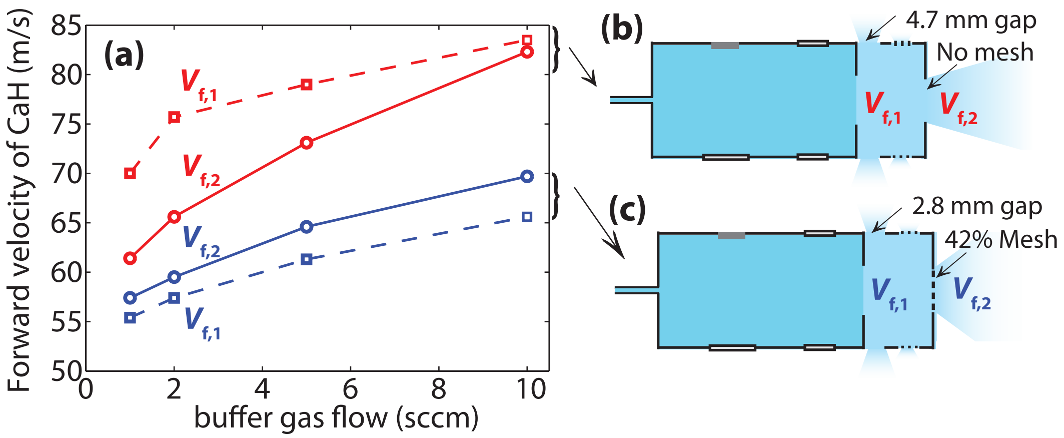

Figure 2.8: (a) Forward velocities v_f plotted in red are for a relatively open cell shown schematically in (b) with a 4.7 mm gap and no mesh on the second aperture; (c) shows a different cell configuration with a 2.8 mm gap and with a 42% transparent mesh covering the second aperture. Its corresponding forward velocities are plotted in blue in (a).

To investigate the role of the slowing cell, we measure the forward velocity of a two-stage cell without a mesh covering the 2nd aperture, depicted in red squares and circles in Fig. 2.8(a). With a gap distance of 4.7 mm, $\frac{A_{\text{2nd cell}}}{A_{\text{1st aperture}}} = 16$. $v_{\text{f},2}$ is measured to be lower than $v_{\text{f},1}$, indicating that CaH passing through the 2nd cell encounters a couple of collisions with cold ^{4}He atoms. This leads to the actual *slowing* of the molecules emitted from the 1st cell. $v_{\text{f},1} \sim 75$m/s of this cell configuration is higher than that of the less open 2nd cell (See blue circles in Fig. 2.6(a) for a cell with 2.8 mm gap and 36% transparent mesh). We can understand this observation as follows. If the density of the 2nd cell, n_2, is equal to that of the 1st cell, CaH retains its thermal velocity due to constant collisions with ^{4}He or $v_{\mathrm{f},1} \sim v_{p,CaH}$. At the other extreme, if n_2 approaches zero, CaH beam emitted out of the 1st cell forms a hydrodynamic beam and is fully boosted or $v_{\mathrm{f},1} \sim v_{f,boost}$. Therefore, a larger density gradient across the two cells causes an increased $v_{\mathrm{f},1}$.

We attempt to extract more CaH molecules from the two-stage cell by using a more transparent mesh. Data plotted in blue squares and circles in Fig. 2.8 (a) shows the forward velocity from a cell with a 2.8 mm gap and a mesh of 42% transparency on the 2nd aperture. This mesh has a pore size of 0.75 mm, leading to $\frac{A_{\mathrm{2nd\ cell}}}{A_{\mathrm{1st\ aperture}}} = 10$. The attained $v_{\mathrm{f},2}$ is comparable to the cell using a 36% transparent mesh (See data depicted in blue circles in Fig. 2.6(a)). $E_{\mathrm{ext}} > 1\%$ measured for this cell configuration is shown in Fig. 2.9.

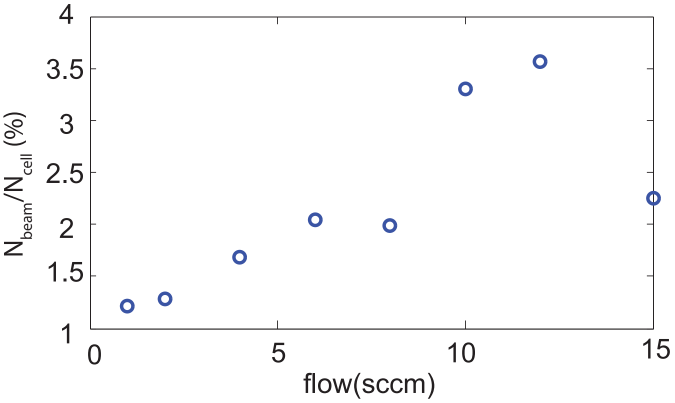

Figure 2.9: Extraction efficiency of the two-stage cell (1.8 K) with a gap of 2.8 mm and a 42% transparent mesh on the 2nd aperture.

2.3.5 Effects of mesh

We study the effect of the mesh by measuring the forward velocity using a fine mesh of a 32% transparency with a pore size of 0.16 mm, as shown in black squares

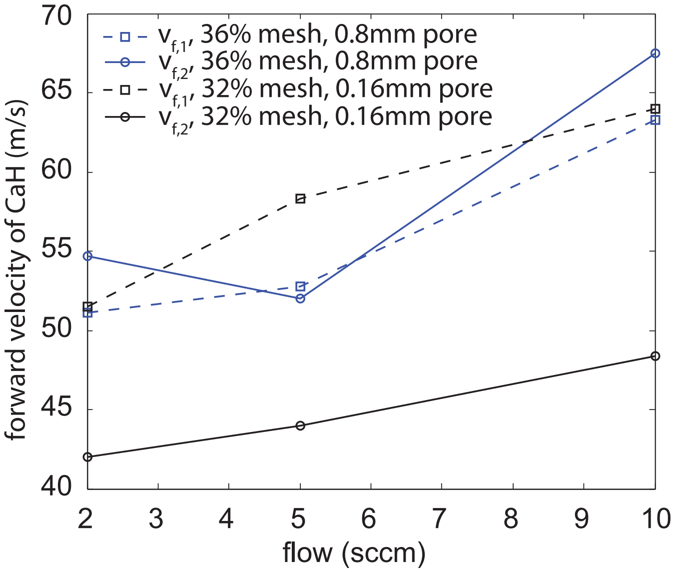

Figure 2.10: Forward velocities v_f measured for the two-stage cell with a coarse mesh (36% transparency, 0.8 mm pore size) and a fine mesh (32% transparency, 0.16 mm pore size) are shown in blue and black, respectively.

and circles in Fig. 2.10. As a comparison, we plot the forward velocity of the two-stage cell with the 36% transparent mesh (pore size of 0.8 mm) in blue. Forward velocities measured outside the first cell $v_{\mathrm{f},1}$ for both mesh geometries are comparable. However, $v_{\mathrm{f},2}$ from the cell with a fine mesh is $\sim$ 15 m/s slower than that of the coarse mesh (0.8 mm pore size). We attribute this effect to the additional ^{4}He-CaH collisions inside the slowing cell since extra ^{4}He atoms can be deflected from the fine mesh back to the 2nd cell.

Fig. 2.11 compares the $v_{\mathrm{f},2}$ as a function of distance from the 2nd aperture for two cell geometries: one cell has a 2.8 mm gap with a 42% transparent mesh and the other has a 3.8 mm gap without mesh on the 2nd aperture. The cell without mesh, which has $\frac{A_{\text{2nd cell}}}{A_{\text{1st aperture}}} = 13$, should have a lower n_2 than the cell with mesh, yet it experiences more boosting. This suggests that the presence of mesh may introduce

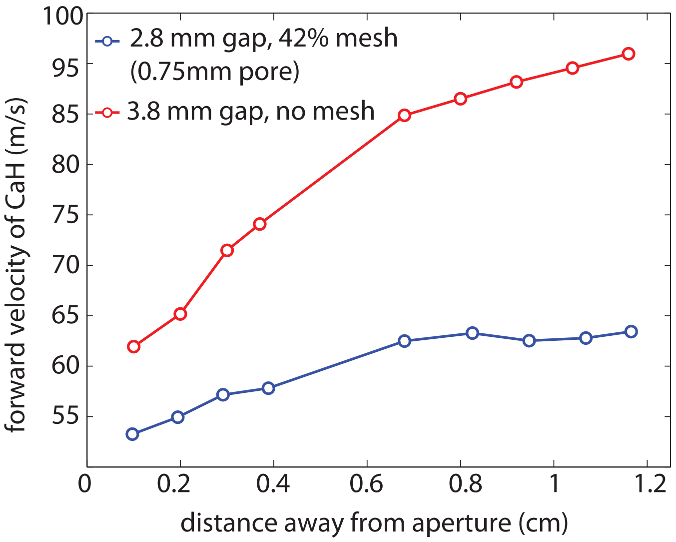

Figure 2.11: Forward velocities $v_{\mathrm{f},2}$ versus distance away from the 2nd aperture for the two-stage cell with the 2.8 mm gap and coarse mesh (42% transparency, 0.75 mm pore size) are illustrated in blue; by contrast, $v_{\mathrm{f},2}$ for a two-stage cell with a 3.8 mm gap and no mesh is depicted in red.

a large ^{4}He density drop across the aperture and cause the ^{4}He beam profile to be more divergent. Both factors can lead to fewer ^{4}He-CaH collisions in the beam, and hence less boosting.

2.3.6 Forward velocity distributions

We compare the longitudinal velocity distributions measured at 3 mm from the 2nd aperture of the two-stage cell using coarse and fine meshes in Fig. 2.12. The coarse (fine) mesh has a transparency of 42% (32%) and a pore size of 0.8 mm (0.16 mm). The velocity distribution using the coarse mesh is fitted with a Gaussian distribution, yielding $v_{\mathrm{f},2} = 62$ m/s and $\delta v_l = 43$ m/s. By contrast, an effusive distribution of the function form $f_{\mathrm{eff}}(v) \propto (v/v_{\mathrm{p}})^2 e^{-(v/v_{\mathrm{p}})^2}$ fits well the distribution for the cell with fine mesh, yielding $T = 3.6 \pm 0.6$ K.

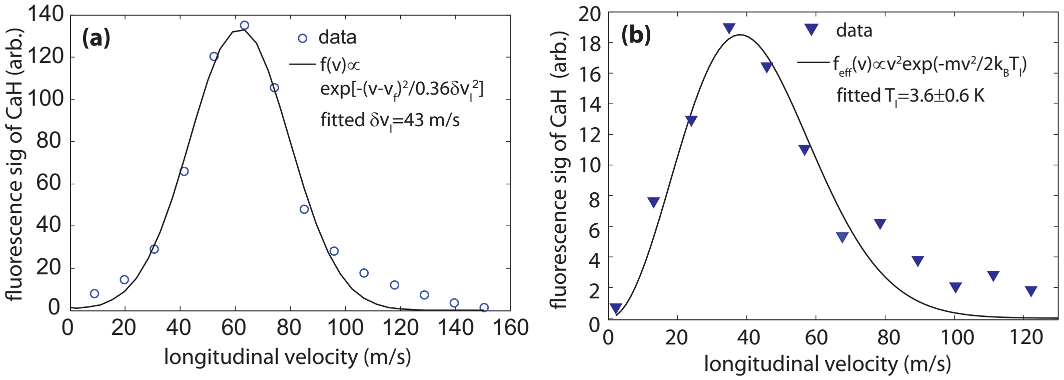

Figure 2.12: Longitudinal velocity distributions for the two-stage cell (2.8 mm gap) with a coarse mesh of 42% transparency (0.75 mm pore) and a fine mesh of 32% transparency (0.16 mm pore) are plotted in (a) and (b), respectively. The velocity is measured at 3 mm from the 2nd aperture.

Although the peak forward velocity of cell with the fine mesh is 20 m/s lower than the cell with the coarse mesh, the extraction efficiency using the fine mesh is roughly a factor of two lower than the coarse mesh. This is also likely due to the additional He-molecule collisions in the 2nd cell from the fine mesh. The additional slowing comes at the expense of the beam intensity.

2.3.7 Boosting of CaH beam and K beam

The slow CaH beam from the two-stage cell has $v_{\mathrm{f},2} = 62$ m/s using the coarse mesh and $v_{\mathrm{f},2} = 40$ m/s using the fine mesh measured at 3 mm from the aperture. The translational temperature of CaH in the 1st cell after ablation drops from 4 K to 2.5 K (See Fig. 2.7), corresponding to a thermal velocity of $40 \rightarrow 32$ m/s. By contrast, the thermal velocity of ^{4}He changes from $129 \rightarrow 101$ m/s for this temperature change. This suggests the beam using the coarse mesh is still slightly boosted owing to collisions with ^{4}He in the beam. A data set shown in Fig. 2.13 supports

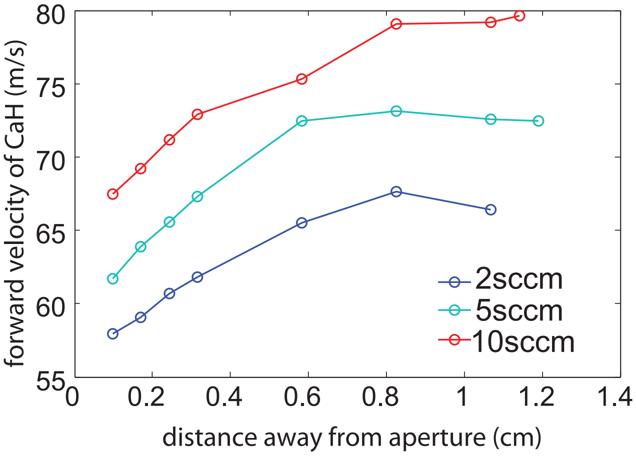

Figure 2.13: $v_{\mathrm{f},2}$ versus distance from the 2nd aperture measured for three flows. The cell has a 2.8 mm gap and a 42% transparent mesh (0.8 mm pore).

this point, where $v_{\mathrm{f},2}$ using the coarse mesh increases with both distances relative to the aperture and flows. The ^{4}He-CaH collisions freeze out at 1 cm ($\sim$ diameter of the 2nd aperture), yielding a final beam velocity of $v_{\mathrm{f},2} \sim 65$ m/s for the cell with a coarse mesh operating at 2 sccm.

We attempt to measure the final velocity of CaH beams for the cell with fine mesh. However, a lower extraction efficiency causes the CaH beam signal to drop below our detection sensitivity rapidly with distance. As potassium atoms have a similar mass to CaH molecules and a large photon scattering rate, we use K atoms to characterize the final velocity of the two-stage cell with the fine mesh.

Measured longitudinal velocity distributions of K from the cell with the 32% transparent fine mesh are illustrated in Fig. 2.14. Here, the velocity distributions up to 3.6 cm from the 2nd aperture are obtained. The K beam has a similar forward velocity of $v_{\mathrm{f},2} \sim 40$ m/s to the CaH beam at 4 mm. At 1.2 cm, $v_{\mathrm{f},2}$ approaches 50 m/s and the collisions freeze. We measure a number of 3.4×10^{10} K atoms/pulse in

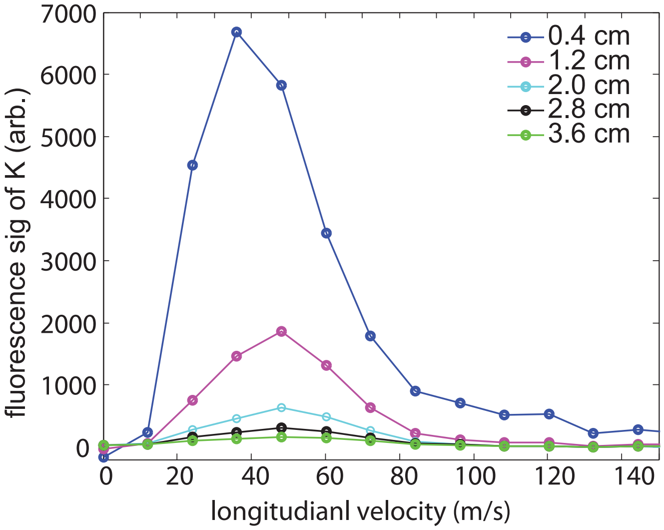

Figure 2.14: Longitudinal velocity distributions of K atoms measured for several distances from the 2nd apertures. The diameter of the detection laser is smaller than the size of the K beam and the fluorescence signal is mostly from the atoms close to the centerline. A finite transverse divergence of the K beam causes the signal to decrease with distance from the aperture. The two-stage cell has a 2.8 mm gap and a fine mesh with 32% transparency. The ablation target used in the first cell used KCl.

the beam using the 32% transparent fine mesh and 5.3×10^{10} atoms/pulse for the 42% coarse mesh.

2.4 Slow CaF beams

CaF is produced by laser ablation of a solid precursor CaF_2. Several types of targets are used. Two home-made targets are produced by pressing CaF_2 powers (99.95% metals basis) into a 0.58″ diameter pellet with a pressure of 40 MPa and a 0.25″ diameter pellet with a pressure of 6 MPa. We also purchased hot vacuum pressed targets (99.9% purity) from Sophisticated Alloys and sputtering target (99.9% purity) from American Elements. We found that there is a significant amount of dust

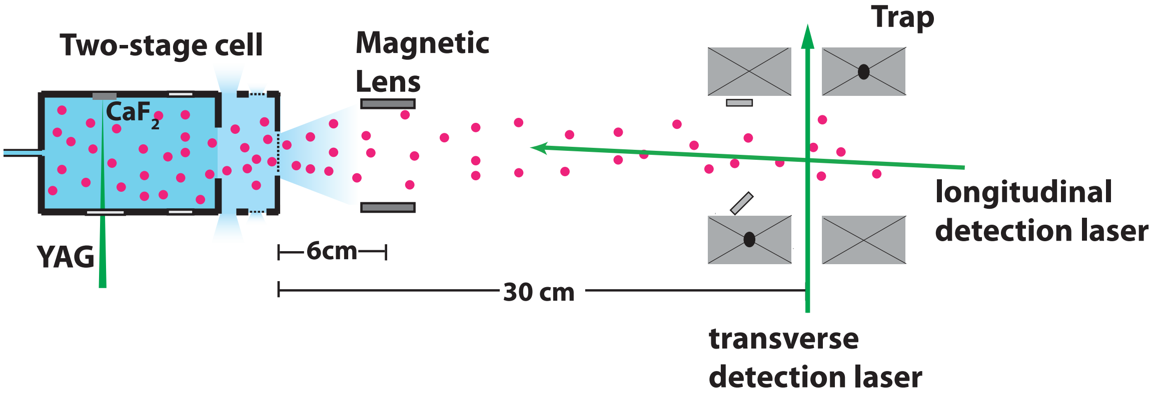

Figure 2.15: Schematic of the apparatus, which includes a two-stage cell for producing cold CaF molecules, magnetic lens, and a magnetic trap (0 A). The longitudinal and transverse detection beams interrogate the molecules inside the trap. The fluorescence signal is collected by two fiber bundles mounted on the magnet cask along the trap midplane (not shown here). The longitudinal velocity distribution is extracted based on the spectral shift relative to the transverse beam spectrum.

ejected out of these targets during ablation. A visible layer of dust coated the entire cell interior after a few days of data taking.

Once the cell interior is coated with a layer of insulator, we hypothesize that the buffer gas can no longer thermalize with the copper cell. This causes the beam to speed up over time, which is consistent with our observations as described below. We note that the dust problem is less severe using the sputtering target, which gives us the slowest CaF beam and is used in our trap loading experiment.

2.4.1 CaF beam using ^{4}He buffer gas

Before starting the trap loading experiment, we move the two-stage cell with a 2.8 mm gap and 42% transparent coarse mesh into the new dewar and measure beam forward velocities at the trap midplane. The schematic of the apparatus for

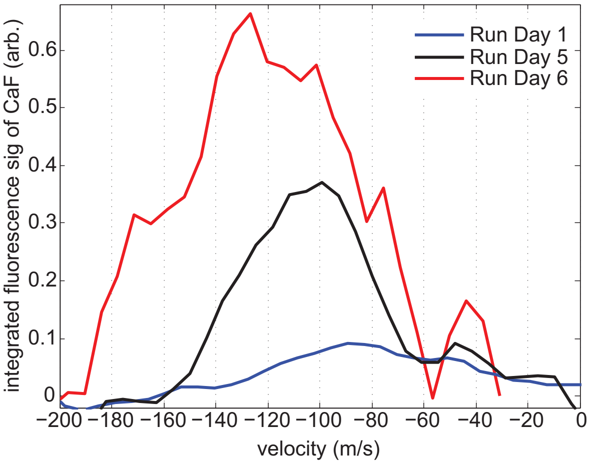

Figure 2.16: Longitudinal velocity distributions of CaF ($N = 0$) using ^{4}He measured at 30 cm relative to the 2nd cell aperture. Experimental conditions: 6 mJ YAG energy at 10 Hz repetition rate, 3 sccm buffer-gas flow. The peak moving velocity of CaF increases with the time of data taking. Run Day 1 indicates the first day of operating the CaF beam.

characterizing the CaF beam is illustrated in Fig. 2.15. The cell inside the new dewar has a lower base temperature of 1.4 K due to an improved thermal links to the 1K pot. ^{4}He is used as the buffer gas for initial data taking and we change to ^{3}He for further data taking.

Fig. 2.16 illustrated the CaF longitudinal velocity distributions using ^{4}He. CaF ($N = 0$) is detected via $X^2\Sigma^+(v = 0, N = 0) \rightarrow B^2\Sigma^+(v' = 0, N' = 1)$ at 564.622680 THz ($R_1(1/2)$ line). See Fig. 2.17 for the level diagram of CaF relevant to this experiment. The fluorescence signal induced by the longitudinal detection laser is collected by two fiber bundles mounted on the magnet cask at the trap midplane. The photons are recorded by a photomultiplier tube operating in analogue mode, for the data set shown here. Although the cell is the same as that used to generate the CaH beam with $v_{\mathrm{f,CaH}} = 65$ m/s, the CaF beam with $v_{\mathrm{f,CaF}} \sim 90$ m/s on the first day of data taking (or Run Day 1) is faster. (We drop the subscript *2* from now on since we are comparing the beam properties outside the zone of freezing.) In addition, the beam velocity increases with time after we start running. As mentioned above, we also noticed the dusty layer accumulated on the interior of the cell grew thicker over the same period of time (about a day).

Despite using the identical two-stage cell design in conjunction with operating at a lower cell temperature, CaF beam measured on the 1st day of the cooldown moves faster than the CaH beam by 25 m/s. To investigate why this is the case, we first compare the thermalization dynamics of CaF with CaH in the 1st cell, as shown in Fig. 2.18(a). Even though the cell operates at a lower base temperature of 1.4 K for CaF than at 1.8 K for CaH, the translational temperature of CaF settles to a steady state temperature of 5 K, which is 2.5 K higher than CaH. Assuming He atoms are at the same temperature with CaF molecules, the corresponding most probable velocity at 5 K is $v_{\mathrm{p,He}}=$ 144 m/s, which could lead to a fast molecular velocity due to the He-CaF collisions in the beam. The size of CaF_2 target used in this data set has a diameter of $0.5''$ while the CaH_2 target is $0.28''$ in diameter. We suspect the surface temperature of these targets is higher than the copper cell wall after ablation due to a poor thermal conductivity of targets, causing a local hot spot in part of the cell.

At a first glance, making the cell cooler should have improved the performance of the beam. The ablation pulse typically heats up the cell by roughly 1 K depending on the exact pulse energy and repetition rate of the YAG laser. Since the cell base temperature for CaF is at 1.4 K, the temperature of the 2nd cell during ablation for CaF could remain below the superfluid temperature of ^{4}He of 2.3 K. In addition, the

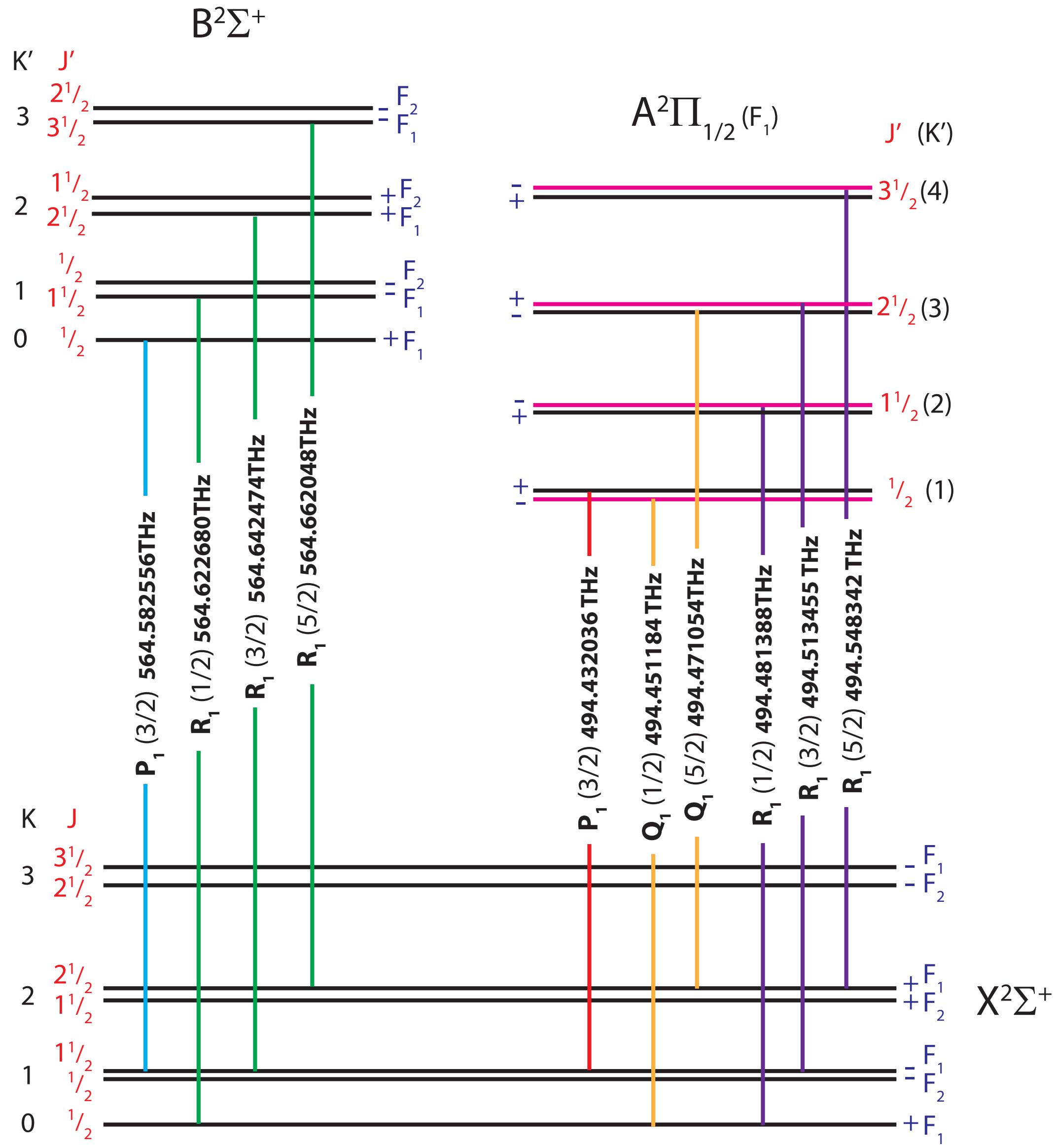

Figure 2.17: CaF level diagram relevant to this work. Note that the frequency is measured by WS/7 wavemeter from HighFinesse, which has an absolute accuracy of 60 MHz. $X-A$ transition is used for optical pumping and $X-B$ transition is for detection. The references which guide us to locate these lines are: [60], [61], [62].

vapor pressure of ^{4}He drops by two order of magnitudes between 2 K and 1 K [63]. We suspect that there might not be enough ^{4}He density in the 2nd cell for slowing down

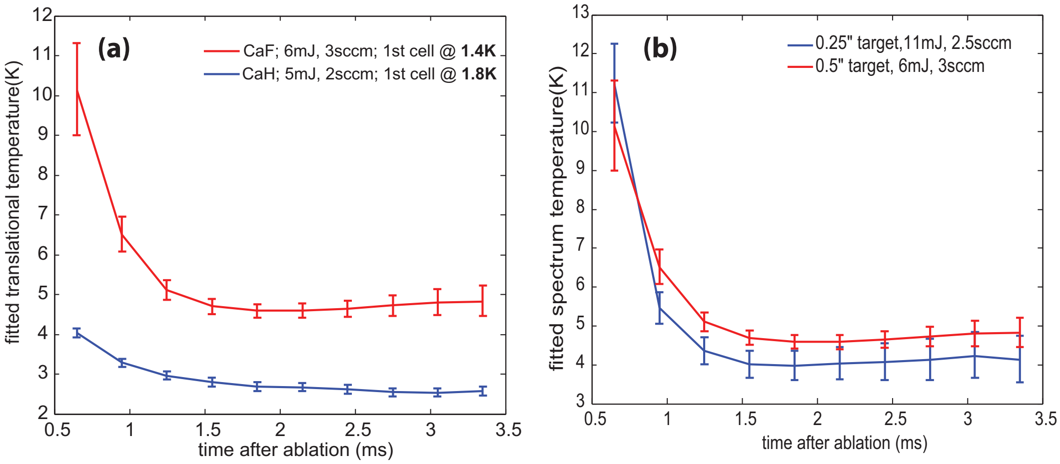

Figure 2.18: (a) Translational temperatures of CaF (red trace) and CaH (blue trace) in the 1st cell after ablation. Two-stage cell has a 7 mm × 7 mm 1st aperture, 2.8 mm gap, and 42% transparent mesh on the 2nd aperture. In addition, the two-stage operates at a base temperature of 1.4 K and 1.8 K for CaF and CaH, respectively. (b) Translational temperature of CaF in the 1st cell with a 7 mm × 7 mm 1st aperture and a target diameter of 0.5″ is shown in red trace. Translational temperature of CaF using a 5 mm diameter 1st aperture and a target diameter of 0.25″ is plotted in blue trace.

CaF molecules. To test this possibility, we heat the cell to a base temperature of 1.8 K. The measured longitudinal velocity distributions for CaF are shown in Fig. 2.19. A slower CaF beam with v_f = 90 m/s is generated at a base temperature of 1.8 K, which is 20 m/s slower than the CaF beam using the cell at 1.4 K (base temperature).

2.4.2 Slow CaF beam-smaller target size and 1st aperture size

In order to improve the thermalization after ablation, we replace the 0.5″ diameter CaF_2 target from Sophisticated Alloy with a pressed target of 0.25″ in diameter. In addition, we change the 1st aperture from a 7 mm square aperture to a 5 mm diameter round aperture so that the ^{4}He density in the first cell is increased at the same flow. The blue trace in Fig. 2.18(b) illustrates the thermalization dynamics of

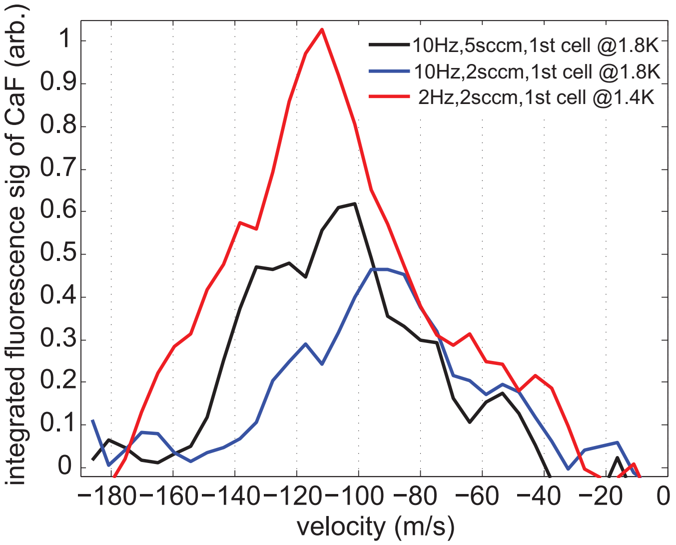

Figure 2.19: Longitudinal velocity distributions of CaF ($N = 0$) using ^{4}He measured at 30 cm downstream. Data shown in black and blue are taken at a flow of 5 sccm and 2 sccm with a cell base temperature of 1.8 K and YAG energy of 4 mJ at 10 Hz. As a comparison, data depicted in red is for the CaF beam at a lower cell base temperature of 1.4 K. These three data sets are taken on the same day of a cooldown (Run Day 6 of 22Oct2012 Cooldown).

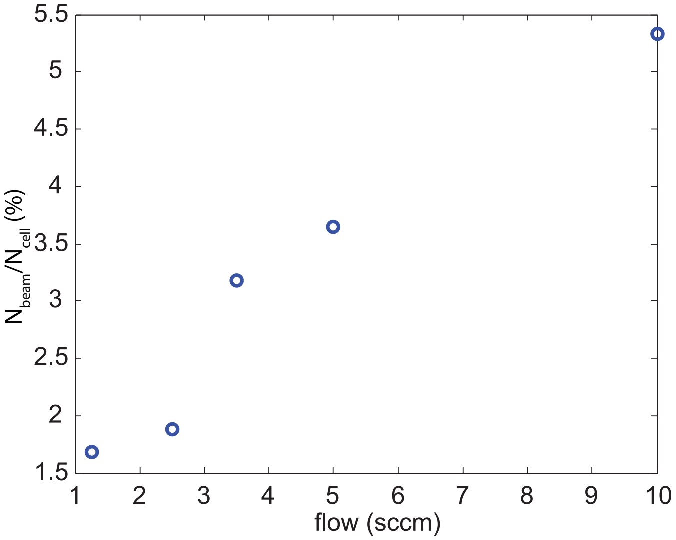

Figure 2.20: Extraction efficiency of CaF using a two-stage cell with a 5 mm diameter 1st aperture, 2.8 mm gap, and 42% transparent mesh. YAG energy is 6 mJ at 2 Hz.

the 0.25″ target, which reaches a lower steady state temperature than the 0.5″ target despite of using a larger YAG energy. On the first day of cooldown, we measure a forward velocity of $v_f = 65$ m/s (velocity width of ~ 40 m/s) using ^{4}He at 1.25 sccm flow and a YAG energy of 10 mJ at 5Hz. There is a reduction of beam velocity of 25 m/s compared to the previous configuration. However, the forward velocity is again observed to progressively increase with time.

With this new cell configuration, we produce $N_{cell,CaF} = 1.2 \times 10^{11}$ molecules/pulse in the 1st cell using ^{4}He buffer gas and a YAG energy of 6 mJ (2 Hz). The transverse beam spread measured outside the cell is $\delta v_t = 56$ m/s and the extraction efficiency versus flow is shown in Fig. 2.20. At a flow of 1.25 sccm, an extraction efficiency of 1.6% corresponds to a CaF number of $N_{upstream,CaF} = 2 \times 10^9$ molecules/pulse outside the cell.

2.4.3 Slow CaF beam-^{3}He buffer-gas

On Run Day 5 of the 19Dec2012 cooldown, we switched to use ^{3}He as the buffer gas, which has a factor of $10 - 100$ higher vapor pressure than ^{4}He between 2 K and 1 K. Fig. 2.21 shows the longitudinal velocity distributions of CaF beam using ^{3}He as the buffer gas, which are slower than the CaF beam using ^{4}He buffer gas taken on the previous day of the same cooldown. We obtain $v_f \sim 65$ m/s using a YAG energy of 4 mJ at 2 Hz and 1.25 sccm ^{3}He flow. We also notice that not only the ablation yield but the beam intensity measured at 30 cm using ^{3}He buffer gas is larger than ^{4}He (Fig. 2.21). A CaF number of $N_{cell,CaF} = 3.75 \times 10^{11}$ using a YAG energy of 4 mJ (2 Hz) is a factor of 3 larger than the case using ^{4}He. We can not explain the

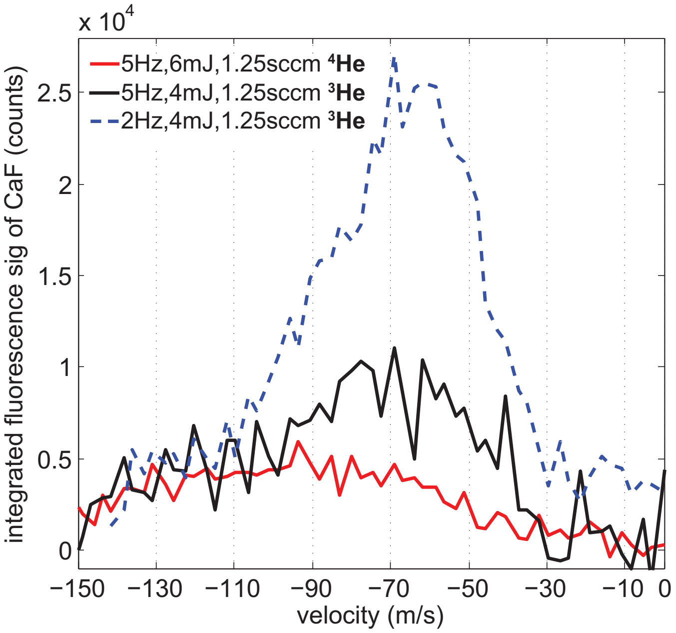

Figure 2.21: Black and blue traces are longitudinal velocity distributions of CaF ($N = 0$) at two YAG repetition rates taken on Run Day 5 of the 19Dec2012 cooldown using ^{3}He as the buffer gas. As a comparison, data plotted in red trace is taken on Run Day 4 for the CaF beam using ^{4}He buffer gas. PMT is operated in photon-counting mode here.

specific reason why the beam property using ^{3}He as the buffer gas is better than that with ^{4}He. However, we suspect that using ^{3}He provides a sufficient buffer-gas density inside the 1st and 2nd cell for thermalization and slowing. We also suspect that our observation may be related to the superfluidity of ^{4}He. The cell temperature is below (roughly equal to) the critical temperature of ^{4}He without (with) ablation while ^{3}He behaves as a normal gas.

To estimate the CaF beam number reaching 30 cm downstream, we perform trajectory simulation to estimate the size of the molecular beam. The average beam diameter in the simulation is $L_{beam} = 4$ cm. The molecular beam has the highest density along the center line and roughly half of the molecules distribute within a radius of $L_{beam}/2$. In addition, we measure the transverse beam spectral function, as shown in Fig. 2.22(a). The narrow transverse beam linewidth of 31 MHz is due to the focusing of the magnetic lens. The recorded PMT signal, Sig, is related to the photon scattering rate R_{scat} out of the molecular beam as

$$Sig = R_{\text{scat}} \times C.E. \times Q.E., \tag{2.1}$$

where $C.E.$ and $Q.E. = 0.18$ represent the light collection efficiency and quantum efficiency of the PMT. We collect the fluorescence using two fiber bundles (borosilicate, each has a 0.375″ active diameter) mounted on the trap midplane and at 41 mm from the trap center. These two bundles merge into a single bundle (NA of 0.66 and 0.53″ active diameter), which then connects to a light pipe (fused quartz, 0.75″ diameter). A PMT counts the photons from the light pipe at room temperature. $C.E. = 3.5 \times 10^{-3}$ of the entire light collection system is measured when a Delrin ball (0.5″ in diameter), which is illuminated by a laser beam, acts as the light source at the trap center.

The molecular density n_{beam} is related to R_{scat} according to the Beer's law.

$$I_{\text{scat}} = h\nu R_{\text{scat}} \sim I_0 \times n_{\text{beam}} \times \sigma \times L. \tag{2.2}$$

Here, I_{scat} is the scattered laser power, $I_0 = 1.6\ \mu\text{W}$ is the detection laser power, and $\sigma = \frac{g_2}{g_1}\frac{\lambda^2}{4}\gamma_{\text{CaF}}\, g(\omega_0)$ is the photon-scattering cross section [64], where $\gamma_{\text{CaF}} = 6.4$ MHz is the nature linewidth of CaF (X-B transition), $g(\omega)$ is the line shape function defined by $\int_{-\inf}^{\inf} g(\omega)\delta\omega = 1$, and g_1 (g_2) is the degeneracy of the ground (excited) state. Based on the measured transverse spectrum in Fig. 2.22(a), $g(\omega_0) = 0.032$ MHz^{-1}.

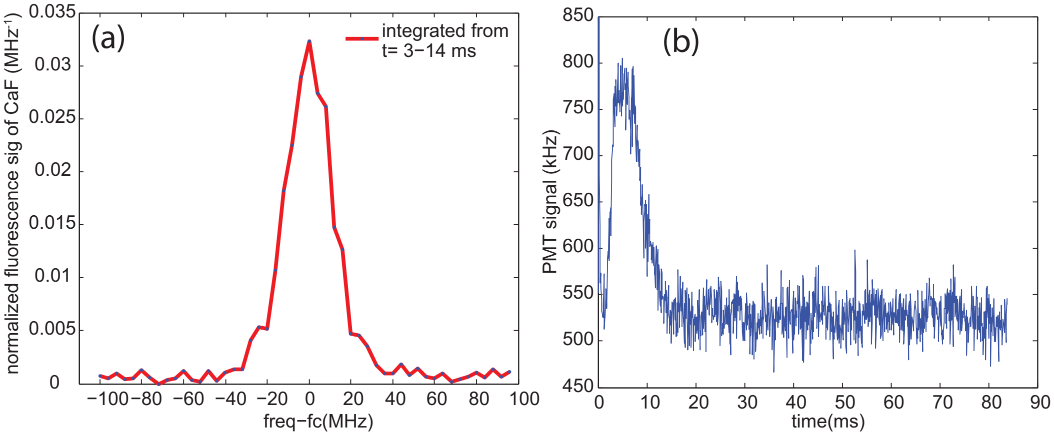

Figure 2.22: (a) Transverse (normalized) CaF beam spectrum at 30 cm. (b) Resonant CaF signal detected by PMT is recorded by a Multichannel Scaler Counter (MCS).

Using Eq. 2.1 and Eq. 2.2, and taking $g_1 = g_2$, we can obtain the CaF density profile. Finally, we can estimate the total number of the CaF reaching the trap midplane as follows.

$$N_{\text{downstream},CaF} = \int n_{\text{beam}}(t) \times A_{\text{beam}} \times v_f \delta t, \tag{2.3}$$

where $A_{\text{beam}} = \frac{\pi}{4} L_{beam}^2 = 12.6\ \text{cm}^2$ is the CaF beam area at the trap midplane and the integration duration is the entire molecular pulse. Assuming $v_f = 65$ m/s, we end up with $N_{\text{downstream},CaF} = 1.3 \times 10^8$ molecules/pulse with 4 mJ YAG energy at 2 Hz and 1.25 sccm ^{3}He flow. Here, we assume the collection efficiency of the molecular beam to be $C.E. = 3.5 \times 10^{-3}$.

2.4.4 CaF ($N = 0 - 2$) beam distributions

For all of the trap loading experiments, we keep the size of the 1st aperture to be 5 mm in diameter and use ^{3}He as the buffer gas. In addition, we use the

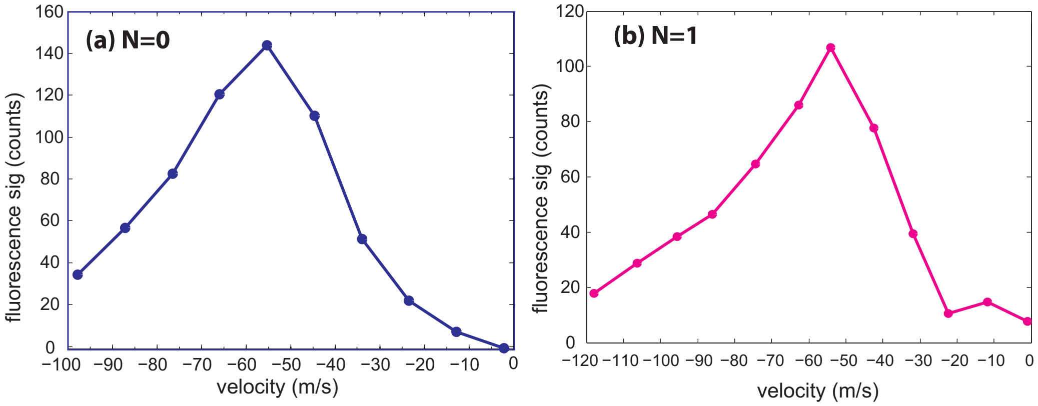

Figure 2.23: Longitudinal velocity distribution of CaF in $N = 0$ (a) and $N = 1$ state (b). $N = 1$ is detected via the $R_1(3/2) = 564.642474$ THz line of the $X - B$ transition. YAG energy is 5 mJ at 2Hz; flow is 1.25 sccm.

sputtering target from American Elements, which spills less dusts during ablation. CaF molecules in the lowest three rotational states are observed 30 cm downstream. A peak forward velocity of $v_f = 55$ m/s (velocity width of ~ 45 m/s) is measured for both $N = 0$ and $N = 1$ state, as shown in Fig. 2.23, and $v_f = 65$ m/s is measured for $N = 2$. Both $N = 0$ and $N = 1$ states have roughly the same beam intensity while $N = 2$ state is not as bright as the other two states.

For the trap loading experiment, we can capture a specific velocity class of CaF, depending on its internal state. We will elaborate this point in the next chapter. Fig. 2.24 plots the CaF signal with a specific longitudinal velocity within the capture velocity for these three rotational states. We notice that the number of slow moving $N = 2$ is less than $N = 0$.

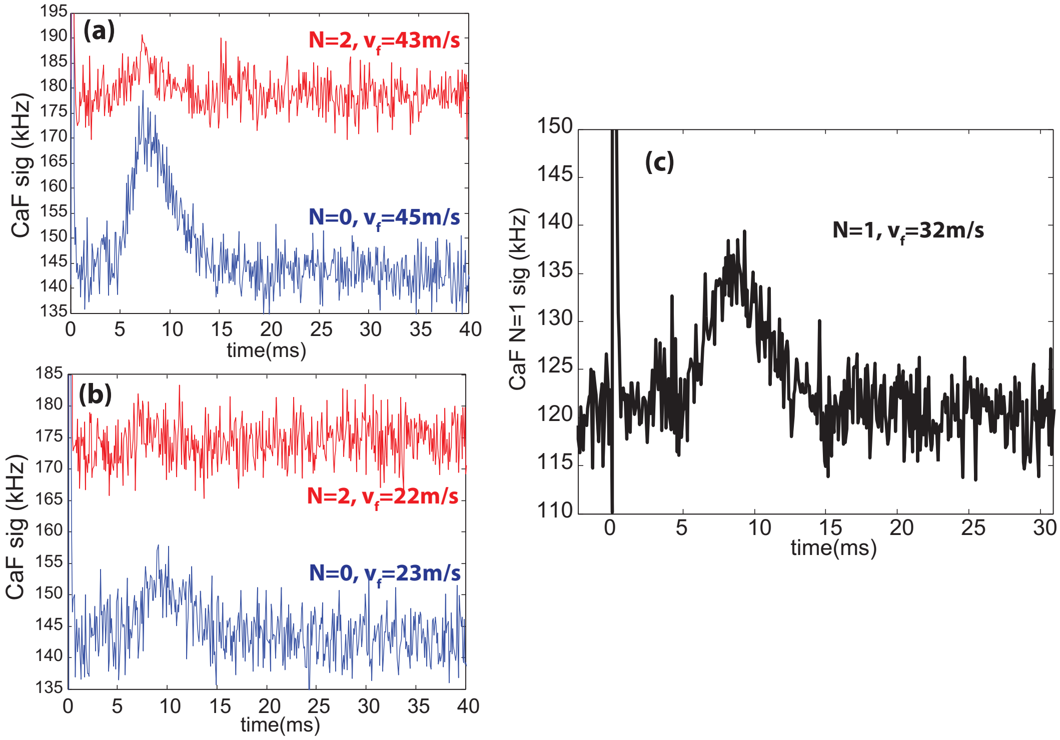

Figure 2.24: CaF signal at a certain longitudinal velocity for three rotational states. YAG energy is 5 mJ at 2Hz; ^{3}He flow is 1.25 sccm. CaF ($N = 2$) is detected via the $R_1(5/2) = 564.662048$ THz line of the $X - B$ transition.

Chapter 3

Optical loading and magnetic trapping of molecules

By ejecting hot molecules into a buffer-gas cell sitting inside a magnetic trap, traditional buffer-gas loading enabled magnetic trapping of four molecular species. The number of He-molecule elastic collisions (~ 100) necessary for thermalization [65, 66] requires an initial buffer-gas density of $n_0 \sim 10^{15}$ cm^{-3} inside the cell. After loading, molecules are in thermal contact with the buffer gas and will migrate to the trap center to form a trapped cloud. These two processes, which are fundamental to this method, limit buffer-gas trapping to magnetic species with a ratio of elastic to inelastic cross sections of $\gamma_{\mathrm{col}} > 10^4$ [43]. For $\gamma_{\mathrm{col}} < 10^3$, the molecules will change their spin projection and leave the trap before full trapping is achieved.

Thermal isolation of the trapped molecules requires the buffer gas to be removed quickly, before the molecules are lost through spin depolarization or evaporation processes. The biggest hurdle for achieving rapid thermal isolation is the helium film that coats the cell wall, which limits the ultimate background pressure. Cryogenic valves and an open cell geometry have been implemented successfully for rapidly pumping out the buffer gas [51, 67]. Going down to a dilution refrigerator temperature eventually freezed the He and led to the realization of Bose-Einstein condensate of metastable He [67]. However, it's technically challenging to introduce chemically diverse molecules into a dilution refrigerator other than using laser ablation.

Buffer-gas molecular beam, as described in Chapter 2 of this thesis, has all the generality of buffer-gas cooling. Using such beams gains the advantage over in-cell buffer-gas loading in that molecules can be trapped in a low background gas region where the helium film is absent. Given that we have produced slow CaH beam with $v_{\mathrm{f,CaH}} = 65$ m/s (velocity width of 40 m/s) and CaF beam with $v_{\mathrm{f,CaH}} = 55$ m/s (velocity width of 45 m/s), this allows for directly loading molecules into a magnetic trap with a depth of 4.9 T (3.3 K for 1 μ_B species), because the velocity spread includes molecules with low enough energies to be slowed and trapped.

The challenge for loading a slow beam of molecules into a conservative trap lies in achieving irreversible and dissipative trap loading. The optical pumping scheme we use is inherently irreversible and the spontaneously emitted photons dissipate the molecular energy. This type of irreversible and dissipative loading scheme was first utilized in Ref. [52] to optically pump laser cooled caesium atoms to the high-field seeking state ($F = 3, m_F = 3$) for loading an ac magnetic trap. A laser cooled chromium (Cr) beam with a velocity of 1 m/s has been continuously loaded into a hybrid optical and magnetic trap [53], where on average 6 photons are scattered to pump Cr from the low-field seeking $m_J = 3$ state to the high-field seeking $m_J = -3$

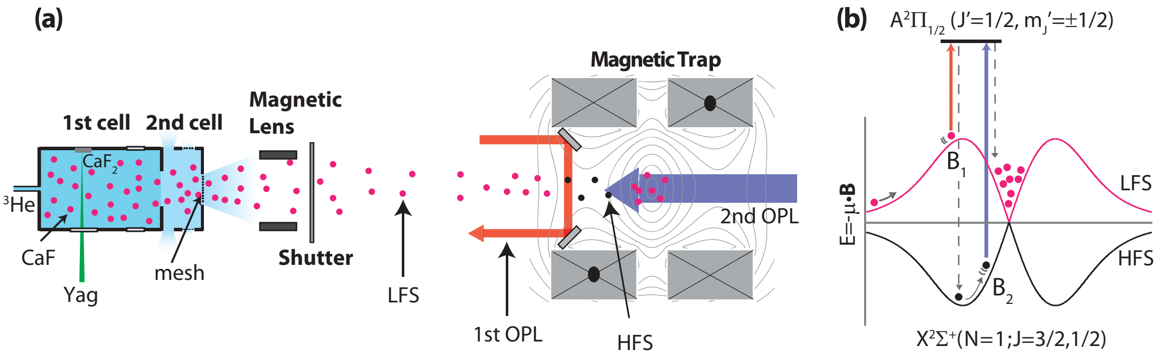

Figure 3.1: a) Schematic of the trap loading apparatus (not to scale). Slow CaF beam produced from a two-stage cell is focused by a magnetic lens (at 6 cm downstream) and then enters a magnetic trap locating at 30 cm. Two optical pumping lasers (OPL) are used to achieve irreversible loading-one interacts with the LFS near the saddle point; the other with the HFS inside the trap. A cryogenic shutter in between the magnetic lens and trap blocks the buffer gas after trap loading. (b) Optical loading scheme for $^2\Sigma^+$ $(N = 1)$ molecules into a magnetic trap. Potentials experienced by the LFS and HFS are represented in pink and black curves.

state. NH molecules in the $a^1\Delta$ state have been Stark decelerated to 20 m/s, and optically pumped to the electronic ground state $X^3\Sigma^-$ for loading a static magnetic trap [68].

Fig. 3.1(a) illustrates the schematic of the apparatus of our trap loading experiment, which consists of the two-stage source, a magnetic lens for collimating the molecules, and a superconducting magnetic trap. A cryogenic shutter in between the magnetic lens and trap can be closed up in a time as short as 10 ms. This shutter can block the helium beam after trap loading. For $^2\Sigma$ molecules, the electronic spin is decoupled from the molecular axis. To first order, the energy of $^2\Sigma$ molecules in the magnetic field can be expressed as $U = -\vec{\mu} \cdot \vec{B} = g_S \mu_B m_S |\vec{B}| = \pm\mu_B |\vec{B}|$, where $m_S = \pm 1/2$ is the projection of electronic spin along the magnetic field direction.

Molecules in the $m_S = 1/2$ state have a lower energy at lower fields, and hence we call molecules in this state low-field seekers (LFS). In contrast, molecules in the $m_S = -1/2$ state have a lower energy at larger fields and are called high-field seekers (HFS).

When entering the trap, the LFS lose their kinetic energy while climbing up the potential hill, as illustrated in Fig. 3.1(b). The first optical pumping laser (OPL), resonant with the LFS near the saddle (B_1), optically pumps CaF to HFS via the $X^2\Sigma^+(v = 0) \rightarrow A^2\Pi_{1/2}(v' = 0)$ transition at 606 nm. The HFS proceed to the trap center, get further decelerated, and are pumped by the 2nd OPL to the trappable state (LFS) at B_2. The spontaneously emitted photons during the pumping process render this scheme irreversible and dissipate the molecular energy.

In this chapter, we will first demonstrate the state manipulation of CaF, which is a necessary step for trap loading. We spectroscopically resolve the LFS and HFS in the field and determine the frequency of the optical pumping lasers to deplete the molecules (Sec. 3.1). When conducting optical pumping spectroscopy, we observe avoided crossings of CaF in the magnetic field, which have been neglected in the literature and prevent molecules from being confined by the maximum field at the edge of the trap. In Section 3.2, we will discuss the capture velocity for CaF in different rotational states. After establishing the trap strength at which we can operate, we demonstrate full state manipulation by pumping LFS→HFS→LFS for CaF ($N = 0$), and the slowing of a CaF ($N = 1$) beam (Sec. 3.3). Finally, we describe trapping results for CaF in $N = 0$ and $N = 1$ states, and present the trapping of CaH ($N = 0$) molecules, in Sec. 3.4 to Sec. 3.6.

3.1 Optical pumping spectroscopy

3.1.1 Spectroscopically resolved LFS and HFS molecules

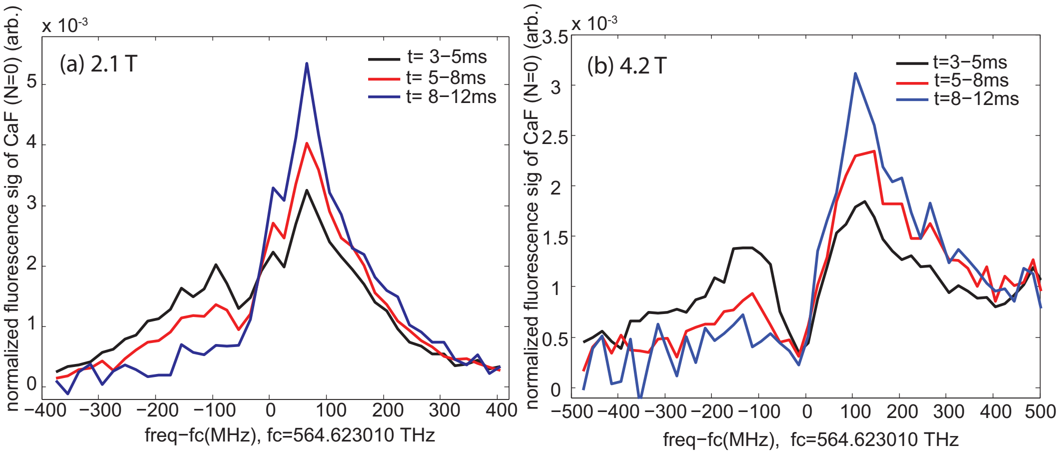

Figure 3.2: Spectra of CaF ($N = 0$) beam at 30 cm downstream when the trap is at 2.1 T (a) and 4.2 T (b). The frequency reference, f_c, is the zero field resonance of the $\mathrm{R}_1(1/2)$ line of the $X \rightarrow B$ transition.

CaF present in the trap midplane is detected via the $X^2\Sigma^+(v = 0) \rightarrow B^2\Sigma^+(v' = 0)$ transition at 531 nm (Fig. 2.17). Since the electronic spin is decoupled from the molecular axis in the $B^2\Sigma^+$ state, the Zeeman broadening is minimized by probing the molecules using the $X^2\Sigma^+ \rightarrow B^2\Sigma^+$ transition. This transition was utilized in Ref. [69] to sensitively detect CaH ($X^2\Sigma^+$) in the magnetic trap. Fig. 3.2 presents spectra of CaF ($N = 0$) with the trap at 2.1 T (Fig. 3.2(a)) and at 4.2 T (Fig. 3.2(b)). The spectral shape changes over the time after ablation. Immediately after ablation, molecules in the cell thermalize with the buffer gas in $\sim$ 2 ms (See Fig. 2.7). This results in an initially fast beam velocity that decreases with time. (We note that all of the longitudinal velocity measurements presented in Ch. 2 were the average beam velocity over the entire molecular pulse time period.) The magnetic lens focuses the LFS while defocusing the HFS as the molecules traverse from the cell to the trap region. The HFS are attracted to the high fringing fields of the magnet when approaching the trap. Both of these effects are more pronounced for slower molecules. Therefore, the relative populations of the LFS to the HFS as measured in the trapping region increase over time as the beam gets slower after ablation. We assign the peak at the blue (red) detuned frequency relative to the zero field resonance, f_c, as the LFS (HFS) molecules.

3.1.2 Optical pumping spectroscopy

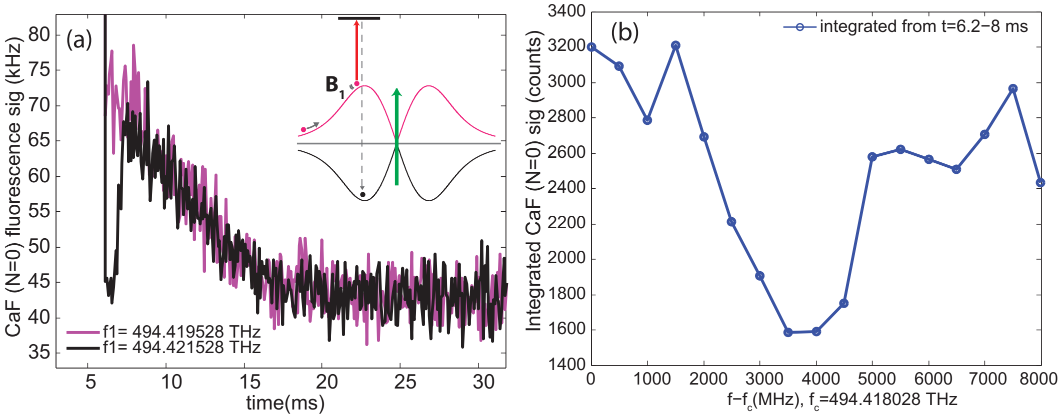

Figure 3.3: Optical pumping spectroscopy for LFS of CaF($N = 0$) at the saddle ($B_1 = 2.1$ T). (a) LFS signal at two pumping laser frequencies. The pumping laser is applied between $0-6$ ms. Signal depletion is seen for one of the frequencies between $6-7$ ms. (b) Integrated signal versus the pumping laser frequency. A minimum signal corresponds to the resonant frequency of the pumping laser.

Since the spin-orbital interaction $A_v = 2133$ GHz for CaF in the electronic excited ${}^2\Pi_{1/2}$ state [70] is much larger than the magnetic field interaction (corresponding to an energy of ~ 100 GHz at 5 T), the electronic spin is always fully coupled to the molecular axis in our experiment. The magnetic dipole moment of the ${}^2\Pi_{1/2}$ state

(Hund's case (a)) can be approximated as [71]

$$\mu = (\Lambda + 2\Sigma)\mu_B = 0, \tag{3.1}$$

where $\Lambda = 1$ ($\Sigma = -1/2$) is the component of the electronic orbital (spin) angular moment along the internuclear axis. In addition, since the electronic spin in the ${}^2\Sigma^+$ state is, in contrast, fully decoupled from the molecular axis, the projection of the electronic spin can be changed with an efficiency of order unity after the spontaneous emission during a $X \leftarrow A$ transition.

The energy of the LFS (HFS) in ${}^2\Sigma^+$ state is $U = \mu_B B$ (-$\mu_B B$), and hence the optical pumping transition frequencies for the LFS and the HFS are

$$f_{LFS}(B) = f_0 - \frac{\mu_B B}{h}, \tag{3.2}$$

and

$$f_{HFS}(B) = f_0 + \frac{\mu_B B}{h}, \tag{3.3}$$

where f_0 is the $X^2\Sigma^+ \rightarrow A^2\Pi_{1/2}$ transition frequency at zero field.

To perform optical pumping spectroscopy for the LFS, we fix the detection laser frequency to address the LFS line as described above. The frequency of the optical pumping laser is scanned around the predicted value based on Eq. 3.2. Fig. 3.3(a) shows the LFS signals of CaF ($N = 0$) at a location 30 cm downstream from the beam cell. The optical pumping laser is switched on between $0 - 6$ ms after ablation and the LFS are seen to be depleted at the resonance frequency between $6 - 7$ ms after ablation (black trace). The integrated signal between $6.2 - 8$ ms (where the depletion is most prominent) versus the pumping laser frequency is depicted in Fig. 3.3(b). The minimum signal in the pumping spectrum corresponds to the resonant frequency of the optical pumping laser.

We apply optical pumping spectroscopy to both the LFS and HFS of CaF ($N = 0$) in different field strengths up to 4 T. We also use two lines, Q_1 and R_1, of the $X - A$ transition to pump the molecules. The resonance frequencies mapped out at different fields are shown in red squares in Fig. 3.4(a). As a comparison, we plot the estimated pumping frequencies based on Eq. 3.2 and Eq. 3.3 in blue traces using the Q_1 line and black traces using the R_1 line. The measured values for the HFS agree with the simple linear dependence on the field. However, the measured frequencies for the LFS change their slope from $df/dB = -\mu_B/h$ to $df/dB = \mu_B/h$ at a field of 2.2 T, indicating there is an avoided crossing.

3.1.3 Avoided crossing of CaF

We plot the Zeeman levels of CaF for $N = 0 - 4$ in Fig. 3.5, where the fine and hyperfine interactions are ignored for now and the Hamiltonian is given by

$$H = B_v \vec{N}^2 + g_S \mu_B B_Z T^1_{p=0}(\vec{S}), \tag{3.4}$$

where $B_v = 0.342488\ \mathrm{cm}^{-1} = 10.27$ GHz is the rotational constant of CaF in the $X^2\Sigma^+$ state [61] and T^k_p is an irreducible spherical tensor operator. In addition, the direction of the magnetic field defines the space-fixed, $p = 0$ (or Z), direction [72]. We notice that the levels of the LFS of the $N = 0$ state cross with the HFS of the $N = 2$ state at roughly 2.2 T. This happens to be given by $B_{\text{avoided}} = (E(N = 2) - E(N = 0))/2\mu_B$, where $E(N)$ is the rotational energy. Our measured data indicates these level crossings are true avoided crossings.

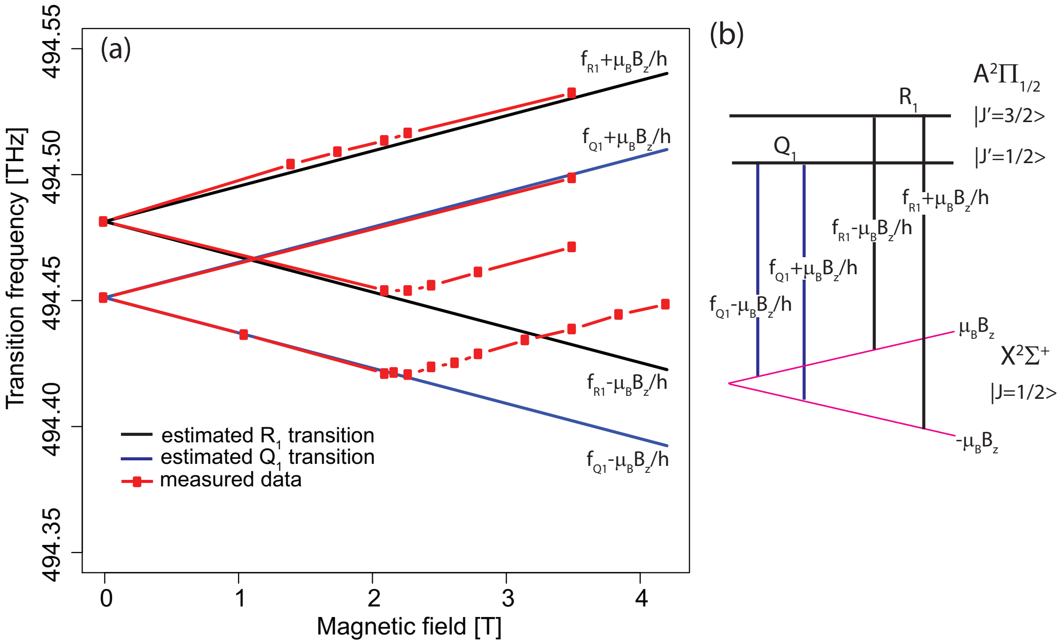

Figure 3.4: (a) Measured resonance frequencies of optical pumping lasers for LFS and HFS of CaF ($N = 0$) are shown in red squares. Expected resonant frequencies according to Eq. 3.2 and Eq. 3.3 using Q_1 (R_1) line are plotted in blue (black) traces. Here, f_{Q1} and f_{R1} are the transition frequencies at zero field. (b) Simplified Zeeman level diagram for the optical pumping scheme assuming both the energy levels of the LFS and HFS shift linearly with field.

However, we note that these avoided crossings may be overlooked in the literature. When measuring the Zeeman transition between $X^2\Sigma^+$ and $A^2\Pi_{3/2}$ inside a buffer-gas cell under a constant magnetic field, Reference [73] assumes that the levels of the ${}^2\Sigma^+$ state have a linear dependence on the magnetic field and obtains good agreement between the measured data and theoretical calculations up to 4 T. When conducting an experiment in a buffer-gas cell at a temperature comparable to the rotational splitting of CaF, the LFS of the $N = 0$ state and the HFS of the $N = 2$ state may be equally populated through collisions. This is different from conducting a Zeeman shift measurement in the beam, where the molecules are prepared in a specific quantum state and the He-molecule collisions are scarce at the location we conduct the measurement.

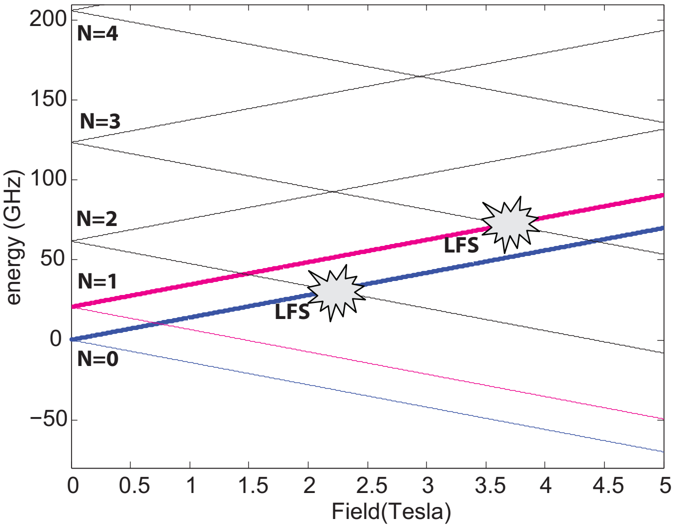

Figure 3.5: Calculated Zeeman energy level diagram of CaF ($N = 0 - 4$). Fine and hyperfine interactions are ignored here.

To know if the level crossings are true avoided crossing, we need to consider both the fine and hyperfine interactions in the Hamiltonian [72].

$$H = B_v \vec{N}^2 + g_S \mu_B B_Z T^1_{p=0}(\vec{S}) - g_I \mu_B B_Z T^1_{p=0}(\vec{I}) + \gamma_v T^1(\vec{N}) \cdot T^1(\vec{S}) + b_F T^1(\vec{S}) \cdot T^1(\vec{I}) + H_{dip}, \tag{3.5}$$

where $\gamma_v = 39.66$ MHz is the spin-rotational coupling [74], $b_F = 122.6$ MHz is the Fermi contact interaction ([74] and Eq. (8.511) of Ref. [72]), and H_{dip} is the spin-nuclear spin dipolar interaction. More explicitly,

$$H_{dip} = -g_S \mu_B g_N \mu_N \frac{\mu_0}{4\pi} \{ \frac{\vec{I} \cdot \vec{S}}{r^3} - \frac{3(\vec{I} \cdot \vec{r})(\vec{S} \cdot \vec{r})}{r^5} \}. \tag{3.6}$$

We diagonalize the energy matrix of Eq. 3.5 numerically by using the Hund's case (b) hyperfine-coupled basis, $|N, S = 1/2, J, I = 1/2, F, M_F\rangle$, and considering $N = 0$ and $N = 2$ states. Before showing the result, let's inspect the matrix element for H_{dip}, which is given explicitly by Eq. (8.259) in Ref. [72].

$$
\begin{aligned}
&< N, S, J, I, F, M_F | H_{dip} | N', S, J', I, F', M_F > \\
&\quad = \sqrt{\frac{10}{3}} c \delta_{F,F'} (-1)^{J'+F+I+1} \begin{Bmatrix} I & J' & F \\ J & I & 1 \end{Bmatrix} \\
&\quad \times [I(I+1)(2I+1)S(S+1)(2S+1)(2J+1)(2J'+1)]^{1/2} \begin{Bmatrix} J & J' & 1 \\ N & N' & 2 \\ S & S & 1 \end{Bmatrix} \\
&\quad \times (-1)^N [(2N+1)(2N'+1)] \begin{pmatrix} N & 2 & N' \\ 0 & 0 & 0 \end{pmatrix} \qquad (3.7)
\end{aligned}
$$

Here, we also use Eq. (8.515)-(8.516) of Ref. [72] to express the interaction strength with $c = 40.12$ MHz, which is the strength of the anisotropic electronic spin-nuclear spin coupling [74]. The last term in Eq. 3.7 mixes $N = 0$ and $N = 2$ states, causing the avoided crossing. Fig. 3.6 depicts the energy levels near B = 2.2 T, which shows avoided crossing levels.

Using Landau-Zener approximation [75], we can estimate the possibility of the LFS passing through one avoided crossing and remaining in the low-field seeking state, $P_{LFS}(t \to \infty)$:

$$P_{LFS}(t \to \infty) = e^{-\frac{2\pi\Omega^2}{\dot{\Delta}}}. \qquad (3.8)$$

Here, Ω is the strength of the interaction coupling the LFS and HFS, which is roughly equal to the size of the avoided crossing. $\dot{\Delta} = \delta\Delta/\delta t$ is the time derivative of the

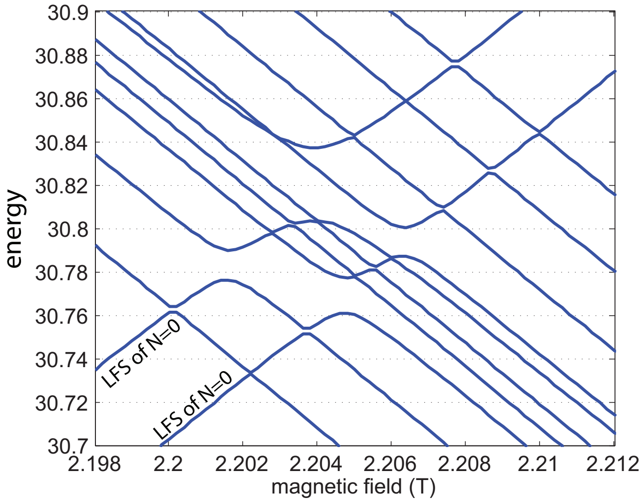

Figure 3.6: Calculated avoided crossings between the LFS of $N = 0$ and HFS of $N = 2$ around B=2.2 T. Two low-field seeking states of $N = 0$ have two different nuclear spin projection in the magnetic field.

frequency difference between the LFS and HFS.

$$\dot{\Delta} = \frac{2\mu_B \delta B}{h\delta t} = \frac{2\mu_B}{h}\frac{(\partial B/\partial x)\delta x}{\delta x/v} = \frac{2\mu_B}{h}\frac{\partial B}{\partial x} \times v, \tag{3.9}$$

where we take the slope of the energy versus magnetic field to be $\mu_B(-\mu_B)$ for LFS (HFS), $\partial B/\partial x \sim 1$ T/cm is the field gradient, and $v = 60$ m/s is the molecular velocity. Let's estimate the chance of LFS passing through a large gap of ~ 10 MHz estimated based on Fig. 3.6. By taking $\Omega = 10$ MHz, we can obtain $P_{LFS}(t \to \infty) \sim 0.02$. There are at least two large gaps with a size of 10 MHz for the LFS to overcome in order to remain in the low-field seeking state, yielding a small chance for finding the LFS ($N = 0$) at $B > 2.2$ T.

In contrast, there is no level crossings for the LFS of $N = 2$ below the maximum strength of the trap of 4.9 T (Fig. 3.5). We experimentally measure the Zeeman transition frequencies of the $N = 2$ state, which is shown in Fig. 3.7. We use the

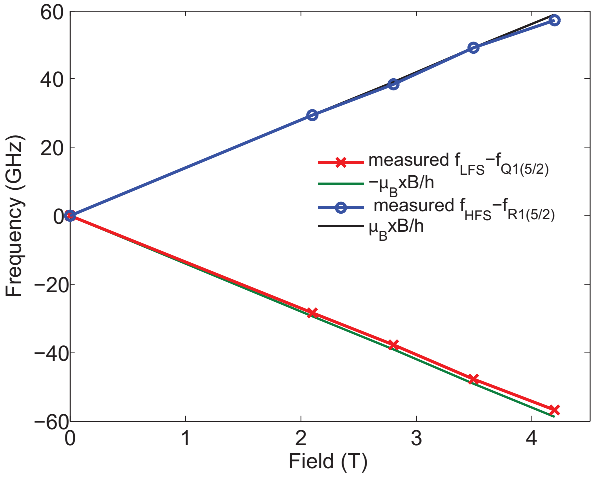

Figure 3.7: Measured Zeeman transition frequency for the LFS (HFS) of CaF ($N = 2$) relative to the $Q_1(5/2)$ ($R_1(5/2)$) line of the $X - A$ transition at zero field.

$Q_1(5/2)$ line of the $X - A$ transition for the LFS; $R_1(5/2)$ for the HFS. The measured transition frequencies follow a linear dependence in the field with slopes of $\pm\mu_B/h$ up to 4.2 T.

3.2 Capture velocity and optical pumping transition lines for CaF

The capture energy of our loading scheme (Fig. 3.1(b)) can be understood as follows. Only molecules with enough kinetic energy to climb up two potential hills can reach the trap center, setting the lower bound of the capture energy to be

$$E_L = \mu_B \times (2B_1 - B_2). \tag{3.10}$$

After deceleration, molecules with kinetic energy lower than the trap depth, $E_D \sim \mu_B \times (B_1 - B_2)$, can remain trapped. The capture energy is hence

$$E_L < E_f < E_L + E_D \Rightarrow \mu_B \times (2B_1 - B_2) < E_f < \mu_B \times (3B_1 - 2B_2), \tag{3.11}$$

where E_f is the kinetic energy of the molecules in the beam and we approximate the maximum field to be B_1. At the full strength of the trap with (B_1, B_2)=(4.9, 1.5) T, the corresponding capture velocity is $v_c = 40 - 47$ m/s for molecules with a mass of 59 amu. This range is close to the peak distribution of our CaF beam.

However, the avoided crossings of CaF described above inhibit the operation of the trap at its full strength for two reasons. When the LFS pass through these avoided crossings on their way to the saddle, they adiabatically turn into the HFS, which limits the amount of kinetic energy we can remove. After the LFS are loaded into the trap, the LFS orbit through these avoided crossings inside the trap and then turn into the HFS, which are expelled from the trap eventually. Therefore, we operate the trap at a field slightly below $B_{\text{avoided}} = (E(N+2) - E(N))/2\mu_B$.

B_1 is typically chosen to be the saddle point to remove the maximum amount of energy. With the same logic, we would choose $B_2 = 0$. However, the HFS are attracted to the magnet cask inside the trap, which would lead to a reduced loading efficiency. Therefore, there should be an optimal value for B_2, which is chosen according to the trajectory simulation and will be discussed in Ch. 5 in detail. If we choose (B_1, B_2) = $(2.17, 1)$ T for loading CaF ($N = 0$), the corresponding capture velocity is $v_c = 25.1 - 29.1$ m/s. According to Fig. 2.24, we do produce some CaF ($N = 0$) molecules moving within this velocity range.

For loading CaF ($N = 0$), we want to pump the molecules using the $Q_1(1/2)$

line (Fig. 3.4(b)) since the excited state $A^2\Pi_{1/2}(J' = 1/2)$ is less likely to decay to the $N = 2$ state compared to the $A^2\Pi_{1/2}(J' = 3/2)$ state. However, because the 2nd OPL at frequency f_2 spatially overlaps with the CaF beam, it may excite the LFS to $A^2\Pi_{1/2}(J' = 3/2)$ via the $R_1(1/2)$ line at certain fields B' (see Fig. 3.4(b)). This occurs when

$$f_2 = f_{Q1(1/2)} + \mu_B B_2/h = f_{R1(1/2)} - \mu_B B'/h. \tag{3.12}$$

where $f_{Q1(1/2)}$ and $f_{R1(1/2)}$ represent the transition frequencies at zero field. We can rewrite the above equation as follows:

$$\begin{aligned} & f_{R1(1/2)} - f_{Q1(1/2)} \\ & \quad = (E(J' = 3/2) - E(J' = 1/2))/h = 31.1\text{GHz} = \mu_B \times 2.22\ \text{T}/h \\ & \quad = \mu_B(B_2 + B')/h \\ & \quad \Rightarrow B' = (2.22\ \text{T} - B_2) \end{aligned} \tag{3.13}$$

Here, we use the energy splitting of $3B'_v = 31.1$ GHz between the $J' = 1/2$ and $J' = 3/2$ states [70]. If we choose $B_2 = 1$ T and use the Q_1 line for the 2nd OPL, we can optically remove the LFS at B'=1.2 T. We did observe this effect in the experiment. For this reason, we use the $Q_1(1/2)$ line for pumping the LFS and the $R_1(1/2)$ line for pumping the HFS, despite a lower branching ratio for decaying back to the $N = 0$ state.

For CaF ($N = 1$), the avoided crossing occurs at $B_{\text{avoided}} = 3.67$ T, giving a higher capture velocity than $N = 0$. Additionally, as pointed out by Ref. [46], the rotational leakage channel can be suppressed by driving a $N = 1 \rightarrow J' = 1/2$

transition (P_1 line in Fig. 2.17), leading to a more efficient state transfer than $N = 0$. We also need to consider the optical removal of the LFS due to the 2nd OPL laser. The field B' of this undesirable pumping for the LFS is given by $\mu_B(B_2 + B')/h = f_{Q1(3/2)} - f_{P1(3/2)} = (E(J' = 3/2) - E(J' = 1/2))/h = \mu_B \times 2.22\ \mathrm{T}/h$. If we can pump the HFS at $B_2 > 2.22$T using the P_1 line, the LFS would not be pumped away before reaching the saddle. Choosing (B_1, B_2)=(3.5, 2.3) T yields $v_c = 29.7 - 33.3$ m/s for $N = 1$, which is closer to the peak distribution than that for $N = 0$.

3.3 State manipulation

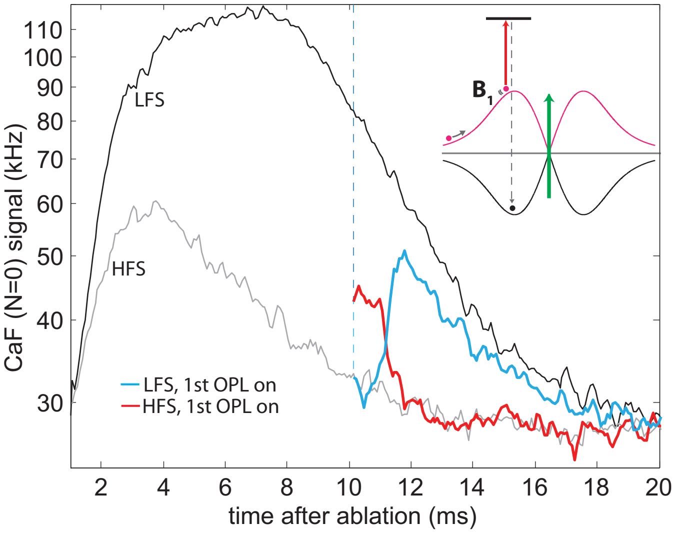

Figure 3.8: The LFS (HFS) of CaF ($N = 0$) detected at the trap midplane are shown in black (gray) without the 1st OPL. When the 1st OPL is turned on between $0 - 10$ ms, the PMT is overwhelmed with scattered photons. Blue and red traces represent the LFS and HFS signals when the 1st OPL is switched off (vertical dash line), demonstrating the state transfer from the LFS to HFS. Inset: schematic of the 1st optical pumping process with $B_1 = 2.17$ T. The transverse detection laser is through the trap midplane.

A key step for this optical loading scheme is to transfer the internal states of molecules in the magnetic field via optical pumping. In this section, we are going to show three measurements, including transferring LFS→HFS and LFS→HFS→LFS of CaF ($N = 0$), as well as slowing of CaF ($N = 1$).

To demonstrate the state transfer during the 1st pumping stage, we can inspect the LFS and HFS populations with and without the 1st pumping laser. Black and gray traces in Fig. 3.8 depict the LFS and HFS signals of CaF ($N = 0$) measured at the trap midplane without the 1st OPL. The LFS have a larger signal height and a longer duration than the HFS due to the magnetic lens and the trapping field. When the 1st OPL is applied between 0 and 10 ms, a dip between $10 - 11$ ms shown as blue trace in Fig. 3.8 represents the depletion of the LFS, which has been observed in Fig. 3.3(a) as well. After the pumping laser is turned off at the saddle, slow molecules take $1 - 2$ ms to reach the trap midplane, causing the LFS signal to recover after 11 ms. Meanwhile, additional HFS molecules (red trace in Fig. 3.8) appear between $10 - 11$ ms compared the case without pumping (gray trace), demonstrating the state transfer from LFS→HFS.

Full state manipulation is established with the addition of the 2nd OPL, as illustrated schematically in the inset of Fig. 3.9(a). The blue trace of Fig. 3.9(a) represents the LFS signal when the 2nd OPL pumps the HFS (between $9 - 10$ ms) at the saddle in addition to the 1st OPL laser. The replenishment of the LFS owing to the 2nd OPL is observed between $10 - 11$ ms, yielding an efficiency of 15% for transferring LFS → HFS → LFS. The measured efficiency is consistent with the branching ratio calculation on the states involved in optical pumping transition.

We have discussed how we choose transition lines and transition frequencies

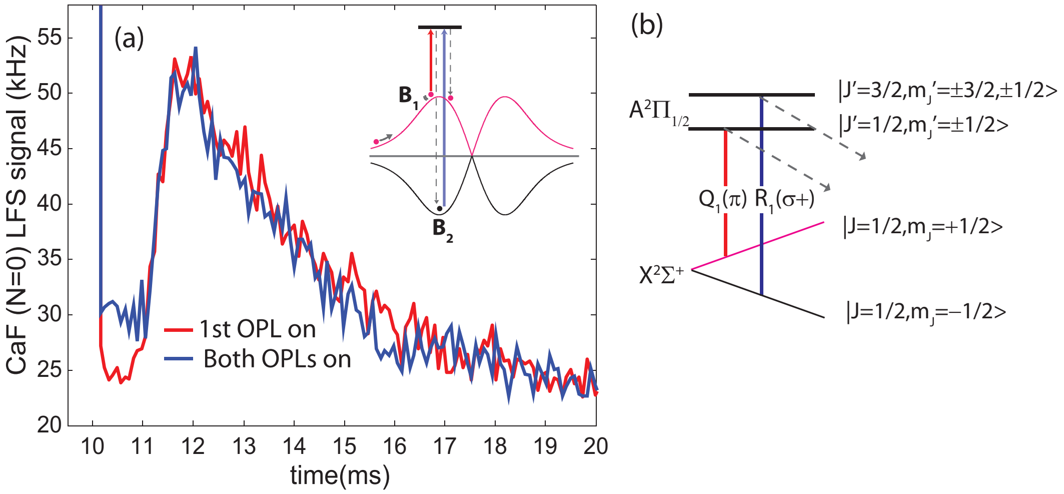

Figure 3.9: (a) Full state manipulation of CaF ($N = 0$) at 2.17 T. Switching the 2nd OPL on ($9 - 10$ ms) in addition to the 1st OPL ($0 - 10$ ms) pumps the HFS back and recovers the LFS signal between $10 - 11$ ms (blue trace). As a comparison, the red trace depicts the LFS with only the 1st OPL on. Inset: schematic of the two-stage pumping process with $B_1 = B_2 = 2.17$ T. (b) Transition lines and polarizations used for the state manipulation.

for the pumping lasers. Correct polarization is also essential for establishing state manipulation, especially for the 2nd OPL. Fig. 3.9(b) summarizes the parameters used for demonstrating state manipulation of CaF ($N = 0$). Definite polarizations are established by sending the OPLs through polarization beam splitter cubes, followed by waveplates before the apparatus. The magnetic field directions of the two pumping stages are roughly parallel to the molecular beam or magnetic bore axis. The 1st OPL is linearly polarized and its electric field direction is parallel to the magnetic field to drive $|J = 1/2, m_J = 1/2\rangle \rightarrow |J' = 1/2, m'_J = 1/2\rangle$ transition. Here, we assume the projection of the nuclear spin remains the same during the pumping process. The 2nd OPL is σ_+ polarized to drive $|J = 1/2, m_J = -1/2\rangle \rightarrow |J' = 1/2, m'_J = 1/2\rangle$ transition. In this way, the molecules can decay back to the LFS after spontaneous emission. By contrast, using a σ_- polarized 2nd OPL does not replenish the LFS.

We experimentally determine the handedness of the 2nd OPL by changing the angle of the $\lambda/4$ waveplate and monitoring whether the LFS can be replenished.

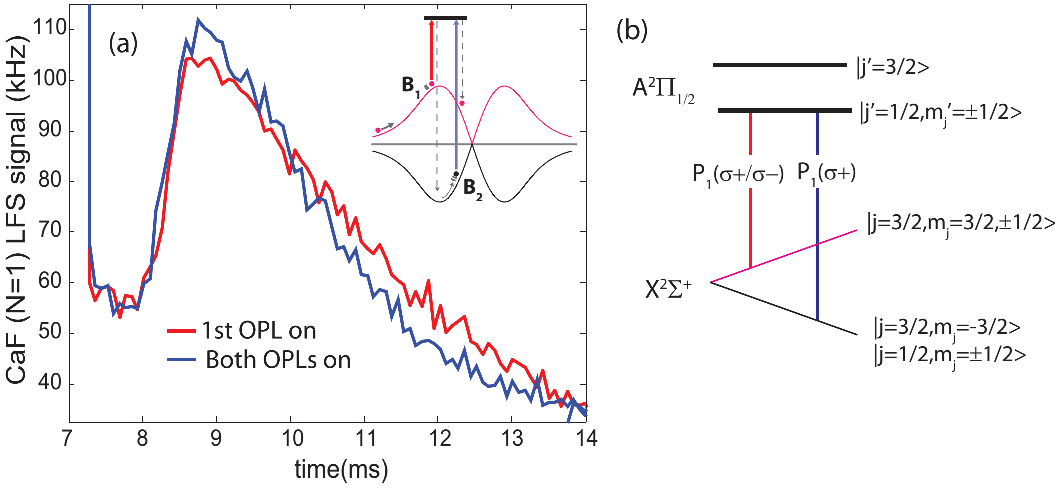

Figure 3.10: (a) Slowing of CaF ($N = 1$) beam using two-stage optical pumping. CaF ($N = 1$) is detected using the $P_1(3/2)$ line of the $X - B$ transition (see Fig. 2.17). The LFS signal with (without) the 2nd OPL is depicted in blue (red) trace. The 1st OPL is on between $0 - 7$ ms and the 2nd OPL is pulsed on between $4 - 7$ ms. Inset: schematic of the slowing process. $(B_1, B_2) = (3.5, 2.27)$ T. (b) Transition lines and polarizations used for the slowing measurement.

In demonstrating the full state manipulation experiment above, we do not slow down the molecules since $B_1 = B_2$. By pumping the HFS at fields closer to the trap center, we can remove some of the kinetic energy and achieve slowing of the molecular beam. We demonstrate the slowing process for the CaF ($N = 1$) beam with the trap at 3.5 T. The blue trace in Fig. 3.10(a) illustrates the LFS signal of $N = 1$ with the 2nd OPL resonant with HFS at $B_2 = 2.27$ T. We observe more LFS molecules at around 9 ms compared to the case without the 2nd OPL (red trace), indicating slowing of the molecular beam. We note that there are slightly less LFS between $10 - 14$ ms when turning on the 2nd OPL, which is attributed to the heating of the cell from the 2nd OPL. (The 2nd OPL lands directly on the beam cell.) We summarize the transition lines and polarizations of the two OPLs in Fig. 3.10(b). The polarization of the 1st OPL is perpendicular to the magnetic field so that a mixture of σ_+ and σ_- polarizations can pump the LFS. We notice that the depletion of the LFS of $N = 1$ is not as efficient as $N = 0$. There's no clear answer for why this is the case.

3.4 Magnetic trapping of CaF ($N = 1$)

To load CaF ($N = 1$) into the trap, we simply extend the time durations of the two OPLs to capture more molecules compared to the slowing case. Fig. 3.11(a) shows a time decay trace of trapped CaF ($N = 1$) at the resonant frequency and Fig. 3.11(b) plots a spectrum of the trapped CaF integrated over different time windows. The cryogenic shutter is not used for this data set. A decay time of $\tau_{loss} = 89$ ms in the trap is set by two factors. First, the continuously flowing ^{3}He gas (0.75 sccm) from the beam source can knock out the trapped molecules, as the trap depth $E_D = \mu_B(B_1 - B_2) \sim k_B \times 826$ mK is comparable to the temperature of the ^{3}He gas. The second effect is the result of probing trapped CaF via the $X^2\Sigma^+(v = 0, N = 1) \rightarrow B^2\Sigma^+(v' = 0, N' = 0)$ transition. After a few scattering events, the molecules can decay to other hyperfine states within the LFS manifold. These states stay trapped but remain dark to the probe laser.

To estimate the number of trapped CaF ($N = 1$) molecules, we need to estimate the size of the trapped cloud based on the Monte-Carlo trajectory simulations, which will be explained in detail in Ch. 5. According to the simulation results as shown

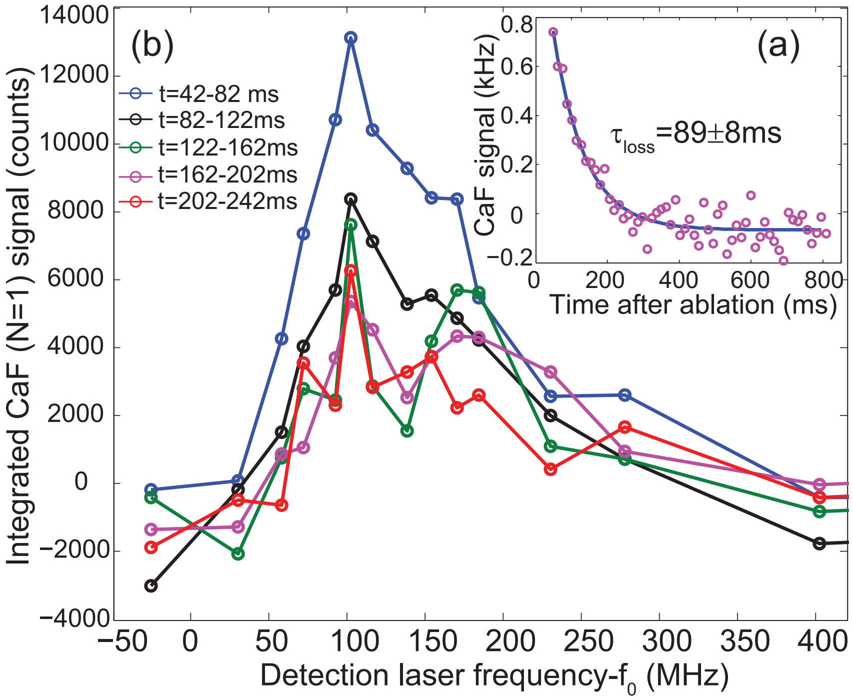

Figure 3.11: (a) Time decay of the trapped CaF ($N = 1$) signal at the resonant frequency, relative to a background count rate taken before ablation. The buffer-gas flow is 0.75 sccm; $(B_1, B_2) = (3.5, 2.4)$ T. A single exponential fit gives a decay constant of 89 ± 8 ms. 1st OPL is on between $2 - 17$ ms; 2nd OPL on between $8 - 17$ ms. (b) Spectrum of trapped CaF ($N = 1$) for different time intervals relative to ablation with a He flow of 1.25 sccm; $(B_1, B_2) = (3.5, 2.27)$ T. f_0 is the resonance frequency of the $P_1(3/2)$ line of the $X - B$ transition measured at zero field (see Fig. 2.17).

in Fig. 3.12, the simulated density distributes between $r_1 = 3$ mm to $r_2 = 27$ mm (FWHM) along the trap midplane. The detection laser has a diameter of 2 mm with a power of $I_0 = 14$ μW. We use *LightTools* package to simulate the collection efficiency, $C.E.$, of the two fiber bundles using two cylindrical light sources (each has a diameter of 2 mm and is placed 3-27 mm symmetrically from the trap center), giving $C.E. = 1.1 \times 10^{-3}$. To consider the losses due to light attenuation in real materials, a finite packing ratio of the fiber bundle, and the coupling between the fiber bundle and light pipe, we compare the measured $C.E. = 3.5 \times 10^{-3}$ of the entire collection system

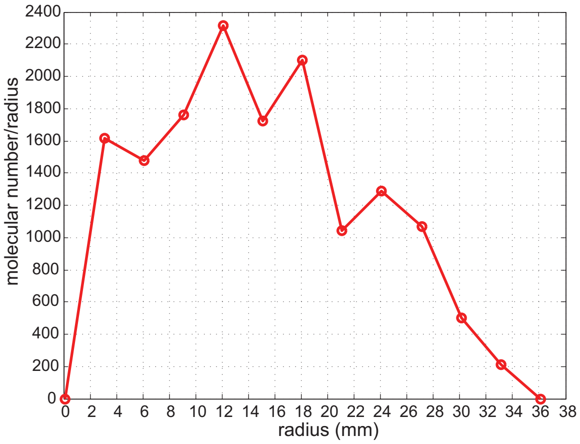

Figure 3.12: Simulated density distribution of CaF($N = 1$) along the radial direction of the trap midplane. Simulation conditions: CaF beam with $(v_f, dv_l, dv_t) = (55, 40, 56)$ m/s and $(B_1, B_2) = (3.5, 2.42)$ T. Here, dv_l and dv_t are the longitudinal and transverse beam velocity widths.

using a Delrin ball as the light source (Sec. 2.4.3) to a simulated $C.E. = 4.6 \times 10^{-3}$ of the two fiber bundles using a 0.5$''$ source in *LightTools*, giving a scaling factor of 0.76. The collection efficiency of the entire collection system for the trapped cloud should be $C.E. = 1.1 \times 10^{-3} \times 0.76 = 0.87 \times 10^{-3}$.

Other experimental parameters used to detect trapped CaF are as follows. The PMT has a quantum efficiency of $Q.E. = 18\%$ and the measured trapped spectrum has a width of $\Gamma_{\mathrm{CaF}} = 115$ MHz. We record a trapped CaF signal of $R_{resonance} = 0.81$ KHz at the resonance frequency and at a delay of 23 ms after the loading process. Since the light collection efficiency is estimated for the molecular cloud within the FWHM of the density distribution, we should use an average signal of the spectrum (FWHM), $R = R_{resonance} \times 0.81 = 0.66$ kHz, to estimate the number of trapped CaF molecules.

The laser power scattered out of the trapped molecules can be written as

$$I_{\text{scat}} = I_0 - I = I_0 \times (1 - e^{-n\sigma 2(r_2 - r_1)}) \sim I_0 \times n \times \sigma \times L, \tag{3.14}$$

where $\sigma = \sigma_0 \times \frac{\gamma_{\text{CaF}}}{\Gamma_{\text{CaF}}}$ is the optical scattering cross section. Here, $\gamma_{\text{CaF}} = 6.4$ MHz is the nature linewidth of the $X - B$ transition and $\sigma_0 = \frac{\lambda^2}{4}$.

The measured count rate and the scattered laser power is related by

$$R = \frac{I_{\text{scat}}}{h\nu} \times C.E. \times Q.E. \tag{3.15}$$

Therefore, an average signal of $R = 0.66$ kHz corresponds to a density and total number of trapped CaF($N = 1$) of

$$\begin{aligned} n &= \frac{I_{\text{scat}}}{I_0} \frac{4\Gamma_{\text{CaF}}}{\lambda^2 \gamma_{\text{CaF}}} \times L^{-1} \sim 6 \times 10^2 \text{ cm}^{-3} \\ N &= \frac{\pi}{3}(r_2^3 - r_1^3) \times n \sim 1.2 \times 10^4. \end{aligned} \tag{3.16}$$

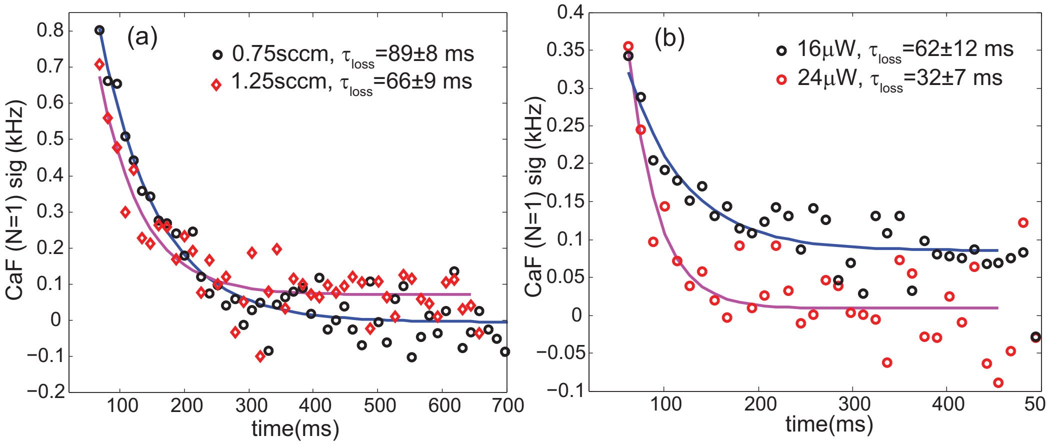

Figure 3.13: (a) Time decay of trapped CaF ($N = 1$) signals for two buffer-gas flows. Detection power is fixed at 14 μW; Yag at 1 Hz. (b) Time decay of CaF($N = 1$) signals for two detection powers. Flow is fixed at 1.25 sccm; YAG at 1 Hz.

Since the signal of $R = 0.66$ kHz is measured at a delay of 23 ms relative to the loading process, the peak signal can be inferred based on the decay time constant of 89 ms. Therefore, $n_{peak} = n \times e^{23/89} = 7.7 \times 10^2$ cm^{-3} and $N_{peak} = N \times e^{23/89} = 1.6 \times 10^4$.

We experimentally change the buffer-gas flows and detection laser powers to investigate their effects on the trap lifetimes, as shown in Fig. 3.13. Both increasing flows and detection laser powers can lead to a reduced trap lifetime. We note that the optical pumping time constant due to the detection laser is on the order of 500 ms (see Sec. 3.4.1). For the case without shutter, collisions between the He beam and the trapped CaF limit the decay time at a detection power of 14 μW.

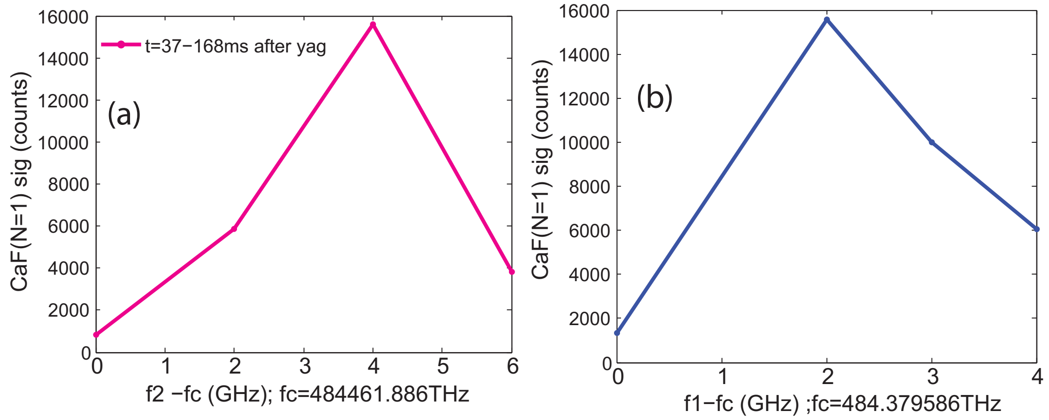

Figure 3.14: (a) Trapped CaF ($N = 1$) signal versus 2nd OPL frequency. Resonant frequency corresponds to $B_2 = 2.42$ T. 1st OPL frequency is fixed to pump the LFS at the saddle point (3.5 T). (b) Trapped CaF ($N = 1$) signal versus 1st OPL frequency. 2nd OPL frequency is fixed at $f_2 = 494.465886$ THz, which is resonant with the HFS at 2.42 T. Flow = 1.25 sccm; YAG (5 mJ) at 1 Hz.

We plot the loaded CaF ($N = 1$) signal versus the frequency of the 2nd OPL in Fig. 3.14(a) and 1st OPL in Fig. 3.14(b). There is a clear dependence of the loaded signal on the OPL frequencies. The maximum signal occurs when the 1st OPL pumps the LFS at $B_1 = 3.5$ T and 2nd OPL pumps the HFS at $B_2 = 2.42$ T.

3.4.1 Trap lifetime with cryogenic shutter

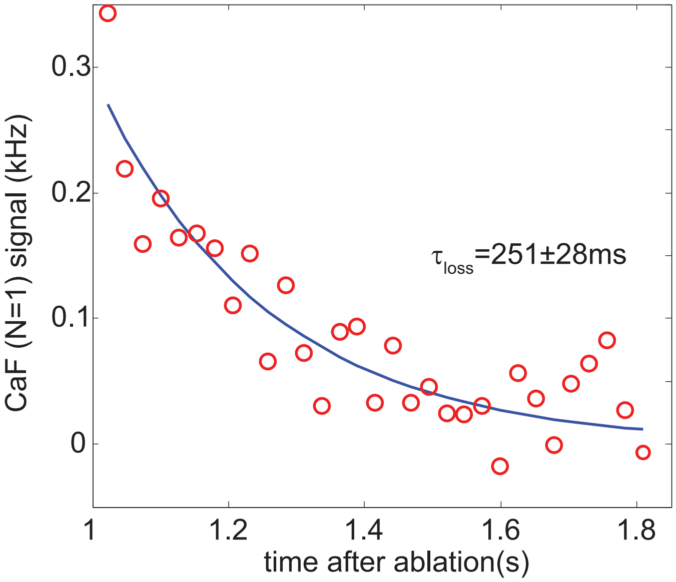

Figure 3.15: Trapped CaF ($N = 1$) signal after the shutter is closed. The detection laser (14 μW power) is turned on at 1 s. Flow = 0.5 sccm; Shutter actuated at 0.5 Hz (same with YAG repetition rate) with an opening duration of 100 ms.

The main limitation for achieving longer trap lifetimes is the net buffer-gas density in the trap. Reducing the background gas collisions, including decreasing the buffer-gas flow and blocking the buffer-gas beam after the molecules have traversed the loading zone, increases the lifetime. After loading the molecules at a low buffer-gas flow of 0.5 sccm, we close the shutter and switch on the detection laser at 1 s. The obtained CaF signal is shown in Fig. 3.15. The observed lifetime increases to $\tau_{loss} = 251$ ms, by a factor of ~ 3 compared to Fig. 3.11(a).

The effect of optical pumping from the probe laser can be removed by turning it on at different delay times. In Fig. 3.16(a), we plot the integrated signal versus the time when the detection laser is switched on with a low flow of 0.5 sccm, and a low loading repetition rate of 0.5 Hz. We determine a fitted decay time constant of $\tau_{BG} = 527$ ms, which is purely limited by collisions with the ^{3}He gas at 4 K inside the trap. As a comparison, we increase the flow and loading repetition rate to 0.75 sccm and 1 Hz, respectively. The obtained trap lifetime of $\tau_{BG} = 255$ ms, as shown in Fig. 3.16(b), is a factor of 2 smaller than the previous conditions (Fig. 3.16(a)).

There are two sources of the background gases. One is the buffer-gas beam which is not completely blocked by the shutter, causing the trap lifetime to be inversely proportional to the flow. If this is the case, increasing the flow from 0.5 sccm to 0.75 sccm should cause the lifetime to reduce by a factor of 1.5. The other is the density of helium due to re-scattering inside the magnet ("built-up density"), which gives an overall helium gas proportional to the flow and the ratio of shutter opening time to the period of the loading sequence. After considering the loading repetition rate and the opening duration of the shutter, we expect the trap lifetime to reduce by a factor of 3 if the built-up density is the dominant source.

Since the reduction of the observed trap lifetime can not be explained by either one of the two sources alone, we suspect both can contribute to the background helium density in the trap. Potential ways to improve the trap vacuum include implementing a better differential pumping design and increasing the area of cryogenic pumps inside the trap. Right now only 34% of the area inside the magnet is covered with charcoal sorbs, which locate between 34.6 cm and 44.5 cm from the cell exit aperture.

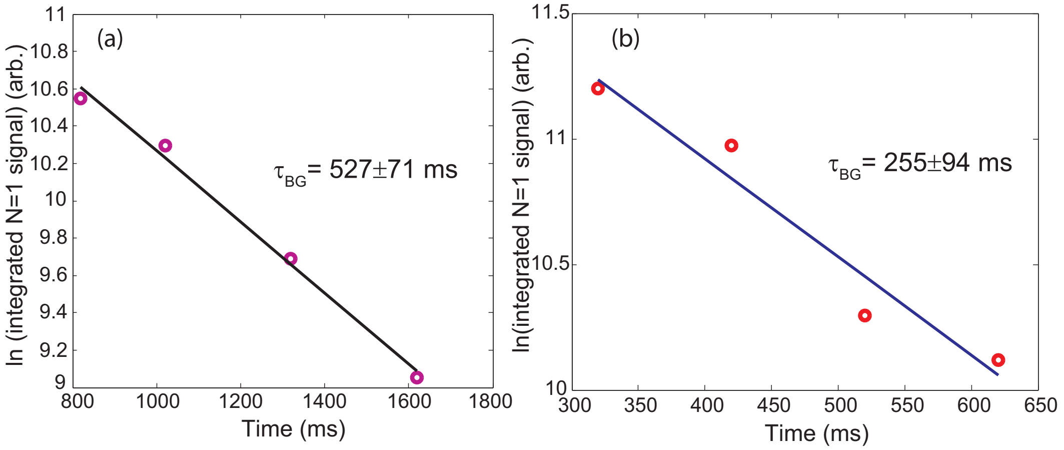

Figure 3.16: Signals of CaF ($N = 1$) integrated over 210 ms as a function of time after ablation at which the detection laser is switched on. (a) Data taken when the flow is 0.5 sccm and shutter is actuated at 0.5 Hz (YAG repetition rate) with an opening duration of 100 ms. (a) Data taken when the flow is 0.75 sccm and shutter is actuated at 1 Hz (YAG repetition rate) with an opening duration of 100 ms.

3.4.2 He-Trapped CaF Collisions

When trapped CaF collides with ^{3}He, three collisional processes can occur in this system: elastic collision, spin depolarization, and rotational state changing. The collisional properties of CaF with ^{3}He at 2 K were studied by Maussang *et al.* [76]. A combined spin depolarization rate of $\Gamma_Z = \Gamma_Z(N=0) + \Gamma_Z(N=1) exp(-\Delta E_{rot}/k_B T_{tr}) = (7.7 + 5.4/-2.5) \times 10^{-15}$ cm^3/s was reported. Here, $N = 0$ and $N = 1$ are assumed to be in thermal equilibrium, $\Gamma_Z(N)$ is the spin-depolarization rate of the rotational state N, $\Delta E_{rot} = 0.987$ K is the energy splitting between the $N = 0$ and $N = 1$ state, and $T_{tr} = 2$ K is the translational temperature of CaF. In addition, it was argued that the spin depolarization of $N = 1$ is much more efficient than $N = 0$. Therefore, a lower bound of $\Gamma_Z(N = 1)$ can be determined, yielding the ratio of elastic to inelastic cross section of $\gamma_{\mathrm{col,N=1}} > 8000$. We can use these previous findings in combination with Monte-Carlo trajectory simulations to estimate the He density in our experiment (when the molecules are trapped). The details about how to perform the trajectory simulations will be presented in Ch. 5.

A simulated CaF ($N = 1$) lifetime of 520 ms is obtained for $n_{\mathrm{He}} = 5 \times 10^{10}$ cm^{-3} by using the value of $\gamma_{\mathrm{col,N=1}} = 10^4$. To distinguish the relative contribution of elastic collisions and spin-depolarization, we can assume $\gamma_{\mathrm{col,N=1}} = 100$ in the simulation. Under this hypothetical situation where the possibility of spin-flip is increased by two order of magnitudes, a much shorter trap lifetime is expected, if the spin-depolarization is the dominant loss mechanism. A marginally reduced (by 20%) simulated lifetime is obtained for $\gamma_{\mathrm{col,N=1}} = 100$, indicating that elastic collisions limit the observed trap lifetime in our system.

3.5 Magnetic trapping of CaF ($N = 0$)

Despite a low capture velocity of $25 - 29$ m/s for CaF ($N = 0$) (compared to $N = 1$), we are able to load molecules in this internal state because we have produced slow molecules moving within this exceptionally low velocity range. Fig. 3.17(a) shows the CaF ($N = 0$) spectrum using $(B_1, B_2) = (2.17, 1)$ T, corresponding to a trap depth of $E_D = 786$ mK. The three spectral peaks arise from the fine structure splitting of the $B^2\Sigma^+(N' = 1)$ electronic excited state. Fig.3.18 plots the Zeeman levels involved for detecting the CaF ($N = 0$) molecules. The only allowed transition at zero field is between the two states plotted in pink [71] and the other two levels plotted in blue would be accessible in the presence of field. We also observe these three lines when measuring the CaF ($N = 0$) transverse beam spectrum in the presence of magnetic

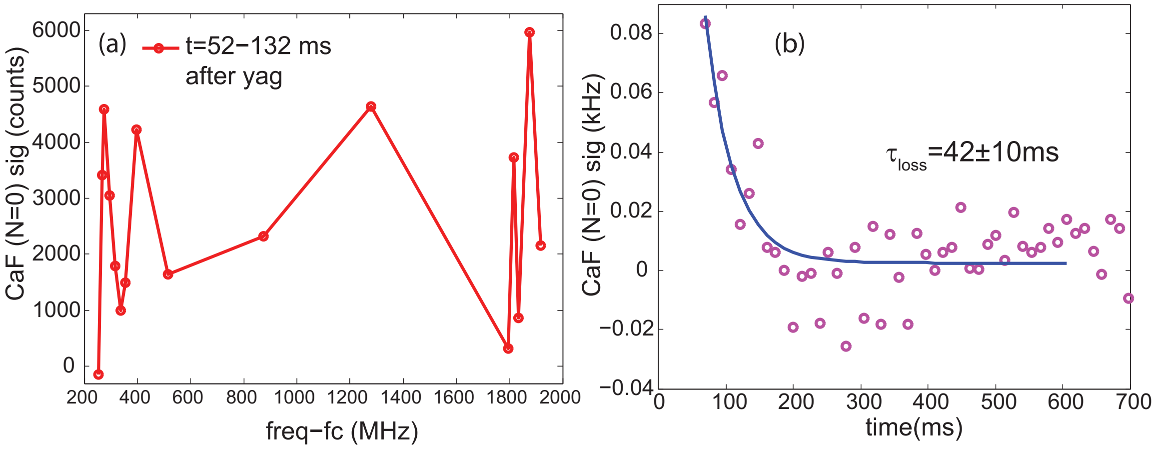

Figure 3.17: (a) Spectrum of the loaded CaF ($N = 0$). f_c is the $R_1(1/2)$ line of the $X - B$ transition measured at zero field (see Fig. 2.17). Experimental parameters: (B_1, B_2)=(2.17,1) T; 1st OPL is on between $0 - 17$ ms; 2nd OPL on between $9 - 17$ ms; 1 sccm flow, no shutter incorporated; 1 Hz YAG repetition rate. (b) Average CaF ($N = 0$) signal over the spectrum. A single exponential fit gives a decay time constant of 42 ms.

field.

We plot the average time decay signal over the spectrum in Fig. 3.17(b), giving a decay time constant of 42 ms with a buffer-gas flow of 1 sccm. The obtained decay time for $N = 0$ is a factor of 2 shorter than $N = 1$ under a similar experimental condition. Since the trap depth is comparable for both states, we suspect that the shorter decay time of $N = 0$ may arise from a more effective optical pumping of the probe laser.

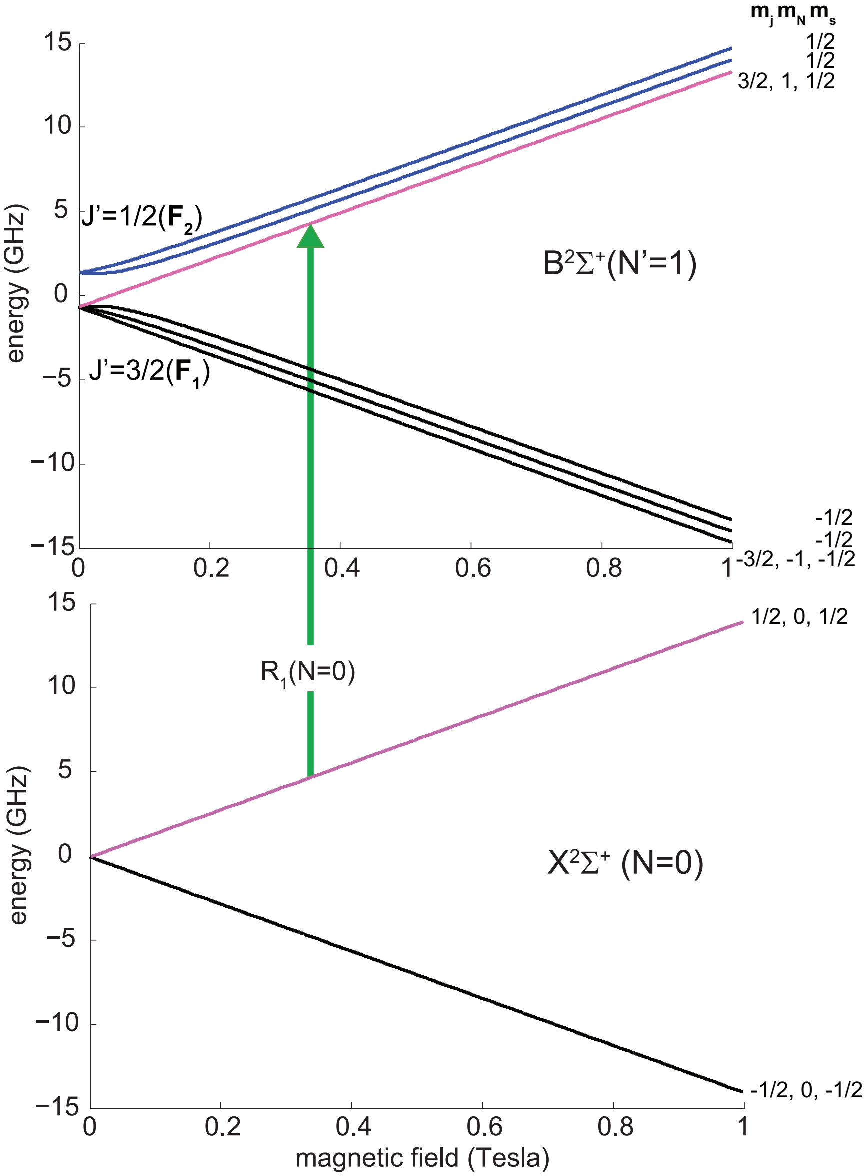

Figure 3.18: Calculated CaF Zeeman levels for the $R_1(1/2)$ line of the $X - B$ transition. Here, we only consider $H = \gamma_v \vec{N} \cdot \vec{S} - \vec{\mu}_S \cdot \vec{B}$. For $B^2\Sigma^+$, $\gamma_{v'=0}$=-0.04581 cm^{-1} = -1.37 GHz [61].

3.6 Magnetic trapping of CaH ($N = 0$)

One way to increase the capture velocity is to use a molecule with a larger rotational constant. CaH ($X^2\Sigma^+$) has a large rotational constant of 6.09 K [69],

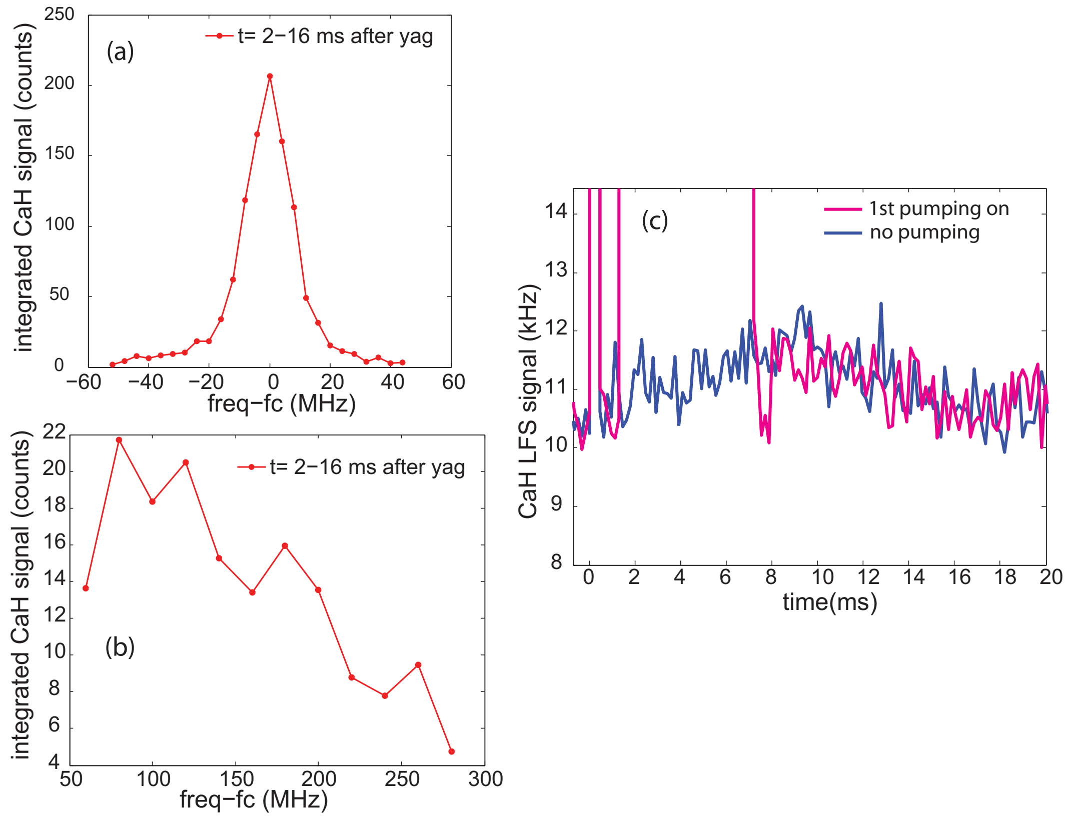

Figure 3.19: (a) and (b) plot the CaH (LFS) beam spectrum at zero field and 3.5 T. (c) LFS signals with and without the 1st OPL turning on. Trap is at 3.5 T.

meaning there is no avoided crossing up to 27 T for CaH ($N = 0$)! For both optical pumping lasers, we use the $Q_1(1/2)$ line of the $X^2\Sigma^+ \rightarrow A^2\Pi_{1/2}$ transition at 14393.36 cm^{-1} [77], since the electronic excited state also has a large rotational splitting. For the detection laser, we use the $R_1(1/2)$ line of the $X^2\Sigma^+ \rightarrow B^2\Sigma^+$ transition at 15761.96 cm^{-1} [69].

Before looking for the trapped CaH signal, we start by performing beam spectroscopy to identify the resonant frequency of the detection laser and the 1st OPL frequency to deplete the LFS. Fig. 3.19(a) and (b) plot the LFS of CaH ($N = 0$) beam spectra measured at the trap midplane at zero field and 3.5 T, respectively. We identify the resonant frequency of the 1st OPL by scanning the 1st OPL frequency to find out when the maximum depletion of the LFS occurs. Fig. 3.19(c) depicts the LFS signal at 3.5 T with and without the 1st OPL turning on. The resonant frequency of the 1st OPL is close to our prediction, which assumes the LFS in the $X^2\Sigma^+$ state have a linear energy shift with the magnetic field and the $A^2\Pi_{1/2}$ state has no Zeeman shift.

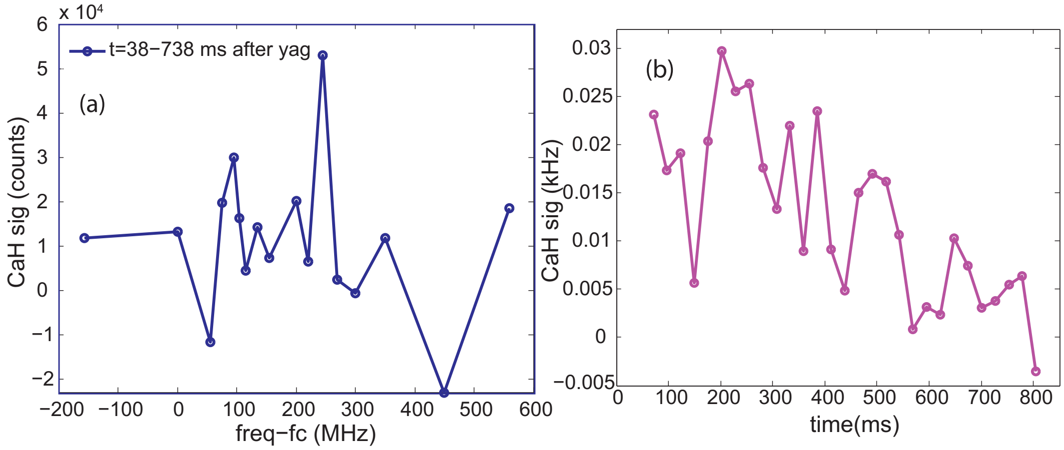

Figure 3.20: (a) Spectrum of loaded CaH ($N = 0$) using $(B_1, B_2) = (3.5, 1.5)$ T. Experiment parameters: 0.75 sccm without shutter; YAG (5mJ) at 1 Hz; 1st OPL (polarization parallel to the magnetic field) on between $0 - 17$ ms. 2nd OPL is σ_+ polarized. (b) Average time decay signal of CaH over the spectrum.

Fig. 3.20(a) shows the spectrum of loaded CaH ($N = 0$) with $(B_1, B_2) = (3.5, 1.5)$ T, corresponding to a capture velocity of $v_c = 38.6 - 45$ m/s and a trap depth of $E_D = 1.34$ K. The average time decay signal over the spectrum is plotted in Fig. 3.20(b). Although the signal is smaller than the trapped CaF, it is above the background over an extended amount of time, indicating trapping of CaH. We note that the trapped CaH signal has not been optimized.

Chapter 4

Apparatus

The experimental hardware will be introduced and described in this chapter. First, we will show how to assemble a two-stage cell step by step in Sec. 4.1. In Sec. 4.2, we will present the properties of the magnetic lens and tests we perform on the assembled lens. In Sec. 4.3, we will illustrate the magnet support structure and how we operate the superconducting magnetic trap in a truly cryogen free environment. Bringing a high current of 140 A into the superconducting magnet at 4 K turns out to be quite technically challenging. In Sec. 4.4, we will go through how we solve the "current lead problem". The design concepts of the cryogenic shutter will be explained in Sec. 4.5. Finally, we will briefly talk about the laser system, optics used for the optical pumping, and the PMT in Sec. 4.6 and Sec. 4.7.

4.1 Two-stage cell

The starting point for the molecules in our experiment is a two-stage buffer gas cell. In earlier development work on the beam source, the cell was cooled to 4 K by a pulsed tube cooler. Here, to produce cold, slow CaH and CaF beams, we cooled the cell to $1.3 - 1.8$ K by using a helium pumped reservoir (1 K pot). The cell is constructed out of oxygen free copper (C101) and is thermally linked to the 1 K pot via flexible thermal links (See Ref. [63] for the manufacture of the flexible thermal links). The construction of a two-stage cell is as follows, as illustrated in Fig. 4.1.

(a): We start by the body of the 1st cell with an inner diameter of 1″ and a length of 1.5″. Note: the tapped holes for mounting thermal links, windows, and snorkel are not shown. Four #10-32 stainless steel threaded rods are attached to the corners of the 1st cell, allowing attaching the remaining components of the two-stage cell to the 1st cell.

(b): We add the 1st cell aperture. In our experiment, it is a 1/16″ thick copper plate with a 5 mm hole for the CaF beam and 7 mm by 7 mm square aperture for the CaH beam. The thickness of the plate near the aperture is reduced to 1/32″.

(c): We add four spacers in order to leak out the He buffer gas. In the real experiment, we use a stack of brass washers as one spacer so that we can easily change the size of the gap. Three #10 brass washers give a total thickness of 2.8 mm.

(d): We attach the 2nd cell, which has an internal dimensions of 1″ diameter and $\frac{3}{8}''$ length.

(e): We add the 2nd aperture, which is a 1/16″ thick copper plate with a 9 mm diameter hole.

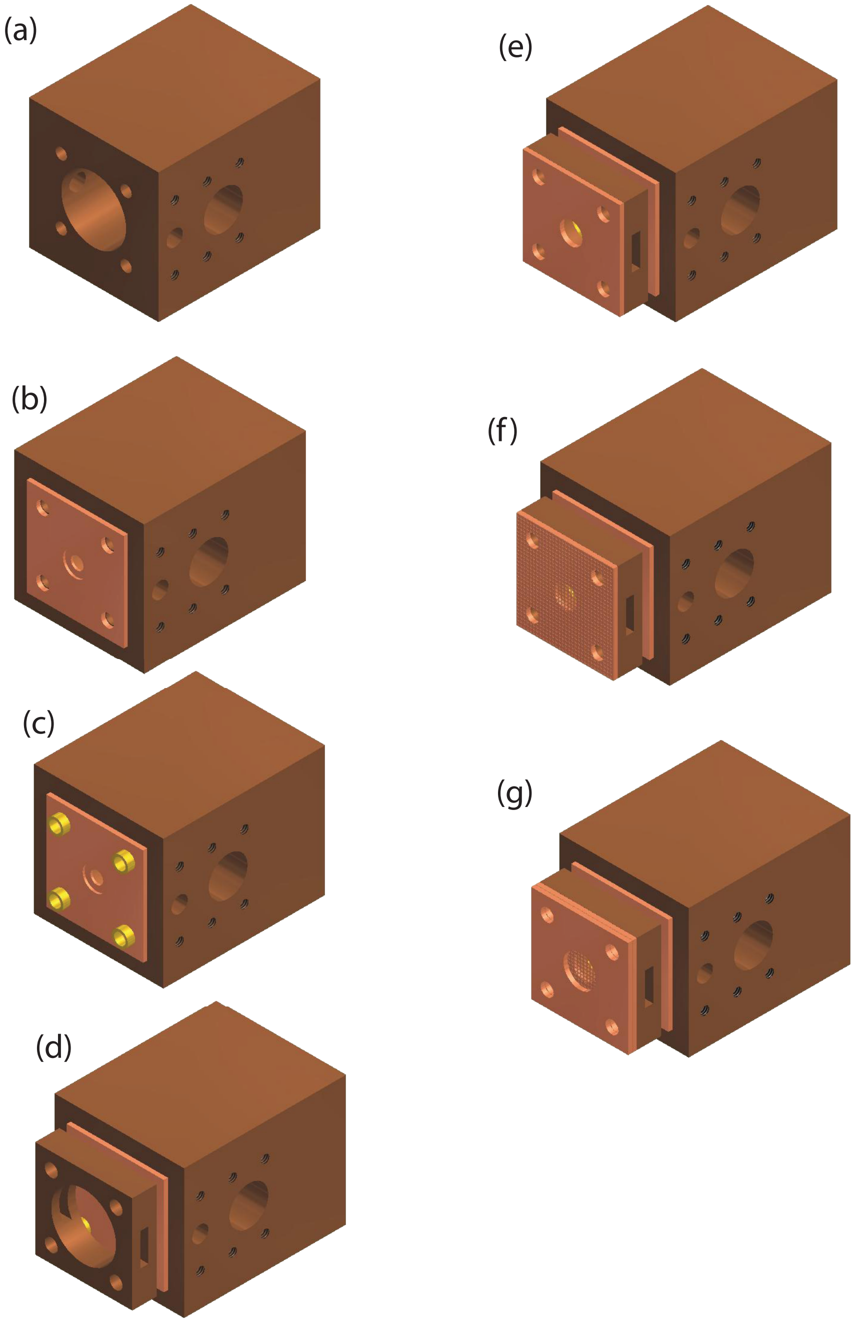

Figure 4.1: Procedure to assemble a two-stage cell. (a) Starting with the body of the 1st cell. (b) Adding the 1st aperture. (c) Adding the spacers. (d) Adding the body of the 2nd cell. (e) Adding the 2nd aperture. (f) Adding a mesh. (g) Adding a clamp piece.

(f): We attach a piece of copper mesh.

(g): Finally, we use a 1/16″ thick copper plate with a 0.5″ diameter hole to clamp down the assembly.

The assembly allows us to change parameters of the two-stage cell easily, such as the size of the apertures, geometry of mesh, and the gap distances. We experimentally determine an optimal configuration of the two-stage cell by measuring the beam properties, which is discussed in Ch. 2.

4.2 Magnetic lens

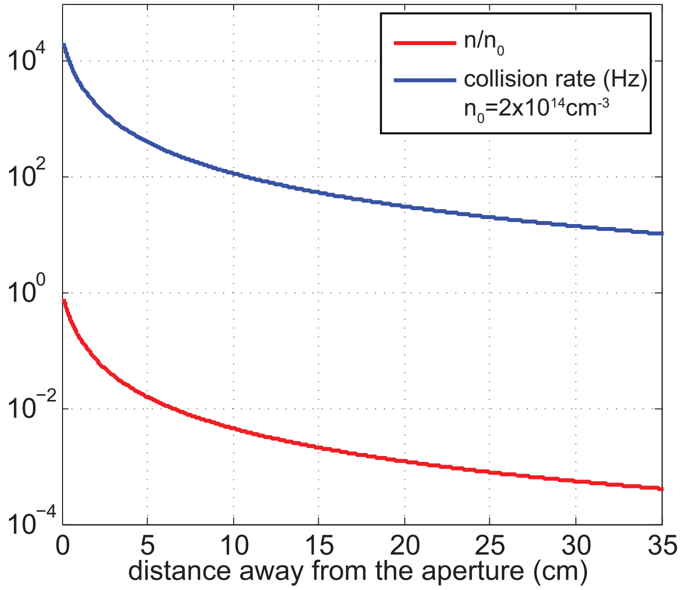

Figure 4.2: The ratio of downstream He density to upstream He density (n/n_0) and collision rate ($n\sigma_{el}v_{He}$) as a function of distance relative to the 2nd cell aperture are plotted in red and blue traces. Density right out of the aperture is assumed to be $n_0 = 2 \times 10^{14}$ cm^{-3}. We assume $\sigma_{el} = 10^{-14}$ cm^{-2} for the elastic He-molecule collision cross section. We also assume the helium beam has an effusive distribution (longitudinally) with a temperature of 4 K, and a transverse velocity spread of $\sqrt{m_{CaH}/m_{He}} \times \delta v_{t,CaH}$, where $\delta v_{t,CaH}$ is measured to be 50 m/s.

We perform trap loading at a location 30 cm downstream from the 2nd cell exit aperture. Since helium is invisible to us, we estimated the helium density profile based on the properties of the CaH beam, as shown in Fig. 4.2. The ratio of helium density at a distance of 30 cm away from the aperture, n, to the density right outside the cell exit aperture, n_0, is $n/n_0 = 5 \times 10^{-4}$. The corresponding collision rate, $n\sigma_{el}v_{He}$, is roughly 14 Hz assuming $n_0 = 2 \times 10^{14}$ cm^{-3}, $\sigma_{el} = 10^{-14}$ cm^{-2}, and v_{He} is the most probable velocity of He at 4 K. If we want to continuously load molecules into the trap, the conservative number of pulses we can load is given by the condition when the molecules would encounter one collision with the He gas. More specifically,

$$\begin{aligned} \text{number of collisions} &= \text{collision rate} \times \text{number of pulses} \times \text{pulse duration} \\ 1 &= n_{He} \times \sigma_{el} \times v_{He} \times N \times \delta t, \end{aligned} \tag{4.1}$$

where the collision rate is shown in blue in Fig. 4.2, and the pulse duration δt is roughly 10 ms of the cryogenic shutter. If we set the trap at 30 cm away from the aperture, we should be able to load ~ 10 molecular pulses.

Although the helium density drops with distance, the molecular density decreases as well. To increase the molecular flux near the trap loading region, we use a hexapole magnetic lens to collimate the low-field seeking molecules (LFS).

We assembled the lens using 12 Neodymium (N52) permanent magnets (obtained from KJ Magnetics). Six of them are magnetized along their circumference and the other six are magnetized along the radial direction. Each magnet segment has an inner radius of 0.5″, outer radius of 1″, and length of 1″. After the lens is assembled (See Fig. 4.3(b)), its field profile is measured and shown in Fig. 4.3(a). The magnetic field near the inner surface of magnetic lens is ~ 1 T. The magnetic field

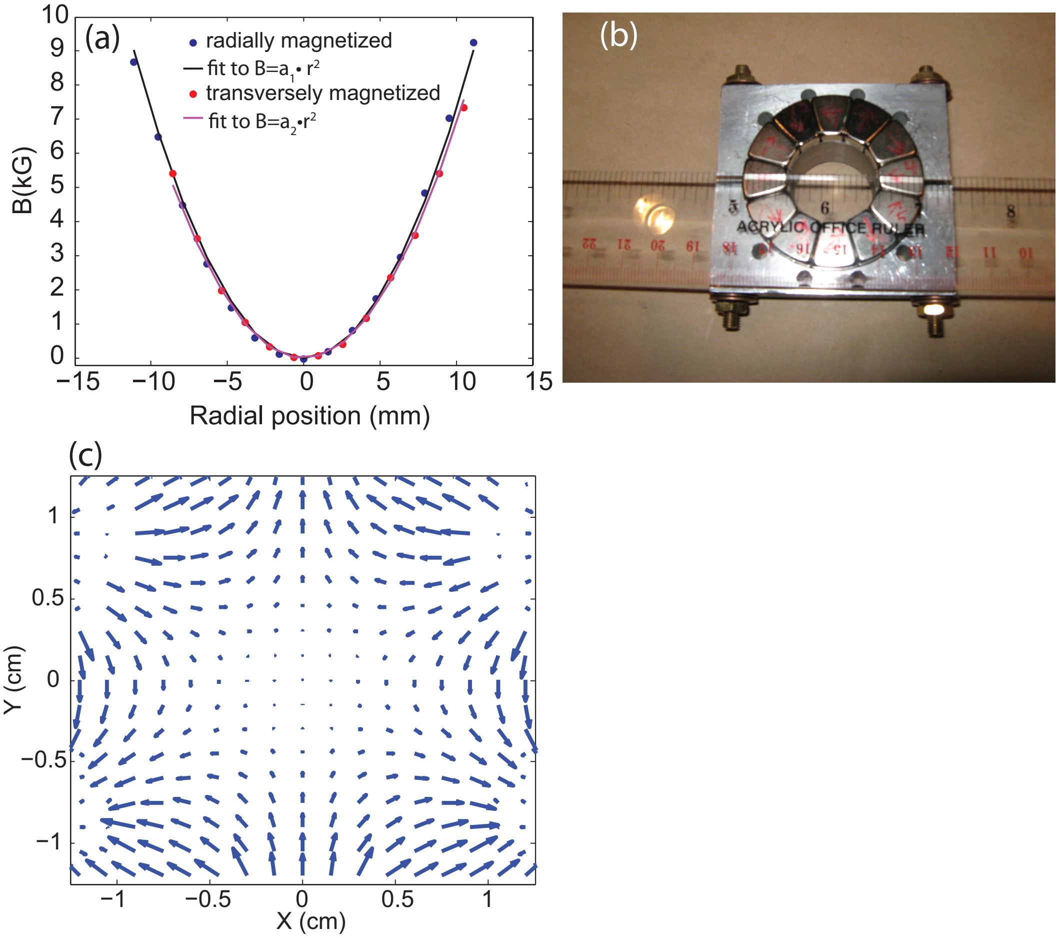

Figure 4.3: (a) Field profile of the assembled magnetic lens measured along the radially magnetized magnets (blue data) and transversely magnetized magnets (red data). (b) Photo of the assembled magnetic lens. (c) Field directions of the magnetic lens calculated using Radia.

directions along the midplane of a hexapole magnetic lens are shown in Fig. 4.3(c), which are calculated using Radia under Mathematica environment.

The potential energy experienced by magnetic species with magnetic dipole moment of μ which interact with the hexapole magnetic lens is given by [78]

$$U(r,z) = \mu \delta_r^2 B_0 r^2 S(z). \tag{4.2}$$

Here, r is the radial distance from the center line and z is the distance from the lens midplane. $\delta_r^2 B_0$ is the magnetic flux density curvature, and the envelope function $S(z) = 1/(1 + z^2/d^2)^2$ describes the spatial dependence of the potential in z with d as a fitting parameter for describing the characteristic length. As a first step to verify if the assembled lens is in hexapole configuration, we can use the functional form of $B \propto r^2$ to fit the measured magnetic field profile. Fig. 4.3(a) indicates a good agreement between the measured data and the functional form for describing a hexapole lens.

An analytical expression for the focal length of a (thin) hexapole lens can be written as [78]

$$f = (M v_{f,M}^2)/\mu \delta_r^2 B_0 L, \tag{4.3}$$

where M is the mass of the magnetic species, $v_{f,M}$ is its velocity, and L is the thickness of the lens. The above equation can be derived using the equation of motions, assuming that a particle moves on axis to the magnetic lens at a velocity $v_{f,M}$ and would gain a transverse velocity (toward the central line of the lens) due to the magnetic force. Although the magnetic force is the same for molecules moving at different velocities, fast molecules spend less time inside the lens and gain less transverse velocity, yielding a longer focal length. Since the molecular beam has finite longitudinal and transverse velocity spreads, we do not attempt to measure the focal length of the assembled lens. What we do instead is to measure whether the magnetic lens properly focuses the molecular beam.

Since the magnetic lens focuses the LFS while defocusing the high-field seekers (HFS), we should also be able to verify this experimentally by measuring the relative population of molecules in these two states. Fig. 4.4(a) shows a CaF ($N = 0$) spectrum

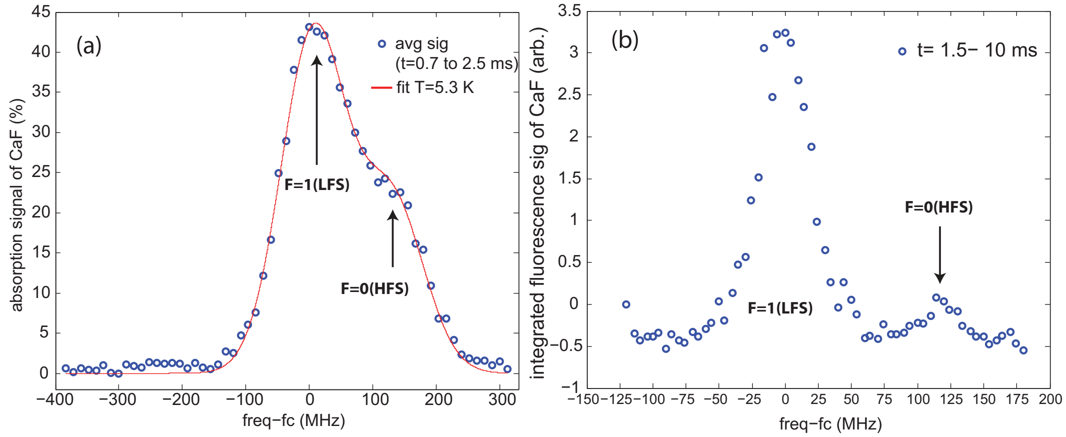

Figure 4.4: (a) CaF ($N = 0$) spectrum inside the cell using ^{4}He buffer gas (3 sccm flow) and 6 mJ YAG energy. Two hyperfine peaks are separated by 123 MHz. (b) CaF ($N = 0$) beam signal measured at 30 cm downstream. ^{4}He buffer-gas flow is 5 sccm.

measured inside the 1st cell. Two hyperfines peaks are identified and separated by 123 MHz. After the magnetic lens, CaF beam signal at 30 cm downstream is plotted in Fig. 4.4(b). The population of the HFS is suppressed relative that of the LFS, indicating the magnetic lens is working properly.

Another way to evaluate whether the magnetic lens behaves is to compare the measured CaF number downstream to the expected number based on the trajectory simulation. According to the simulation, we should have an efficiency of $\frac{N_{\text{downstream}}}{N_{\text{upstream}}} \sim 20\%$, where N_{upstream} and $N_{\text{downstream}}$ are the molecular numbers outside the cell and at 30 cm. We produce a number of 3.75×10^{11} CaF ($N = 0$) in the 1st cell (using 1.25 sccm ^{3}He and 4 mJ Yag at 2 Hz) and detect 1.5×10^8 CaF molecules at 30 cm. Assuming an extraction efficiency of 1% for the two-stage cell (See Fig. 2.20), we measure an efficiency of $\frac{N_{\text{downstream}}}{N_{\text{upstream}}} \sim 40\%$, which is consistent with the simulated efficiency and indicates no obvious beam attenuation.

Fig. 4.5 shows the two-stage cell and magnetic lens inside the intermediate chamber used for producing the slow CaF beam. 1 K pot is physically located in a different chamber (far corner in the photo). We made some modifications to the system over time. In the final trap loading experiment, we adopted a longer snorkel design (2.5″ in length and 0.375″ in diameter), allowing the buffer gas to flow in from the ablation window side. In addition, the window ports on the 77 K and 4 K shields were modified to have a width of 1.5″ on the narrow dimension. In this way, the temperature gradient on the window due to blackbody heating is reasonable for the experiment.

4.3 Magnetic trap

The magnetic trap is a superconducting quadrupole trap with a maximum trap depth of 4.9 T. The detail description of the coil geometry and construction procedures can be found in Ref. [79]; the *Mark 5* Magnet is the one we are using. This magnetic trap was also employed in the in-cell buffer-gas loading of NH and N experiments. At that time, the magnet itself was cooled by liquid helium to 4.2 K. In the current experiment, the dewar with the magnetic trap inside is cooled by a pulse tube cooler (PTC, model PT410 from Cryomech) with a cooling power of 1 W available at the 4.2 K (aka cold) stage and 35 W for the 45 K (aka warm) stage. In this section, we will focus on the magnet support structure and design of thermal links employed in this experiment.

Fig. 4.6 shows the magnet support structure from the 4 K top plate. In our system, we support the 4 K and 77 K top plates via four #10-32 Ti threaded rods to the dewar top plate at 300 K. The cold stage of the pulse tube cooler is used to

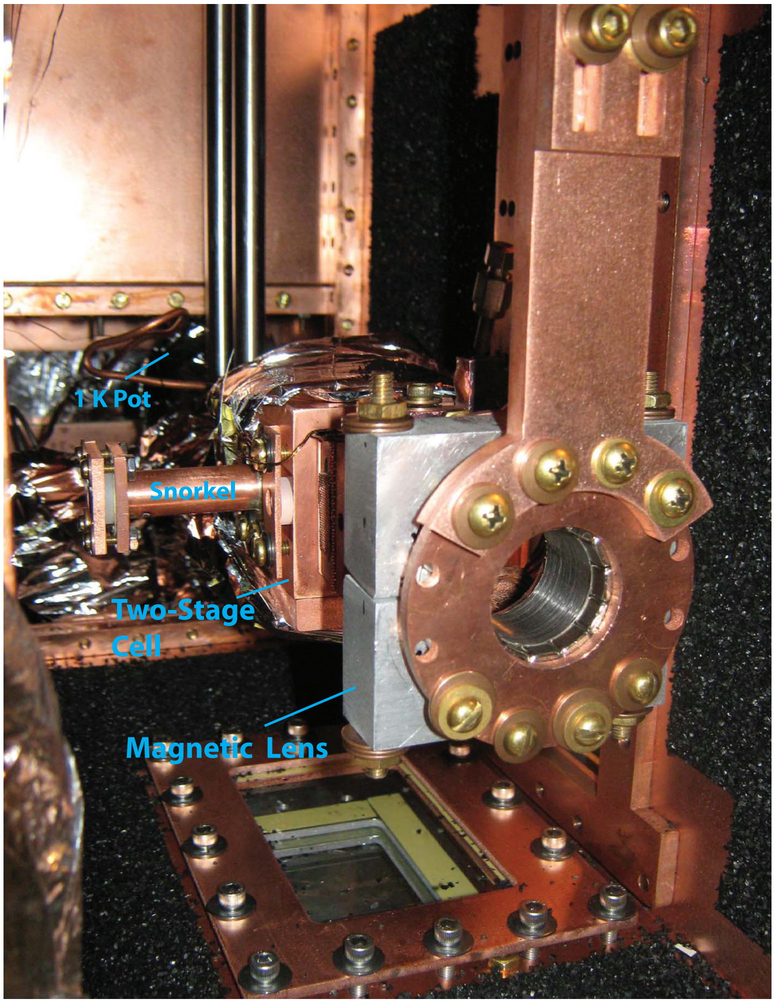

Figure 4.5: Two-stage cell and magnetic lens inside the intermediate chamber, which bridges a chamber where 1 K Pot locates and another chamber with the magnetic trap inside. Some modification were made in the trap loading experiment to improve the performance of the beam and reduce the blackbody heat load.

cool the 4 K top plate via flexible thermal links. Eight copper support plates (0.25″ thick) connect the front and back faces of the magnet (four of them are highlighted in the figure) to the magnet top plate (0.5″ thick copper plate). The magnet top plate is then rigidly bolted to the 4 K top plate. The footprint of the magnet top plate (11.4″×9.5″×0.5″) is smaller than the 4 K top plate (13.5″×13.5″×0.5″), and hence

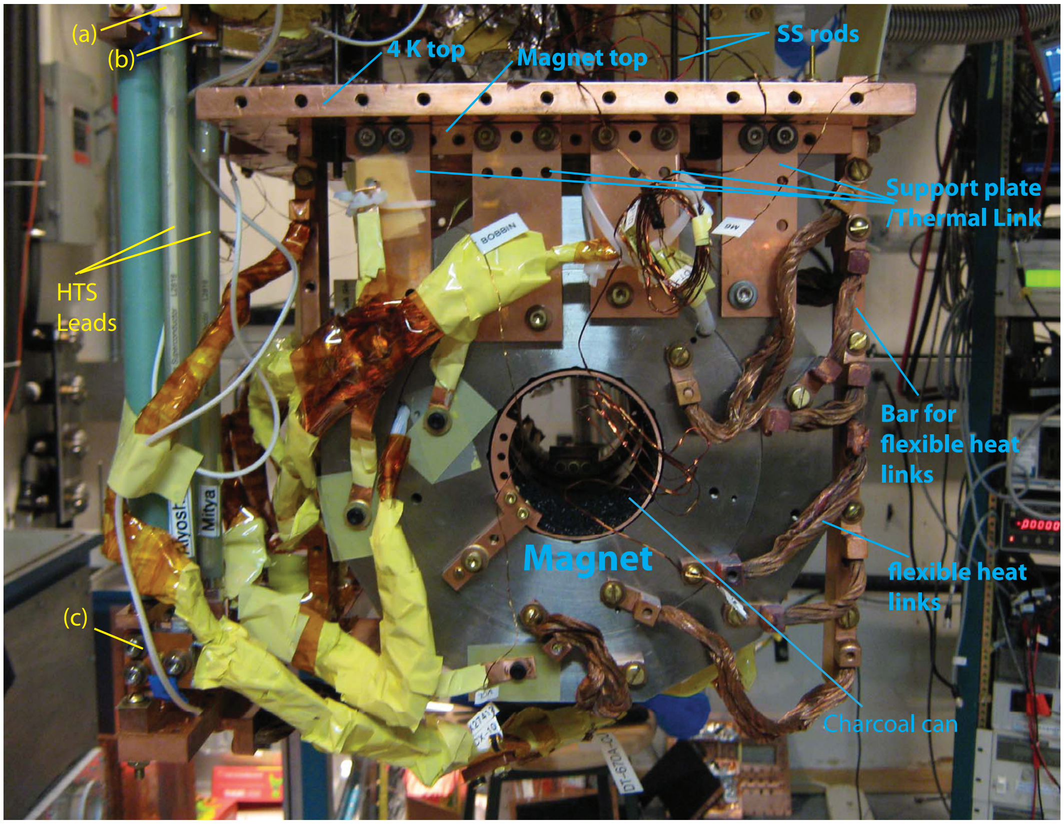

Figure 4.6: Support structure and thermal links for the magnetic trap. Note that high T_c leads (Alyosha and Mitya) are on the left of the figure and their orientations were rotated by 90 degrees in the final trapping experiment.

the magnet can be enclosed inside 4 K radiation shields.

The eight copper support plates not only provide a good thermal connection between the magnet top plate and the upper part of the magnet but release the stress on the magnet after cooling down. The length of the magnet is 11.4″, which is identical to that of the magnet top plate. Cooling down from 300 K to 4 K, the magnet top plate (copper) would shrink more than the magnet (titanium) by 0.5 mm $\equiv 2d$ along the magnet bore direction, where we assume thermal expansion coefficients of copper and titanium to be 325×10^{-5} and 151×10^{-5}, respectively. The thermal differential expansion can cause a bending stress of σ_{bending} on the copper support plate. For a copper plate with a length of $L = 3''$ and thickness of $t = 0.25''$, the bending stress is $\sigma_{\text{bending}} = Ey/R$ [80], where $E = 117$ GPa is the Youngs modulus of C101, $y = t/2$ is the maximum distance from the neutral axis of the bent plate, and $R \sim L^2/(2d)$, yielding a bending stress of ~ 32 MPa. This is less than half of the yield strength of copper and thus the copper support plates bend elastically after cooling down.

The magnet cask and bobbin consist of Grade 6 Titanium (containing 5% aluminium and 2.5 % tin). Although the low temperature thermal conductivity of Grade 6 Titanium is not available, we should treat the magnet itself as a poor thermal conductor, same as grade 5 Titanium (containing 6% aluminium and 4% vanadium) which has a thermal conductivity two order of magnitudes lower than C101 at 20 K [81]. For this reason, we connect additional flexible heat links to the lower part of the magnet (we highlight this in Fig. 4.6).

Each flexible heat link consists of two C101 braids and each C101 braid has a cross section area of 0.0967 cm^2. The end of the C101 braid is welded to a C101 log for mounting. We assume the thermal conductivity of the flexible thermal link to be $\kappa = 2$ W/(cm·K), which is based on a measurement in the trap loading of NH experiment in the past. This thermal conductivity is close to that of copper with RRR $= 40$. Assuming a heat load of 100 mW on the magnet (roughly the head load from a blackbody at 300 K with an area of 2 cm^2), we need roughly 13 flexible thermal links with a length of $3''$.

During the first cooldown of the magnet, its base temperature of 4.7 K was 0.2 K higher than the old NH experiment, reducing the trap depth we can operate. We tried to improve this by cutting down blackbody heat loads, including blocking the direct blackbody radiation from 300 K, applying more superinsulation on the 4 K radiation shields, and reducing the size of the window ports to 1.5″. We use BK7 windows with thicknesses of 0.25″ or 0.375″ on the 4 K shields. For 77 K shields, the BK7 windows have a thickness of 0.375″ or 0.5″.

In addition, we improved the thermal links between the 4 K top plate and pulse tube cooler by adding more flexible links. Several flexible thermal links are also added between the magnet and the four copper bars. After a few test cooldowns, the magnet with a base temperature of 4 K was achieved, allowing us to operate the trap at its full strength of 4.9 T.

The coil geometry of the magnetic trap and the field profiles along the radial and magnetic bore directions are shown in Fig. 4.7.

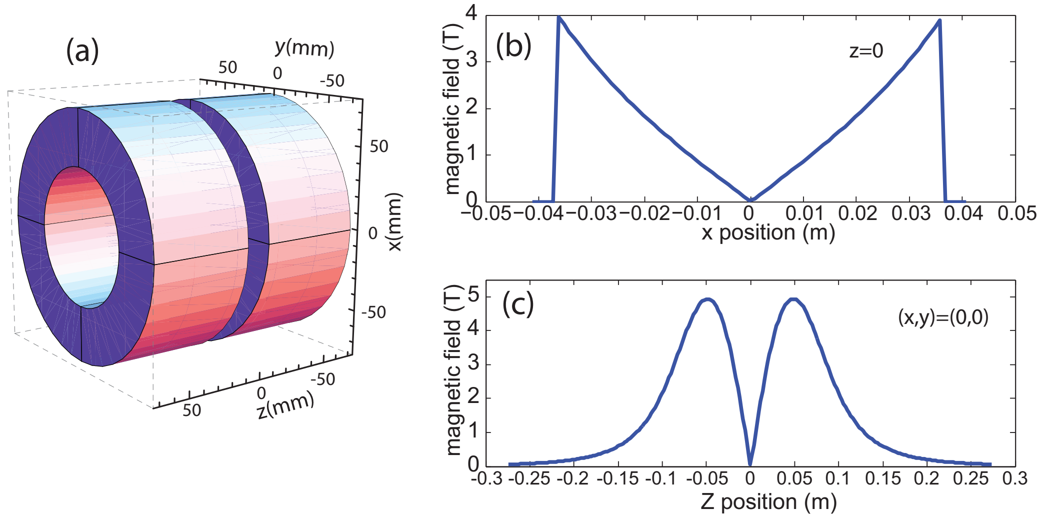

Figure 4.7: (a) Coil geometry of the magnetic trap. (b) Magnetic field along the radial direction at the trap midplane. Current of the trap is 140 A. (c) Magnetic field along the z axis at 140 A.

4.4 Current leads

The current leads consist of three parts as shown in Fig. 4.8: brass resistive leads carrying the current from 300 K to 77 K, high T_c superconducting (HTS) leads bringing the current from 77 K to 4 K, and low T_c superconducting (LTS) leads finally delivering the current to the magnet bobbin. In this section, we will discuss how we chose the material of the resistive leads. In addition, two unusual magnet quenches occurred in the earlier two cooldowns, which were associated with an improper design of the connection of the HTS to the LTS. We will describe how we resolve the problems next.

In the old NH experiment, the resistive lead was made out of copper. It has a low electric resistivity and hence low resistive heat load when the magnet is energizing to 140 A. However, the good thermal conductivity of copper also causes a large conductive load on the HTS side. The solution at that time was to add thermal links between the liquid nitrogen bath and the midpoint of the copper leads. In this fashion, most of the the conductive load was transferred to the liquid nitrogen bath and the HTS top could be cooled below the superconducting critical point using the warm stage of the PTC.

In the current experiment, we only use one pulse tube cooler to cool the entire system. Obviously, we needed a different material for the resistive leads. Brass has a lower thermal conductivity than cooper roughly by a factor of 4 at room temperature, and a factor of 3.5 larger resistivity than copper. Choosing the dimension of the brass leads carefully, we are able to make the combined conductive and resistive heat loads to be less than the cooling power of the warm stage of the PT410.

The three brass leads we chose each to have a diameter of $0.25''$ and a length of 19 cm (Fig. 4.8). There is a combined conductive heat load from room temperature via the three brass leads, followed by three short copper sections, to the top of the high T_c leads. The total conductive heat load on the warm stage is calculated to be 5.8 W. The temperature of the copper plate on the top of the HTS was measured to be $T_1 = 53$ K (Fig. 4.8), which was cooled by the warm stage of the PTC at a base temperature of 37 K.

When the magnet is operating in the anti-Helmholtz configuration (forming a magnetic trap), two of the brass leads carry current from room temperature to the high T_c leads via two flexible copper links, named Alyosha and Mitya. The resistance of one brass lead and one flexible copper line is measured to be 0.368 mΩ. At a current of 140 A, the resistive heat load from two leads is hence 14.4 W. We observe that the temperature of the copper plate on the top of the HTS reaches $T_1 = 75$ K, for a combined conductive and resistive heat loads of 20 W (trap at 140 A).

The temperature of the copper plate on the top of the HTS was under the superconducting critical temperature when the magnet is at its full current. However, we encountered two abnormal magnet quenches. This magnet (*Mark 5*) typically quenches three to four times around $55 - 62$ A when it is cooled down from room temperature to 4 K. For each subsequent quench, the magnet current can be raised by 1-2 A and finally can be ramped up to its full current. We call this process as magnet training. In the old NH experiment, the magnet can be operated at its full current (140 A) without any problem after it is trained. The first abnormal quench we encountered (beyond that just described) occurred 30 minutes after the magnet

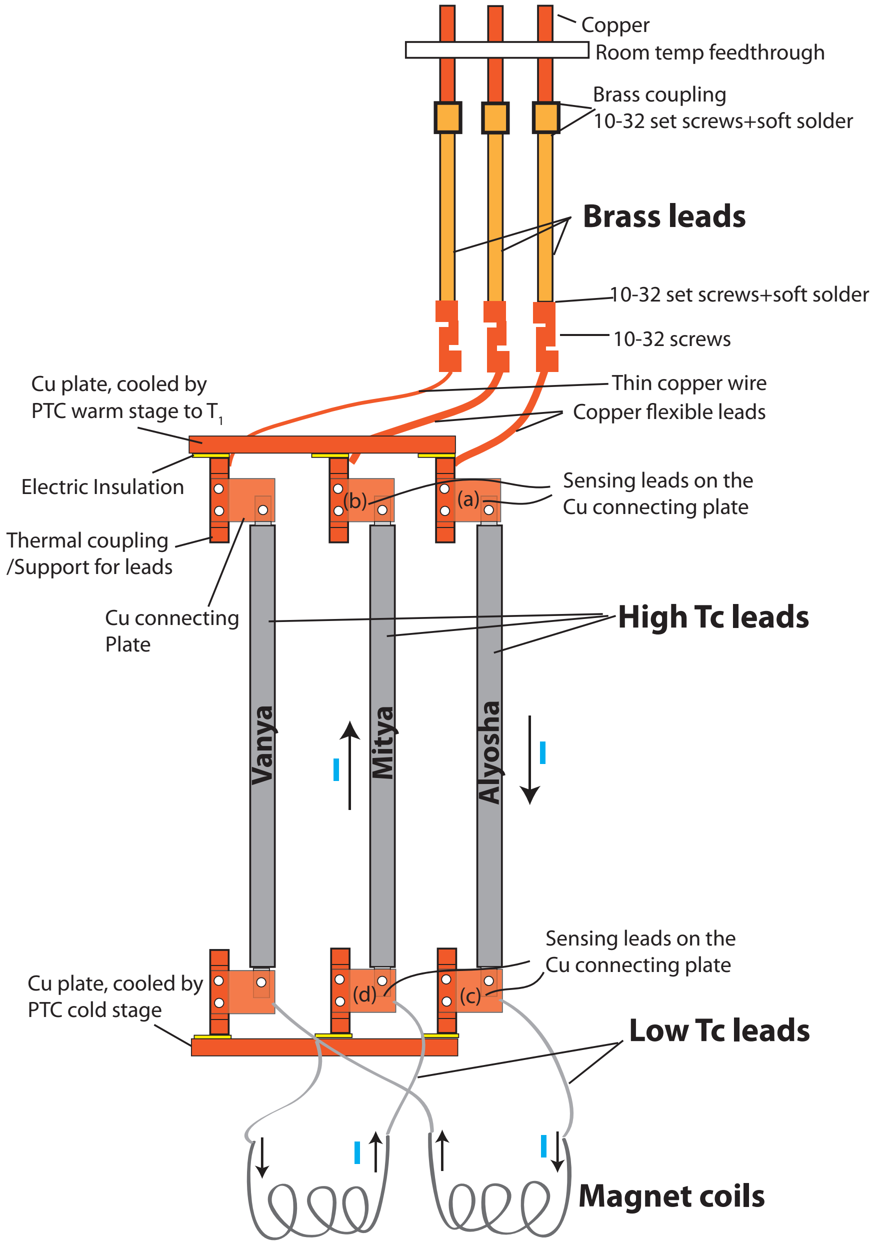

Figure 4.8: Schematic of the current leads (not to scale). Only two of the leads (Alyosha and Mitya) are active and carrying currents when the magnet is in the anti-Helmholtz configuration. Note that the orientation of the leads in the real experiment are different from this schematic. Brass leads have a diameter of 0.25″ and length of 19 cm. We use two 10 cm long flexible copper heat links (each has a cross section area of 0.19 cm^2) to connect the brass leads and the two active high T_c leads. The third high T_c lead (Vanya), connecting to the brass lead via a copper wire with a diameter of 0.02″ and length of ~10 cm, can carry current only when the magnet is in the Helmholtz configuration. Mitya is physically closer to the magnet center than Alyosha, as shown in Fig. 4.6.

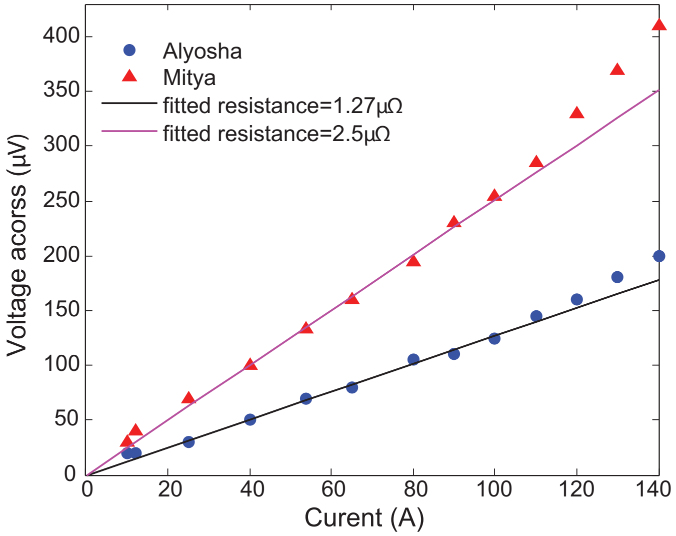

Figure 4.9: Voltage across HTS leads versus current before the 1st abnormal magnet quench. The voltage sensing points are shown in Fig. 4.8: voltage difference between point (a) and point (c) is for Alyosha; (b) and (d) for Mitya.

had reached its full current. We noticed that the voltages across the HTS leads, measured between point (a) and (c) for Alyosha and point (b) and (d) for Mitya in Fig. 4.8, behave nonlinearly at high currents, as shown in Fig. 4.9. The sensing leads are placed on the copper connecting plates, and the end cap of the HTS lead is sandwiched by two connecting plates. Therefore, the measured voltage difference has two contributions: one is from the resistance of the HTS lead and the other is the contact resistance between the connecting plate and the end cap of the HTS lead. However, the nonlinear voltage dependence indicates a significant resistance change, implying that the HTS went into its normal phase when we energized the magnet. We also note that the temperature of the copper plate on top of the HTS, T_1, was gradually increasing after ramping up the magnet to its full current. This is likely because the warm stage of the PTC not only cools the HTS top but also the 77 K radiation shields. A large thermal mass can cause a long thermal time constant.

We attribute two possible reasons for the HTS leads turning normal. Although the temperature of the copper plate on the top of the HTS, T_1, is below the critical temperature, we suspect the actual temperature of the leads may be higher. We used a piece G-10 with a thickness of 5 mil to electrically insulate the copper plate above the HTS. The thermal properties of the G-10 insulator are then tested at 77 K in a separate test rig. We found a temperature gradient of 23 K developed across the G-10 with a heat load of 20 W, which would certainly make the temperature of HTS leads themselves above their critical temperature.

In addition, the HTS leads are located much closer to the magnetic trap, compared to the old NH experiment, due to the spatial constraints. We define the coordinate system according to Fig. 4.7, where the center of the magnet is at (0,0,0). Mitya is located at (y, z)=$(18, 11)$ cm and Alyosha is located at (y, z)=$(18, 16)$ cm. The magnetic fields produced by the magnet at 140 A along y axis (or defined as parallel field for the HTS lead in Fig. 4.10(a)) and z axis (or defined as perpendicular field for the HTS lead in Fig. 4.10(a)) on the two leads are depicted in Fig. 4.10(d), (e). Parallel fields drop rapidly compared to the perpendicular field. In addition, near the top of the HFS lead ($x = 20$ cm), a perpendicular field of 0.015 T is a factor of three larger than the parallel field for Mitya, which is closer to the trap center. The manufacture of the high HTS leads (HTS-110) provided data on the current scaling factor versus magnetic field strength, as shown in Fig. 4.10(b) and (c). Our HTS leads are rated to 250 A at 65 K. The full current of 140 A for the magnetic trap corresponds to operating the HTS leads at a current scaling factor of 0.56. According

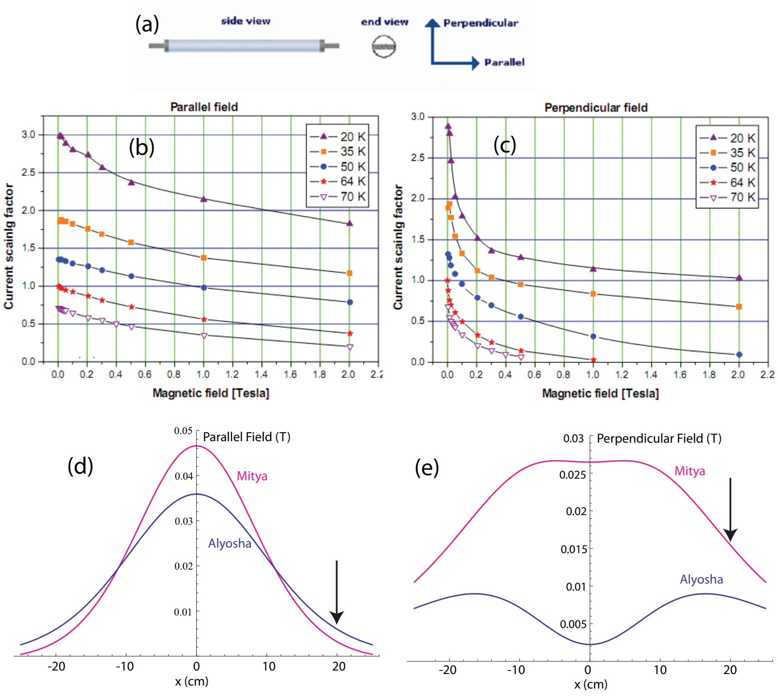

Figure 4.10: (a) Perpendicular and parallel field directions defined and provided by the manufacture (HTS-110 from New Zealand). Current scaling factor versus magnetic field at different temperatures for parallel field (b) and perpendicular field (c). The HTS leads we used are made out of BSSCO (Model number: CS025030, operating current is 250 A at 64 K). Parallel and perpendicular fields along the direction of gravity (or x axis in Fig. 4.7) calculated for Alyosha and Mitya. Here, $x = 0$ is the center of the magnet. The top of the HTS lead locates at $x \sim 20$ cm, which has the highest temperature.

to the specifications, the scaling factor is extremely sensitive to the perpendicular field. More specifically, we can tolerate at most a parallel field of 0.4 T and probably a perpendicular field of only ~ 0.01 T at 70 K. Therefore, we surmised that we would avoid anomalous quenching by rotating the leads by 90 degrees.

We made three changes after the first abnormal magnet quench. First, we used thermally conductive kapton from Dupont (Kapton-MT) with a thickness of 3 mil as

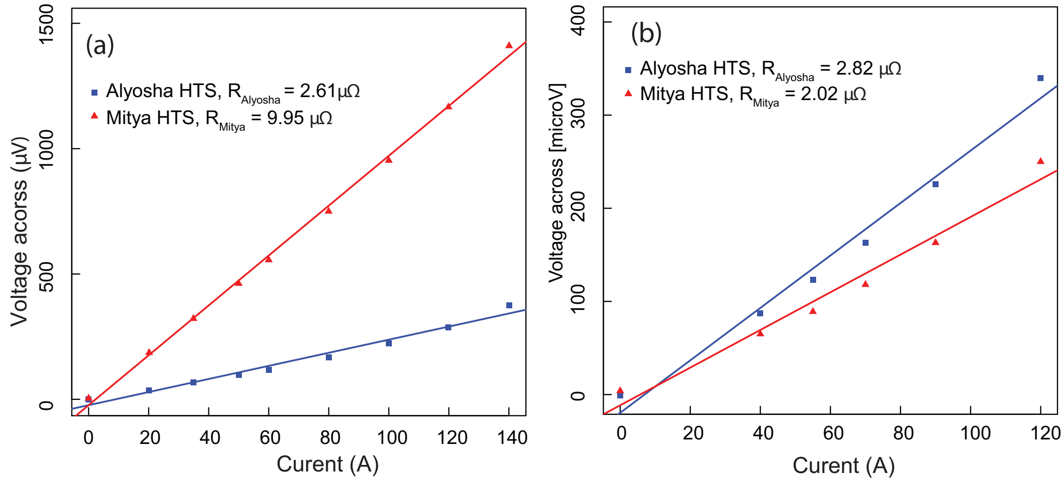

Figure 4.11: We made three improvements to the HTS assembly after the 1st abnormal magnet quench. Voltage across HTS leads versus current after these improvements is shown in (a). After polishing the end caps of Mitya, the voltage versus current measured is shown in (b).

the insulator (compared to 5 mils of G-10 used previously). Its thermal properties were tested at 77 K. With a 20 W heat load, we found a temperature difference of 3 K across the piece of kapton (with thermal grease (Apiezon N) applied at the junction). In addition, the supporting structure of the HTS leads was modified to rotate the orientations of the leads by 90 degree. Finally, we used indium foils between the electric junctions in order to reduce the contact resistance. The last change was motivated a measurement where we found the contact resistance between two copper surfaces can be reduced by 30% by using a piece of indium foil (5 mil). The voltage across the HTS leads after these improvements is shown in Fig. 4.11(a). We can ramp up the magnet up to its full current and the voltages always have a linear dependence on the current, indicating a constant resistance. However, we noticed the resistance of the Mitya assembly was a factor of few larger than the Alyosha assembly. In addition, the magnet went though another abnormal quench after it was ramped up to its full current again. At this time, we noticed the temperature of the LTS leads connecting to the magnet rose above 5.1 K.

We suspect that the junctions of the Mitya assembly were not connected properly in that run. After disassembling the Mitya assembly, we discovered some indents on the (copper) end cap of the Mitya lead where washers located. There were small patches of indium foils on the end cap, which seemed to be accumulated over time during multiple assembling attempts. After carefully polishing the surface of the end cap and applying new indium foils, the voltage across the HTS leads was measured and shown in Fig. 4.11(b). The resistance of Mitya assembly dropped significantly compared to Fig. 4.11(a), and we did not encounter anomalous quenches after the improvements describes above.

4.5 Cryogenic shutter

After we successfully loaded CaF molecules into the trap, we realized that the collisions between the trapped molecules and the helium beam were the limit on the trap lifetime. A cryogenic shutter was then installed between the magnetic lens and the trap in order to block the buffer gas after trap loading. Fig. 4.12(a) depicts the drawing of the shutter assembly. The shutter blade itself is a piece of copper with a diameter of 1.75″ (Fig. 4.12(b)) and thickness of 1/16″. The shutter blade is mounted on a thin wall metal shaft, which is supported on the room temperature plate. The actuation is achieved through a commercial rotary feedthrough on the dewar.

The shutter blade directly faces the cell and the magnetic trap and blocks the cold helium when it is closed. We would like the shutter blade to remain cold so

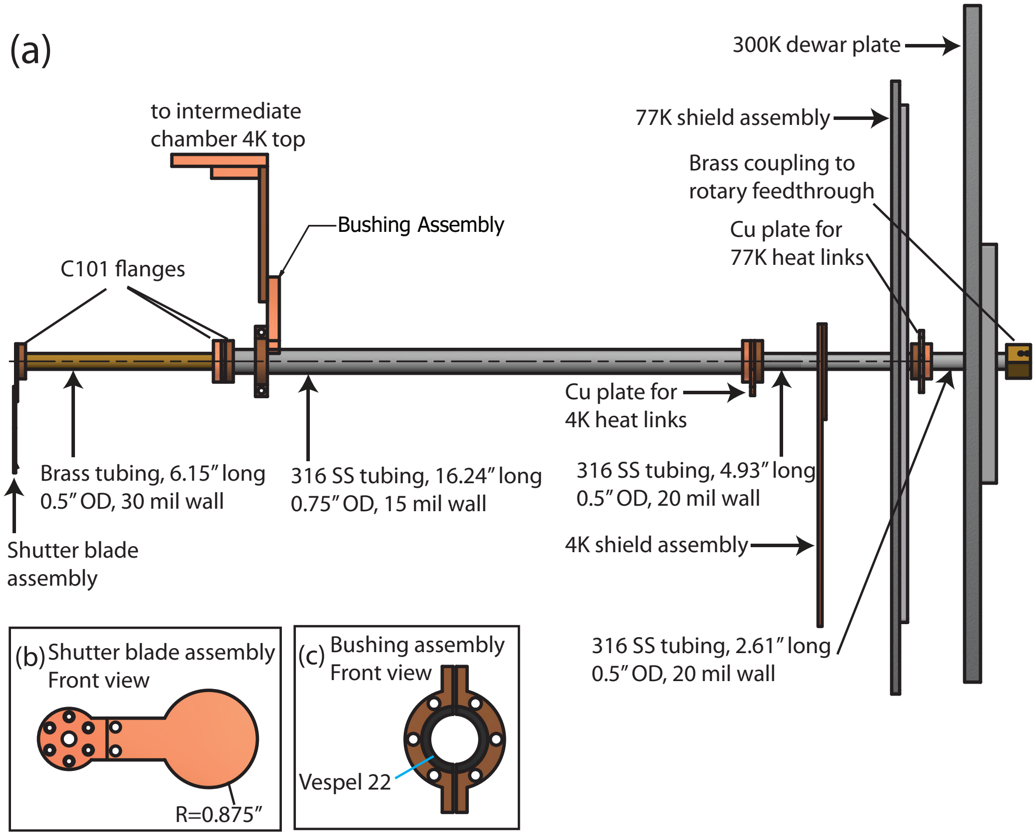

Figure 4.12: (a) Drawing of the cryogenic shutter assembly. (b) Front view of the shutter blade. (c) Front view of the bushing assembly.

that the radiative heat load from the shutter blade can be negligible and the He atoms scattering out of the blade can remain cold as well. The metal shaft consists of several segments of thin wall metal tubings (dimensions are noted in Fig. 4.12(a)). Most of the tubing material is 316 SS, which has a low thermal conductivity and is strong. Only the last segment of the shaft is made out of brass, since the magnetic field locally is on the order of 100 G when the trap is energized. All of the thin wall metal tubings are brazed to copper flanges (0.25″ in thickness) to form segments of the shaft. Flexible thermal links are connected to copper plates (1/8″ in thickness) inserted between two segments of the shaft.

A bushing assembly is installed near the end of the shaft to constrain the motion of the shutter during actuation. The bushing material is Vespel 22 (from Emco Industrial Plastics, Inc). Vespel 22 is machined into two half rings and glued into the copper rings (Fig. 4.12(c)).

The shutter can be closed up within $10 - 15$ ms across the diameter ($1''$) of the magnetic lens. Actuating at 1 Hz with a 15 ms closing duration, we observed a temperature increase on the intermediate 4 K shield of ~ 3 K (from 5 K up to 8 K). This is due to the frictional heating between the shaft and the bushing, which is thermally linked to the intermediate chamber 4 K shield. We would like to point out that the cryogenic sorbs inside the intermediate chamber did not run away despite the temperature increase. Actuating at 0.5 Hz with a closing duration of 100 ms, we only observed a temperature increase of ~ 1 K.

Fig. 4.13 shows the cryogenic shutter together with the magnetic lens and the cell inside the intermediate chamber.

4.6 Laser system and optics in the Dewar

For trap loading of CaF, two pumping lasers at 606 nm are generated by CW ring dye lasers. The output power of the dye laser is roughly $600 - 700$ mW at this wavelength, but we typically use a total pumping laser power of 50 mW for each optical pumping stage. The detection laser at 531 nm for CaF is obtained by doubling a slave diode laser at 1062 nm (seeded or frequency locked). More specifically, we start with a master ECDL at 1062 nm (Thorlabs, M9-A64-0300 with 300 mW at 390 mA current). At an operational current of 194 mA, we obtain an output power of

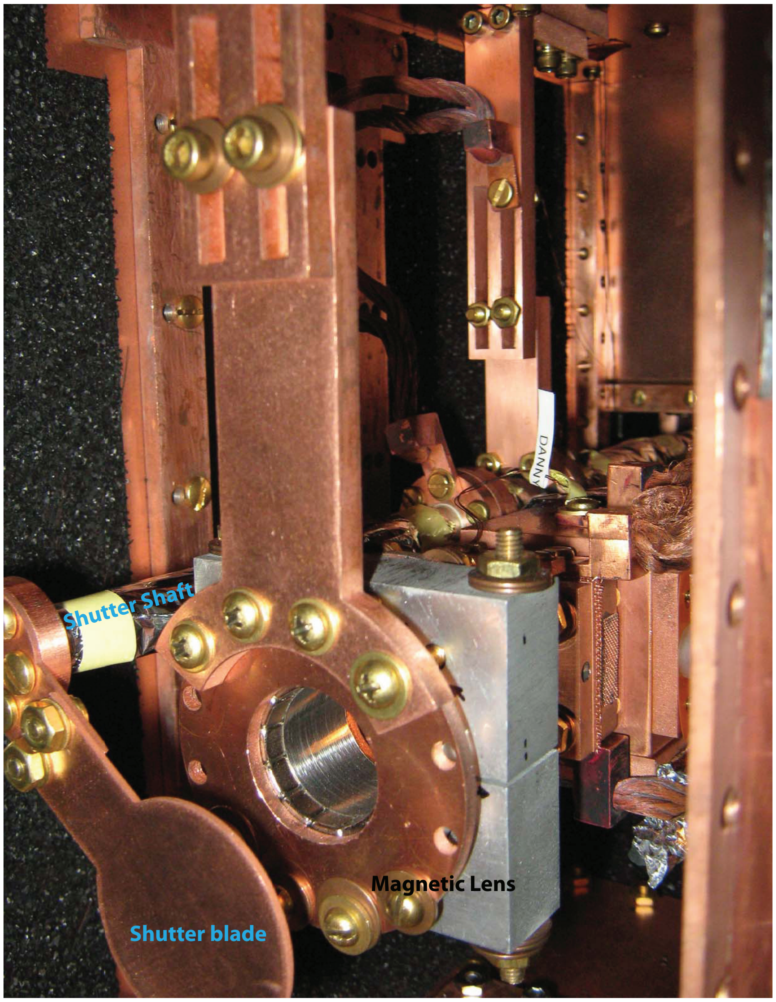

Figure 4.13: Shutter inside the intermediate chamber with the magnetic lens and cell used in the trap loading experiment.

35 mW from the master laser at the desirable frequency. The output of the master laser is used to injection lock another identical laser diode (slave laser), which has an output power of 160 mW at 382 mA. After coupling the output of the slave through a polarization maintaining fiber, we obtain a power of 70 mW immediately before a ppKTP crystal, which has a doubling efficiency of 120%/W from ADVR (PM fiber coupling on both the input and output of the crystal). We obtain a doubled laser power of 1 mW at 531 nm. (We note that the slave laser power degrades over time,

causing the detection laser power to decrease significantly. The laser diode of the slave laser should be replaced and turned off when the experiment is not running.)

For CaH, all of the pumping and detection lasers are solid state lasers. Two pumping lasers at 695 nm are also produced from a master-slave laser system. We start with a master ECDL at 695 nm using a diode (QL68J6SA) from Roithner. We obtain a 10 mW output at 50 mA from the master laser. An identical laser diode is then injection locked to the master and provides an output power of 40 mW at a current of 90 mA. The output of the slave laser then propagates in free space to the dewar. The detection laser at 634 nm is an ECDL laser using a laser diode from Thorlabs (HL63133DG). We note that most of these diodes tend to lase at 638 nm at room temperature, which means it requires a significant amount of cooling to pull the wavelength down to 634 nm. However, we found some of them do laser at a lower wavelength. The one we installed lases at 634 nm at room temperature without any optical feedback, which greatly simplifies out setup.

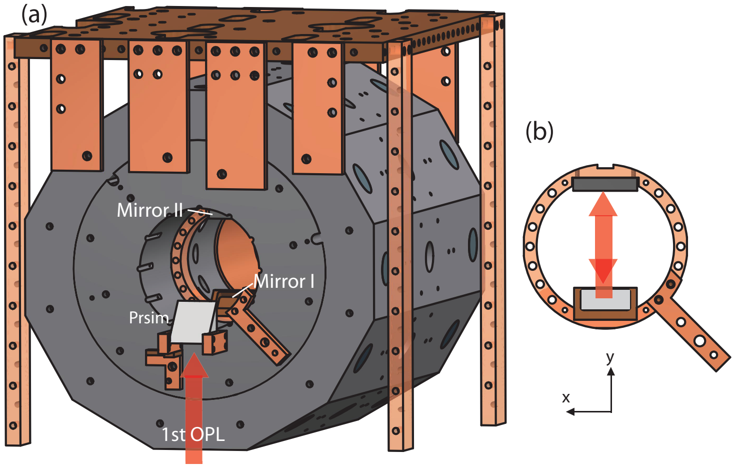

Figure 4.14: (a) 1st OPL optics inside the magnet. (b) Enlarged mirror mounting ring inside the magnet bore.

The 1st OPL spatially intersects the LFS near the saddle point so that we can avoid pumping the trapped LFS after trap loading. This requires mounting optics, including one prism (N-BK7) and two silvers mirrors, on and inside the magnet, as shown in Fig. 4.14. The 1st OPL is coming from the bottom of the dewar and directed by the prism to the mirrors inside the magnet bore. The 1st mirror, which is mounted at 45 degree relative to the z axis, reflects the 1st OPL to the 2nd flat mirror, which retro-reflects the 1st OPL out of the system. We note that the optics is mounted on copper holders and the optics assemblies are fixed on the front surface of the magnet.

The laser induced fluorescence is collected by two borosilicate fiber bundles (Fiberoptic Systems, Inc.) with an outer diameter of $0.43''$ mounted on the magnet midplane. Two fiber bundles then merge to a single bundle with an active area of $0.53''$ in diameter and a 0.66 NA. The end of this merged fiber bundle directly connects to a light pipe (fused quartz, Technical Glass Products Inc.) with a diameter of $0.75''$, which can be mounted on top of the dewar and sealed off using a NW-tube quick coupling. Placing a Delrin ball, illuminated with a laser source, inside the magnet center, we measured the light collection efficiency of the two fiber bundles followed by the light pipe to be $C.E. = 0.35\%$.

4.7 PMT

Once the fluorescence photons are collected by the light pipe, we connect the end of the light pipe directly to the front face of a PMT (R8900U-20, Hamamatsu). We measured the gain curve of this PMT, which is illustrated in Fig. 4.15(a). For detecting small signals, we found that operating the PMT in photon counting mode provides us a better sensitivity than in analog mode. For this purpose, we measure the pulse height distribution of the PMT, which is shown in Fig. 4.15(b). PMT is operated at -800 V for this test. The PMT signal is amplified by a pre-amplifier (SR 445A, SRS) and then sent to a multichannel scaler. We determined a discrimination level of -2 mV would be appropriate for cutting out the electronic noises. We also notice the dark count rate of the PMT is roughly 50 KHz at room temperature. By cooling the casing of the PMT down using a TE cooler, we can reduce the dark count to <1 KHz level, as illustrated in Fig. 4.15(c).

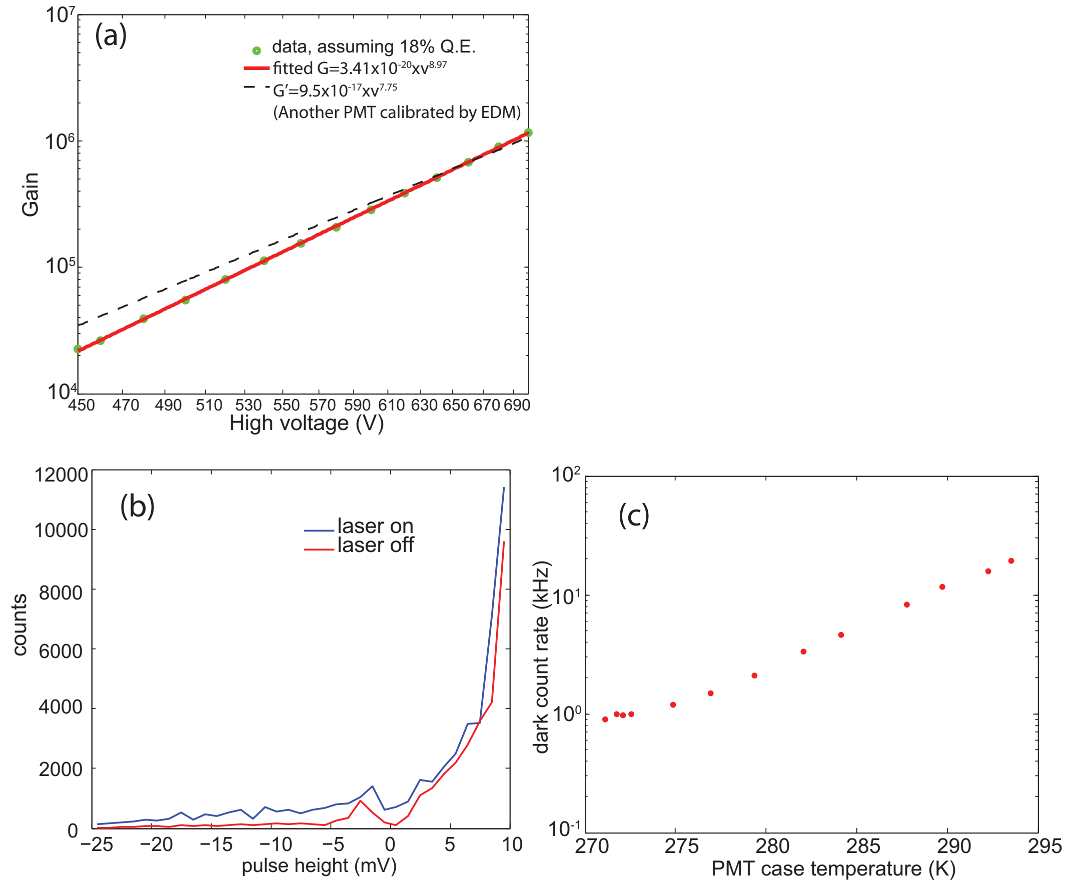

Figure 4.15: (a) Gain curve measured for the PMT (R8900U-20). (b) Pulse height distribution. (c) Dark count versus temperature of the PMT casing.

Another key to observing the a trapped CaF signal of 0.5 KHz was to reduce the scattering from the detection laser. The detection laser is sent into the dewar at an angle of incidence of 30 degree relative to the windows. We typically use a detection laser power of $12 - 15$ μW (with a beam diameter of $2 - 3$ mm) and the scattering rate from the detection laser of CaF at 531 nm is ~ 20 KHz.

Chapter 5

Trajectory simulations for optical loading and trap lifetimes

The idea of optical loading is straightforward. Theoretically, we can always accumulate some molecules in the trap, as long as a portion of the molecular beam is falls within the capture energy of the loading scheme (Eq. 3.11). In order to remove as much energy as possible, we would like to perform the 1st optical pumping near the saddle point and the 2nd pumping at the trap center. However, the HFS between two pumping stages are attracted to the magnet cask where their energy is lower. The molecular beam in the high-field seeking state is diverging in the trap and the loaded molecular number can be reduced if the 2nd pumping stage occurs at the trap center. Therefore, there should be an optimal field to perform the 2nd optical pumping. In addition, the magnetic lens we built has an effective focal length, which depends on the properties of the beam. So, there will be an optimal distance between the magnetic lens and trap.

To find the optimal conditions for performing the trap loading experiment, we set up trajectory simulations for the entire loading process. In this chapter, we will first explain the algorithm of the trap loading simulation (Sec. 5.1). The simulation results for CaH and CaF molecules will be presented in Sec. 5.2 and Sec. 5.3. Based on the simulated trajectories and data, we are able to decide the size of the molecular beam at two optical pumping stages as well as the radius of the trapped cloud, which enable us to choose the size of the optical pumping beams and estimate the number of trapped molecules. To estimate the helium density in the trapping region, we incorporate the He-CaF collisions to the simulation, which will be discussed in Sec. 5.4. The simulated trap lifetimes under different background He densities and $\gamma_{col,He-CaF}$ values will be presented and compared to the measured trap lifetime in Sec. 5.5.

5.1 Optical loading simulations

The simulation program starts by generating the molecule's initial position within the 2nd cell aperture and velocity based on the measured beam velocity distribution of the two-stage cell. The molecular beam defines the coordinate system, where central line of the beam is along the z axis and the 2nd cell aperture is located at $z = 0$. The transverse beam direction is on the $x - y$ plane. Fig. 5.1(a) plots the initial particle positions constrained to be within the diameter of the aperture (9 mm). We specify the the CaH beam properties of $(v_f, \delta v_l, \delta v_t) = (65, 40, 50)$ m/s, where v_f is the peak forward velocity, δv_l is the longitudinal velocity width, and δv_t is the transverse velocity width. The generated velocity distributions are depicted in

Fig. 5.1(b) and (c), and they agree well with the specified initial conditions.

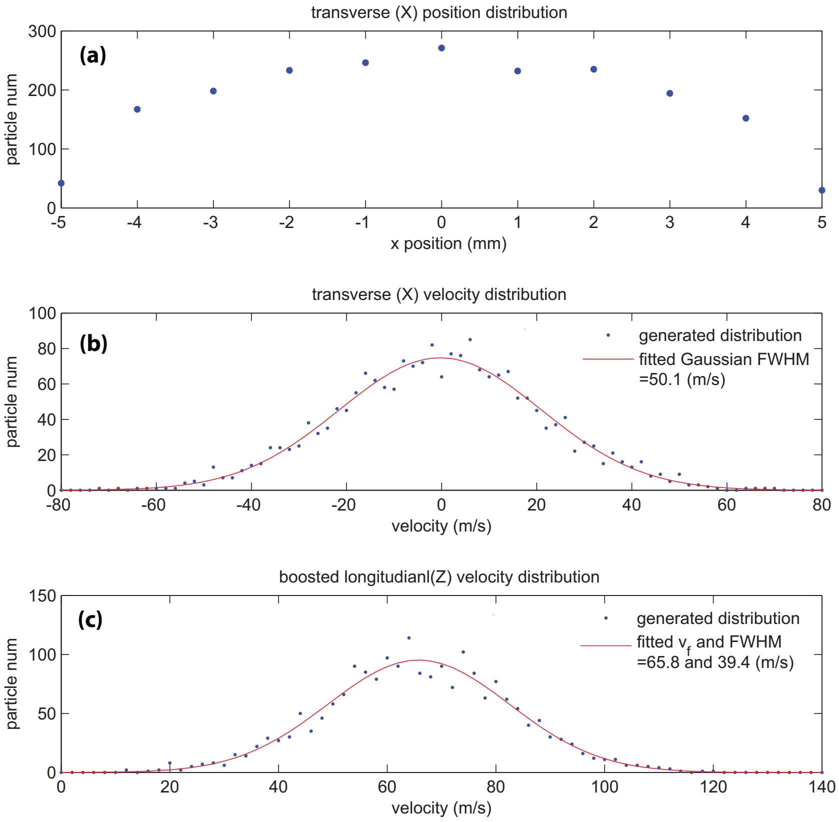
transverse (X) position distribution

transverse (X) velocity distribution

boosted longitudianl(Z) velocity distribution

Figure 5.1: (a) Transverse positions of the molecules generated along the x axis. We define the molecular beam direction (or longitudinal direction) as the z axis in the simulation. The beam velocity specification is $(v_f, \delta v_l, \delta v_t)$ $= (65, 40, 50)$ m/s in the simulation. The generated transverse velocity distribution and longitudinal velocity distribution are plotted in blue dots in (b) and (c), respectively.

The magnetic field of the quadrupole trap is calculated using Biot−Savart law numerically in Matlab and then stored in a 3D grid. Note again that the coil specifications for our trap (*Mark 5* Magnet) are listed in Ref. [79]. The generated field along the central line of the magnetic trap was shown in Fig. 4.7. The field of the magnetic lens is generated using *Raida* within the Mathematica environment. In that program, we need to specify the geometry of the magnetic lens, which is given by the permanent magnets we obtain, and the magnetization vector of the material, which is not known for our permanent magnets. We constrain the magnetization vector by matching the calculated field profile on the midplane of the lens to the measured values shown in Fig. 4.3.

We adopt the second-order Runge-Kutta method to simulate the trajectories of molecules inside the magnetic fields of the lens and trap. The molecular position and velocity as a function of time can be numerically solved based on the initial condition of the molecule. The magnetic potential experienced by the molecule $U = (state) \times \mu_B|\vec{B}(x,y,z)|$, where $state = +1$ for the LFS and $state = -1$ for the HFS. The magnetic force is hence $\vec{F}(x,y,z) = -\nabla U(x,y,z)$ and the equations of motion along x axis are

$$\begin{aligned} \frac{dx}{dt} &= v_x \\ \frac{dv_x}{dt} &= \frac{F_x(x,y,z)}{M} \end{aligned} \tag{5.1}$$

Based on the 2nd order Runge-Kutta (R-K) method, the solutions can be written as [82]

$$\begin{aligned} x' &= x + k_{2x} \\ v_x' &= v_x + k_{2v_x}, \end{aligned} \tag{5.2}$$

where x' and x are the positions at $t + dt$ and t. The coefficients are given by

$$\begin{aligned}
k_{1x} &= v_x dt \\
k_{1v_x} &= \frac{F_x(x, y, z)}{M} dt \\
k_{2x} &= (v_x + \frac{1}{2} k_{1v_x}) dt \\
k_{2v_x} &= \frac{1}{M} F_x(x + \frac{1}{2} k_{1x}, y, z) dt
\end{aligned} \tag{5.3}$$

The solutions of the positions and velocities along the y and z directions can be written down similarly. We test the simulation codes, which use 2nd order R-K method, on a simple harmonic oscillator (SHO). The simulated position and kinetic energy of the 1D SHO are depicted in red in Fig. 5.2(a) and (b), respectively. As a comparison, we plot the analytical solution of the SHO in blue, indicating good agreement between the simulated trajectory using 2nd order R-K method and the analytical solution.

With the molecule's initial position and velocity, the magnetic field profile, and solutions of the equation of motion generated, the optical loading process can also be modeled. The algorithm is as follows:

(1) Simulate the molecular trajectory starting from the exit aperture at $t = 0$, going through the magnetic lens, and then entering the magnetic trap. The initial internal state is low-field seeking (or $state = +1$).

(2) When the low-field seeking molecule reaches $|\vec{B}| = B_1$, change the internal state from $state = +1$ to $state = -1$, and then continue propagating the molecular trajectory according to the magnetic potential experienced by the HFS.

(3) When the high-field seeking molecule reaches $|\vec{B}| = B_2$, change the internal

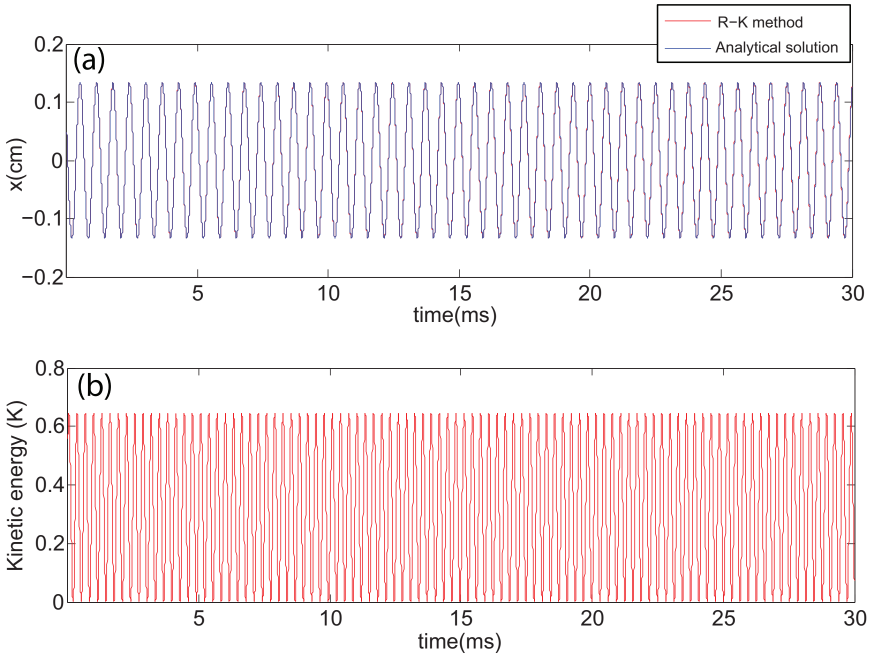

Figure 5.2: (a) Simulated position of a SHO using the 2nd order R-K method is shown in red. The analytical solution is plotted in blue as a comparison. (b) Simulated kinetic energy and analytical solution of the SHO are depicted in red and blue, respectively.

state from $state = -1$ back to $state = +1$, and continue simulating the trajectory up to 40 ms.

For each individual time step of $dt \sim 1\mu$s, we check whether the molecule reaches the inner surface of the magnetic lens or magnet cask. The assembled lens has an inner radius and length of 12.45 mm and 25.4 mm, respectively. The inner radius and length of the magnet cask is 3.91 cm and 28.96 cm, respectively. If the molecule collides with the physical walls of the magnetic lens or magnet cask, we terminate the trajectory simulation.

5.2 Optical loading of CaH-simulation results

5.2.1 Trajectories of loaded CaH

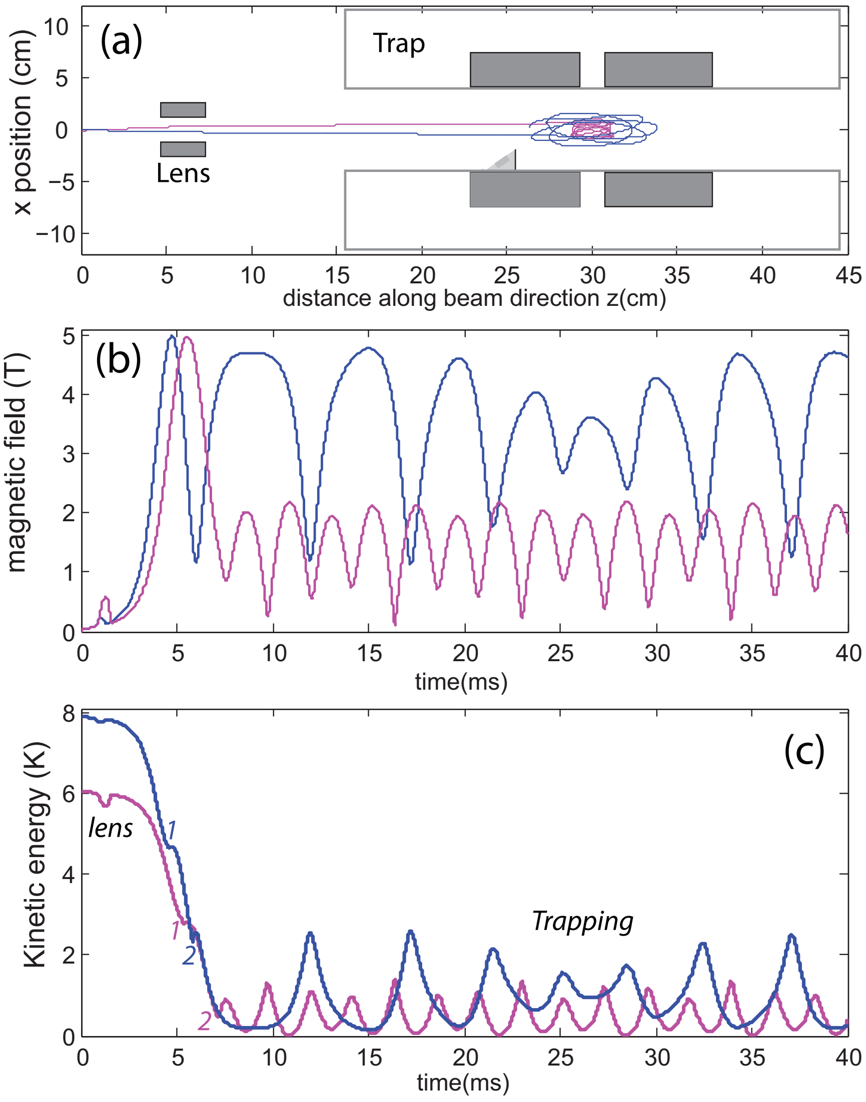

Figure 5.3: (a) Simulated trajectories of the loaded CaH molecules into the trap at 140 A. The 2nd cell aperture locates at $z = 0$. (b) Magnetic fields experienced by the loaded molecules. The optical pumping fields are (B_1, B_2)=$(4.9, 1.5)$ T. (c) Kinetic energies of the loaded molecules versus time. Here, we denote the moment of molecules passing the lens as *lens*, being optically pumped as *1* and *2*, and being loaded in the trap as *Trapping*.

Fig. 5.3(a) shows the simulated trajectories of two loaded CaH molecules into the magnetic trap at 140 A, where we assume $(v_f, dv_l, dv_t) = (65, 40, 50)$ m/s and (B_1, B_2) $= (4.9, 1.5)$ T. The magnetic fields experienced by the molecules and molecular kinetic energies are depicted in (b) and (c). At t ~1 ms, the molecular beam reaches the magnetic lens and experiences the lens field. Around $t = 5$ ms, the molecules arrive the saddle point and are decelerated, which is reflected in the decreased kinetic energies. Molecules in the low-field seeking state are pumped to the high-field seeking state at $B_1 = 4.9$ T, and then continue to be decelerated until reaching $B_2 = 1.5$ T at $t = 6 - 7$ ms. After being pumped back to the low-field seeking state, molecules with kinetic energy lower than the trap depth can sustain stable orbits.

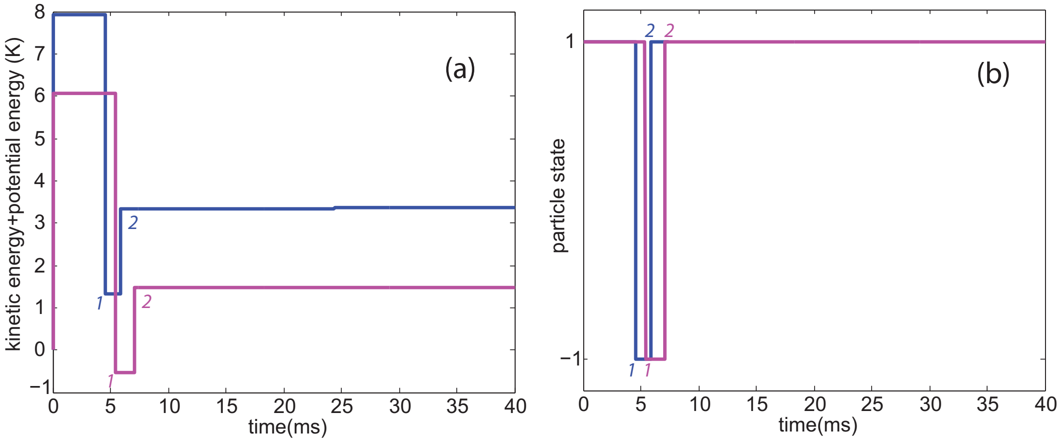

Figure 5.4: (a) The sum of the kinetic and potential energies of the loaded molecules. The 1st (2nd) optical pumping event is denoted as *1* (*2*). (b) Internal state of the molecules.

We plot the sum of kinetic energies and potential energies of the two loaded molecules (with trajectories shown in Fig. 5.3) in Fig. 5.4(a) and the internal states of these molecules in (b). The total energy conserves in the simulation before the 1st pumping and after the 2nd optical pumping events, which are denoted as *1* and *2* in

Fig. 5.4(a). Right before the 1st optical pumping, the kinetic energy of the molecule is $KE = KE(t = 0) - \mu_B \times B_1$. Right after the 1st pumping stage, molecules are in the high-field seeking state, and the sum of the kinetic and potential energies is $E_t = KE + U = KE(t = 0) - 2\mu_B \times B_1 = KE(t = 0) - 6.6$ K. Therefore, the total energy after the 1st pumping event can fall below zero.

5.2.2 Simulated capture velocity

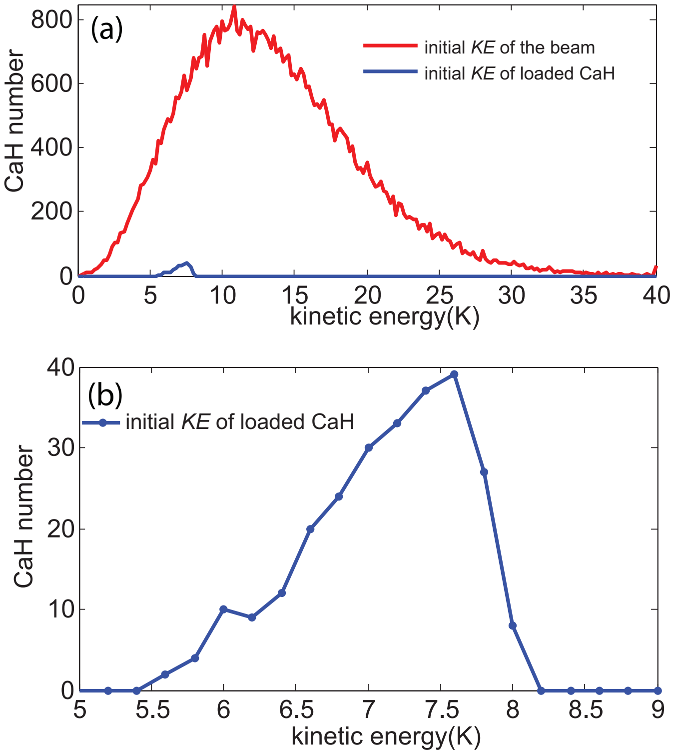

Figure 5.5: (a) Simulated initial kinetic energy distribution of $N_0 = 5.6 \times 10^4$ CaH molecules is plotted in red. Simulation parameters: $(v_f, dv_l, dv_t) = (65, 40, 50)$ m/s and $(B_1, B_2) = (4.9, 1.5)$ T. Trap at 30 cm and Lens at 6 cm. A fraction of the molecules are loaded, giving a loading efficiency of $N_{loaded}/N_0 = 4.6 \times 10^{-3}$. We depict these loaded molecules' initial kinetic energy distribution as blue. (b) We enlarge the initial KE distribution of the loaded molecules here. The expected capture energy is 5.56 K $< KE(t = 0) <$7.84 K.

The simulation results are consistent with the physical picture of the system. Since we can estimate the capture energy of the loading process based on the energy argument (Eq. 3.11), we can compare that with the simulated capture energy. Fig. 5.5(a) plots the initial kinetic energy distribution of $N_0 = 5.6\times10^4$ CaH molecules with $(v_f, dv_l, dv_t)=(65, 40, 50)$ m/s (red curve). The number of loaded CaH molecules is $N_{loaded} = 255$, corresponding to a loading efficiency of $N_{loaded}/N_0 \equiv 4.6 \times 10^{-3}$, where N_0 is the number of molecules outside the cell and we assume the efficiency of the optical pumping process itself is 100% for simplicity. To know the capture energy, we show the initial kinetic energy distribution of these loaded molecules in blue trace in Fig. 5.5(a). We enlarge the loaded distribution in Fig. 5.5(b). According to Eq. 3.11, the capture energy is $\mu_B(2B_1 - B_2) < KE(t = 0) < \mu_B(3B_1 - 2B_2)$, giving 5.56 K $< KE(t = 0) <$ 7.84 K using $(B_1, B_2)=(4.9, 1.5)$ T. This range is consistent with the simulated results shown in Fig. 5.5(b). Since the simulation results presented above make physical sense, we have confidence in the results and we use the trajectory simulations to explore the optimal parameters for trap loading.

5.2.3 Determination of pumping parameters

We determine the beam diameters of the optical pumping lasers based on optimization of the simulated trajectories of the loaded molecules. Fig. 5.6 depicts the trajectories of the 35 loaded CaH molecules. The collimation of the beam due to the magnetic lens is clear and the diameter of the loadable beam is roughly the same as the inner diameter of the lens.

Based on the trajectories of the 255 loaded CaH molecules, we learn the follow-

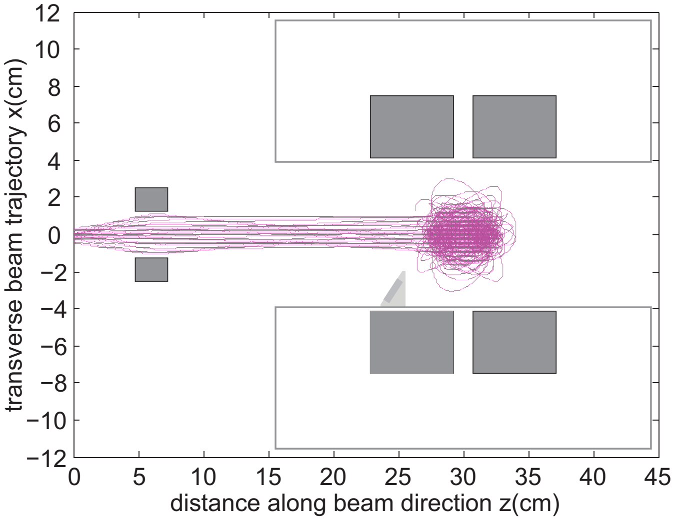

Figure 5.6: Simulated trajectories of 35 loaded CaH molecules. Simulation parameters: (v_f, dv_l, dv_t)=(65, 40, 50) m/s and (B_1, B_2)=(4.9, 1.5) T.

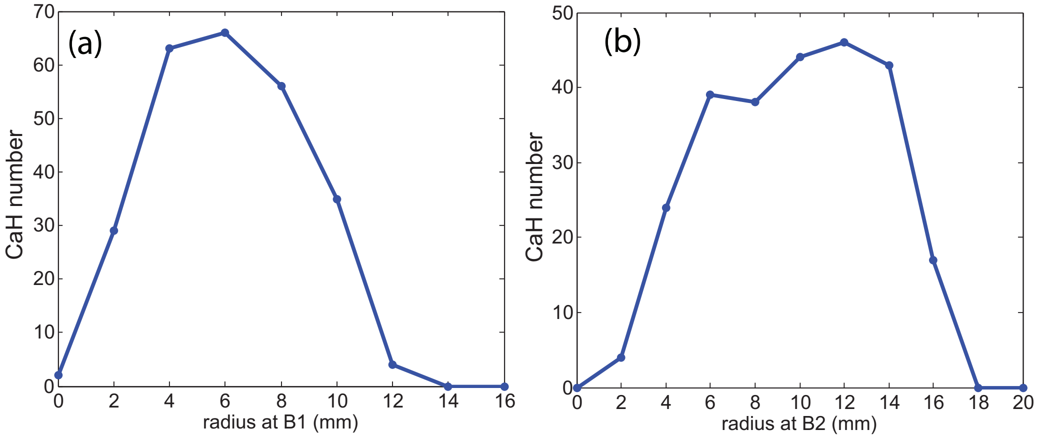

Figure 5.7: (a) Simulated radial distribution of the loaded beam at B_1. Simulation parameters: (v_f, dv_l, dv_t)=(65, 40, 50) m/s and (B_1, B_2)=(4.9, 1.5) T. Trap at 30 cm and Lens at 6 cm. (b) Simulated radial distribution of the loaded beam at B_2.

ing:

- The first optical pumping should occur at $\bar{z_1} = 24.53$ cm (5.47 cm from the trap center) with $z_{1,rms} = 1.2$ mm. The radial distribution of the loaded molecules at B_1 is shown in Fig. 5.7(a).

- The 2nd optical pumping should occur at $\bar{z_2} = 29.32$ cm (0.68 cm from the trap center) with $z_{2,rms} = 1.7$ mm. The radial distribution of the loaded molecules at B_2 is illustrated in Fig. 5.7(b).
- The average radius of the loaded cloud under these conditions is 1.77 cm.

Therefore, we choose the location of the two mirrors for the 1st pumping stage to be in the center at $\bar{z_1}$ inside the magnet (Fig. 4.14). In addition, the dimensions of the optics are designed to address the loadable molecules as much as possible. The prism assembly has a clear aperture of $0.9''$ along the transverse beam direction, which also sets the dimension of the 1st OPL along x axis to be 22.9 mm. The 45 degree mirror limits the width of the 1st OPL along the longitudinal beam direction (or z axis) to be 9.84 mm. The diameter of the 2nd OPL in the experiment is $1.5''$.

5.2.4 Loading efficiency versus other parameters

Fig. 5.8 shows the loading efficiency of CaH versus B_2 for three different trap depths. We pump the LFS at the saddle in these three cases. The loading efficiency is significantly less at a low trap depth.

Reducing the transverse temperature of the buffer-gas beam can be achieved for laser coolable atoms. Applying direct laser cooling to molecules with diagonal Franck-Condon factors, including SrF, CaF, CaH, and YO, is more technically challenging but achievable. The other possibility to generate a colder beam in both the longitudinal and transverse directions is to introduce the molecules in a different way other than laser ablation. We simulate the loading efficiency for a hypothetic CaH beam with a transverse velocity width of 35 m/s, which is illustrated in Fig. 5.9. A colder

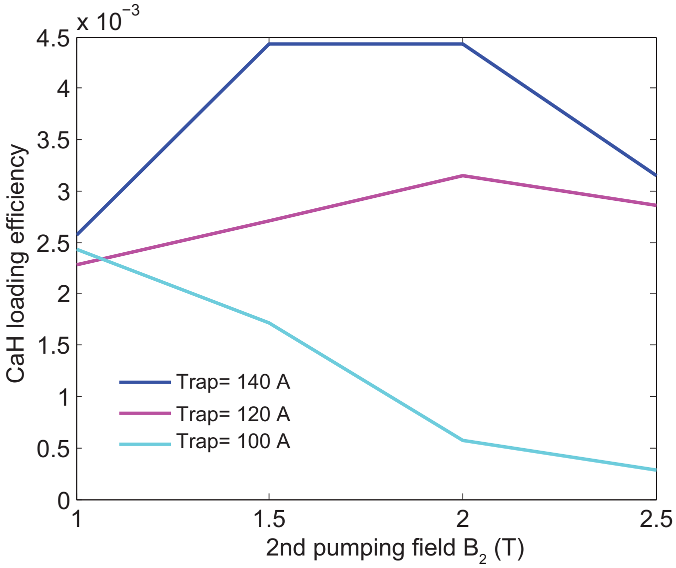

Figure 5.8: Simulated loading efficiency of CaH versus B_2 for three different trap depths. CaH beam: (v_f, dv_l, dv_t)=$(65, 40, 50)$ m/s. Trap at 30 cm and Lens at 6 cm.

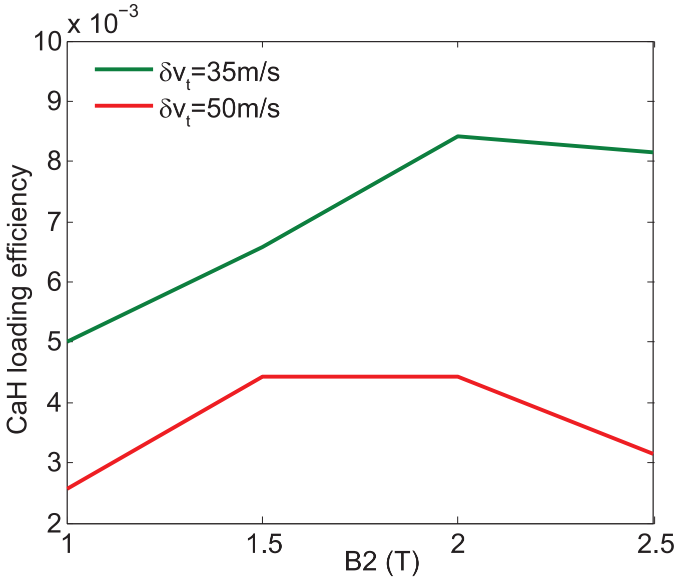

Figure 5.9: Simulated loading efficiency of a hypothetic CaH beam with $dv_t = 35$ m/s is plotted in green. As a comparison, the efficiency of the CaH beam with $dv_t = 50$ m/s is shown in red. Other simulation parameters: (v_f, dv_l)=$(65, 40)$ m/s and $B_1 = 4.9$ T. Trap at 30 cm and Lens at 6 cm.

transverse temperature certainly increases the molecular flux into the trap and the loading efficiency by a factor of 2.

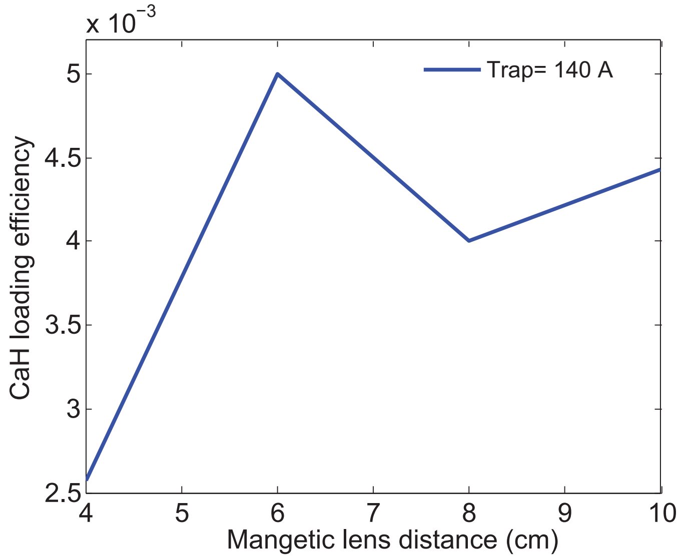

Figure 5.10: Simulated loading efficiency of CaH versus distance of the lens to the cell exit aperture. (v_f, dv_l, dv_t)=(65, 40, 50) m/s and (B_1, B_2)=(4.9, 1.5) T with trap at 30 cm.

Fig. 5.10 depicts the loading efficiency versus the relative distance between the midplane of the magnetic lens to the 2nd cell exit aperture. Here, we assume the CaH beam properties are given by the typical output of the two-stage cell with (v_f, dv_l, dv_t)=(65, 40, 50) m/s. When (B_1, B_2)=(4.9, 1.5) T, The maximum loading efficiency occurs at a relative distance of 6 cm, which is used for the trap loading experiment.

5.3 Optical loading of CaF-simulation results

The trajectory simulation of CaF trap loading assumes the beam has (v_f, dv_l, dv_t) = (55, 40, 56) m/s. The trap depth (or B_1) is set to 3.5 T and 2.17 T for loading

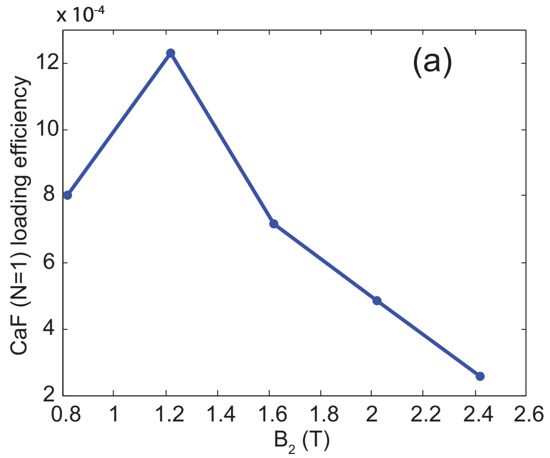

Figure 5.11: (a) Simulated loading efficiency of CaF ($N = 1$) versus B_2. $B_1 = 3.5$ T and trap is at 100 A. (b) Simulated loading efficiency of CaF ($N = 0$) versus B_2 when $B_1 = 2.17$ T and trap is at 62 A. Other simulation parameters: (v_f, dv_l, dv_t)=$(55, 40, 56)$ m/s. Trap locates at 30 cm and lens is at 6 cm.

$N = 1$ and $N = 0$, respectively. Fig. 5.11(a) plots the simulated loading efficiency versus B_2 with an maximum loading efficiency of 1.2×10^{-3} at $B_2 = 1.2$ T for loading $N = 1$. We measured the loaded CaF ($N = 1$) signal as a function of the 2nd OPL frequency in Fig. 3.14(a). The maximum signal occurs at $B_{2,exp} = 2.42$ T and a frequency detuning of 1 GHz corresponds to a change of the 2nd pumping field by 0.07 T. As we discussed in Sec. 3.2, the 2nd OPL resonant with the HFS via P_1 line may optically remove the LFS in the beam via Q_1 line when $B_2 < 2.22$ T. This can explain the discrepancy between the simulated and the measured B_2 dependencies. The simulated loading efficiency at $B_{2,exp}$=2.42 T is down to 2.5×10^{-4}. We did switch to pump the HFS using the 2nd OPL on R_1 line experimentally so that the LFS would not be optically removed and we can operate at a lower B_2. The loaded $N = 1$ signals by choosing (B_1, B_2)=$(3.5, 0.9 - 1.2)$ T with the 2nd OPL on R_1 line were comparable to the original choice of (B_1, B_2)=$(3.5, 2.27)$ T with the 2nd OPL on P_1 line. We attribute this to a lower branching ratio of the R_1 line than P_1 line back to the $N = 1$ state.

The simulated loading efficiency of $N = 0$ versus B_2 is plotted in Fig. 5.11(b) with a maximum loading efficiency of 1.4×10^{-4}. This simulated efficiency of CaF ($N = 0$) is a factor of 30 lower than CaH ($N = 0$).

5.4 Incorporating collisions in simulation

So far, we have not considered the effect of the background buffer gas in the simulation. Since ^{3}He buffer-gas inside the trap has a temperature of 4 K (the walls of the chamber are at 4 K), collisions between trapped molecules with ^{3}He can certainly cause trap loss, which is confirmed experimentally (Sec. 3.4).

To simulate the collisions between the trapped molecules and ^{3}He, we take the simulated position and velocity of the loaded molecule at B_2 as the initial condition and then incorporate the collision events as follows.

(1) Determine the time duration, τ, between two He-molecule collisions.

(2) Evolve the molecular trajectory according to the 2nd R-K method in each time step of $dt = 1\mu$s. After simulating the trajectory for a duration of τ, we perform a collision event.

(3) Repeat Step (1)-(2) for up to 300 ms.

We adopt the method presented in Bob Michniakn's thesis [66] to treat the elastic He-molecule collisions. In reality, the time between collisions τ is not a constant. The probability of the molecule encountering a collision between t and $t + dt$ after surviving for time t is given by [66]

$$P(t)dt = \frac{exp(-t/\bar{\tau})}{\bar{\tau}}dt. \tag{5.4}$$

Here, $\bar{\tau} = (n_{bg}\sigma_{el}v_{rev})^{-1}$ is the mean collision time and $v_{rev} = \sqrt{v_{p,He}^2 + \vec{v}_M^2}$ is the relative velocity, where $\vec{v}_M$ is the molecular velocity and $v_{p,He}$ is the most probable velocity of the buffer gas. The time between collisions in Step (1) is chosen according to the functional form in Eq. 5.4 for a better accuracy.

To handle the elastic collision event in Step (2), we first transform both the molecular velocity and the velocity of He, which is chosen according to the Boltzmann distribution at 4 K, to the center of mass (COM) frame. In the COM frame, an elastic collision randomizes the velocity of the molecules. This can be achieved numerically by choosing a random angle after collision while keeping the speed of the molecule the same in the COM frame. Finally, we can transform the molecular velocity back to the laboratory frame.

To test the simulation codes regarding the elastic collisions, we simulate the diffusion of a CaF cloud with an initial size of 1 mm inside a 5 cm cube cell at a temperature of 2 K. There is no magnetic field in this simulation. The ^{4}He buffer gas has a density of $n_{bg} = 10^{15}$ cm^{-3}. The elastic He-CaF cross section is assumed to be $\sigma_{el} = 10^{-14}$ cm^2. Fig. 5.12 shows the particle number decays as a function of time. An exponential decay is used to extract the diffusion time of the simulated sample at long time scale, giving us $\tau_d = 2.7$ ms. An analytical solution exists for such a diffusion problem. According to Hasted [83], the diffusion time of particles in a cube can be expressed as

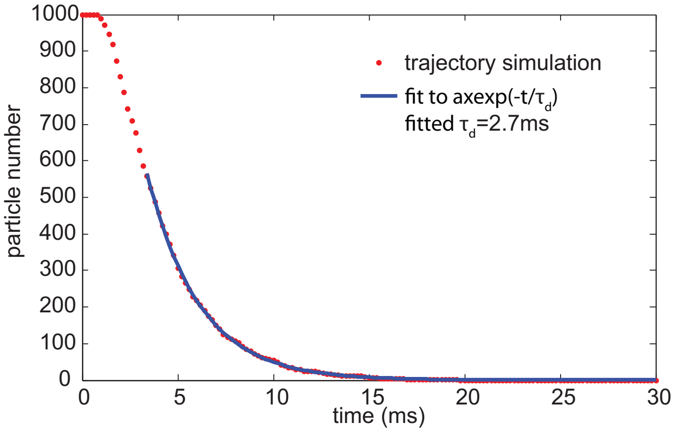

Figure 5.12: Trajectory simulation of the diffusion of CaF molecules inside the ^{4}He buffer gas at T = 2 K and $n_{bg} = 10^{15}$ cm^{-3}. The cell has a length of 5 cm. The number of particle is plotted as a function of time, and an exponential decay is fitted at the long time scale to figure out the diffusion time.

$$\tau_d = \frac{L_{cell}^2}{3\pi^2 D}, \tag{5.5}$$

where L_{cell} is the length of the cell. D is the diffusion coefficient and given by

$$D = \frac{3}{16(n_{bg} + n_{molecule})} \times \frac{2\pi k_B T_{bg}}{\mu} \times \frac{1}{\sigma_{el}}. \tag{5.6}$$

Here, μ is the reduced mass. Assuming $n_{CaF} << n_{bg}$, we can obtained an expected diffusion time of 2.7 ms according to Eq. 5.5, which is consistent with our simulation.

The inelastic He-molecule collision can be treated as follows. For each collision in Step (2) of the simulation, there is some possibility that the molecular internal state would be changed, which is determined by the ratio of elastic to inelastic collision cross section, $\gamma_{\text{col}} = \frac{\sigma_{el}}{\sigma_{in}}$. In the simulation, each collision event randomizes the velocity of the molecules in the COM frame due to the elastic collision and changes the molecular state to $state' = (-1) \times state$ with a probability govern by γ_{col}.

5.5 Trap lifetime of CaF-simulation results

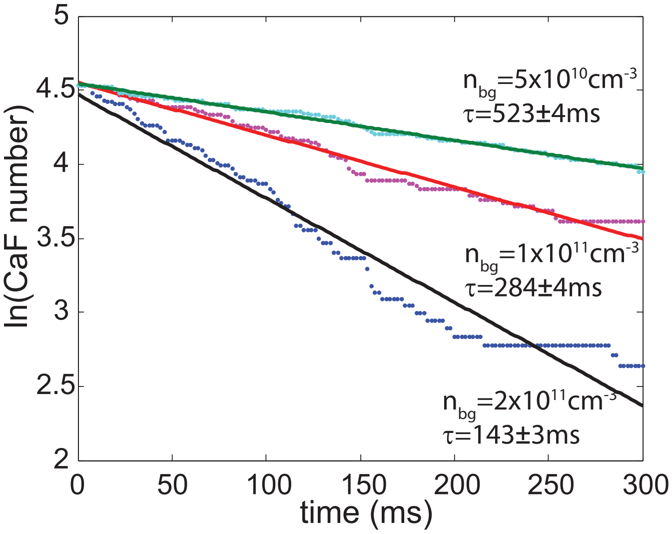

Figure 5.13: Simulated CaF ($N = 1$) time decay at different background ^{3}He (4 K) densities are plotted in green, purple, and blue dots. The collision is assumed to be elastic. Linear fits to ln(CaF number) extract the decay time constant of the simulation and are depicted solid lines.

Since the energy difference between $N = 0$ and $N = 1$ of CaF is ~ 1 K, the $N = 0$ state can be populated quickly from the initially loaded $N = 1$ molecules via collisions with He at 4 K. Elastic collisions of CaF in both rotational states with He can impart enough energy on the molecules and cause molecules to leave the trap. In addition, the spin-depolarization of $N = 0$ is much weaker than $N = 1$ according to Ref. [76] and a lower bound of $\gamma_{\mathrm{col,N=1}} > 8000$ can be placed (see Sec. 3.4). The trap loss simulation can be performed on the $N = 1$ molecules alone since only elastic collisions can cause $N = 0$ to leave the trap and would affect $N = 1$ in the same way.

Fig. 5.13 shows the simulated time decay of CaF ($N = 1$) at three different background ^{3}He densities. We ignore the inelastic collisions for now. A linear fit to decay of ln(CaF number) gives the simulated decay time. At a He density of

5×10^{10} cm^{-3}, we obtain a simulated decay time of 520 ms, which is comparable to the observed trap lifetime.

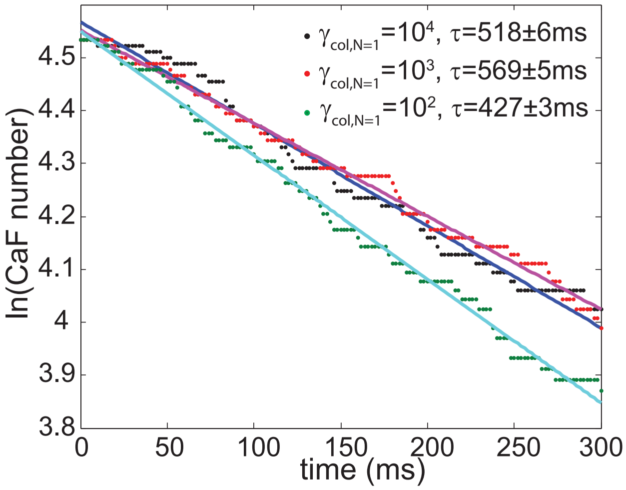

Figure 5.14: Simulated CaF ($N = 1$) number versus time for three $\gamma_{\text{col,N=1}}$ values are plotted in black, red, and green dots. $n_{bg} = 5 \times 10^{10}$ cm^{-3}.

Next, we fix the background density to be $n_{bg} = 5 \times 10^{10}$ cm^{-3} and change the $\gamma_{\text{col,N=1}}$ values in the simulation. The simulated time decay is plotted in Fig. 5.14. The simulated decay times are comparable when $\gamma_{\text{col,N=1}} = 10^3 - 10^4$. Using a vale of $\gamma_{\text{col,N=1}} = 10^2$ reduces the simulated lifetime slightly, indicating the elastic collisions dominate the observed trap loss.

The most probable velocity of ^{3}He at 4 K is 148 m/s. At a density of $5{\times}10^{10}$ cm^{-3}, the mean elastic collision time is 135 ms, where we assume the $\sigma_{el} = 10^{-14}$ cm^2 and ignore the moving velocity of the molecule. The number of elastic collisions is $\sim$ 4 within the observed decay time constant of 527 ms. This again indicates the elastic collisions limit the observed trapped CaF ($N = 1$) lifetime.

Chapter 6

Outlook

In this chapter, we are going to discuss some of the future directions based on the results presented in this thesis, including the slow molecular beams and the optical loading technique.

6.1 Co-trapping atoms with molecules and sympathetic cooling of molecules

A typical successful recipe for creating quantum degenerate atomic gases contains the following steps: starting with laser pre-cooled atoms and then applying evaporative cooling or sympathetic cooling on the trapped species. Although molecules are much harder to cool than atoms due to their complex internal structures, recent progress on direct cooling methods has shown the ability to control the molecular internal and external degrees of freedom. Two out of the three ingredients for realizing degenerate atoms–direct laser cooling and evaporative cooling of molecules [47,49,50]–

have been demonstrated separately on two types of molecules. The idea of sympathetic cooling is quite simple. If we want to cool the species of interest, we allow it to be in thermal contact with other colder species. Buffer-gas cooling of molecules with the cold inert helium gas is actually one of the examples of sympathetic cooling. However, the vapor pressure of ^{3}He drops below 10^{15} cm^{-3} at 200 mK [84], which sets the lowest temperature we can reach utilizing He as the coolant. A natural choice of a coolant for bringing molecules to ultracold temperature is laser cooled atoms. To realize sympathetic cooling of neutral molecules, one might rely on a simultaneous confinement of atoms and molecules with favorable collision properties.

The optical loading method we demonstrated in this thesis is ideal for loading two species of interest into a magnetic trap by simply introducing one more ablation target and two more optical pumping lasers. A rule of thumb for choosing the atomic coolant is a ratio of elastic to inelastic cross sections of $\gamma_{\rm col} > 100$ [85]. Ref. [86] identified the properties of a good collision pair: (1) a light atom so that the centrifugal barrier of the outgoing channel is high enough to suppress the inelastic collisions, (2) Hund's case (b) molecules, such as NH and CaH, where the electron is weakly coupled to the molecular axis, and (3) an atom with an isotropic potential energy surface, such as alkaline earth atoms.

Several collision pairs have been predicted to have favorable collisional properties, including Mg-NH [85], N-NH [7], Mg-CaH [87], and Li-CaH [87]. Co-trapping N with NH has been realized using the traditional in-cell buffer-gas loading method [7]. However, a lack of a simple laser cooling scheme for atomic N and the presence of the background buffer gas hinder sympathetic cooling of NH experimentally. Light and laser coolable alkaline earth atoms seem to be a good candidate, yet trapping of these atoms can only be realized in a magneto-optical trap with small magnetic field gradient or an optical dipole trap with a small trap depth and volume.

6.1.1 Sympathetic cooling of CaH with Li

The atom-molecule pair we plan to study is Li-CaH. By using rigorous quantum scattering calculations, Ref. [87] predicts this pair should have elastic-to-inelastic collision ratios of $\gamma_{\text{col}} > 100$ from 10 mK down to 10 μK inside a magnetic trap. This finding implies the possibility of sympathetic cooling of CaH by using Li as a coolant in the magnetic trap. Although the Li-CaH interaction potential is fairly anisotropic compared to He-CaH, Ref. [87] pointed out that the spin depolarization mechanism of CaH due to the interaction potential is very similar to that of the He-CaH collision. When $^2\Sigma$ molecules in the rotationally ground state collide with atoms, the interaction potential does not directly couple to the electronic spin. However, the anisotropic part of the potential can excite the molecule to the first rotationally excited state, where the molecular spin-rotational coupling can change the projection of the electronic spin [88]. This corresponds to a scaling law of $\gamma_{\text{col}} \propto \gamma_v^2$, where γ_v is the spin-rotational constant. Even if the interaction potential of Li-$^2\Sigma$ molecules is fairly anisotropic, the spin depolarization can be suppressed by choosing molecules with small γ_v. Several $^2\Sigma$ molecules are expected to have similar collision properties with Li atoms [87].

Compared to CaF, optical loading of CaH has some advantages. Since CaH has an order of magnitude larger rotational constant ($B_{CaH} = 6.09$ K) than CaF

($B_{CaF} = 0.49$ K), we should be able to operate the magnetic trap at its full strength of 4.9 T. We note that the experiment on trapping of CaH, as presented in Section 3.6, was performed at 3.5 T. This is because the PTC lost its cooling power due to a leak, resulting in a higher than normal operating temperature and preventing the operation of the trap at its full strength. We expect to resolve this technical problem in the near future. By choosing $(B_1, B_2) = (4.9, 1.5)$ T, we obtain a simulated loading efficiency of $N_{loaded}/N_0 = 4.5 \times 10^{-3}$ (see Fig. 5.8), where N_{loaded} and N_0 are the number of loaded molecules and the molecular number just outside the beam cell, respectively. Note again that we do not consider the inefficiency during the optical pumping process. This loading efficiency is an order of magnitude larger than the simulated value of $\sim 3 \times 10^{-4}$ for CaF ($N = 1$) using $(B_1, B_2) = (3.5, 2.3)$ T (see Sec.5.3). In addition, the corresponding trap depth of 2.3 K for loaded CaH can lead to a much longer trap lifetime than CaF when colliding with the background He gas, giving more time to reach fully UHV conditions.

6.1.2 Estimation of the number of loaded Li

We expect to load a much larger number of Li atoms into the trap compared to CaF. A large ablation yield of 10^{15} Li atoms/pulse was reported previously [89], which is four orders of magnitude higher than our CaF yield. Fig. 6.1 plots the simulated loading efficiency of ^{7}Li using the optical pumping method, where we assume the efficiency of the optical pumping process is 100%. Since we have not produced a Li beam yet, we guess its properties by scaling the velocities of the CaH beam. For a Li beam with a peak moving velocity of $v_{f,Li} = 98$ m/s, we obtain an extremely

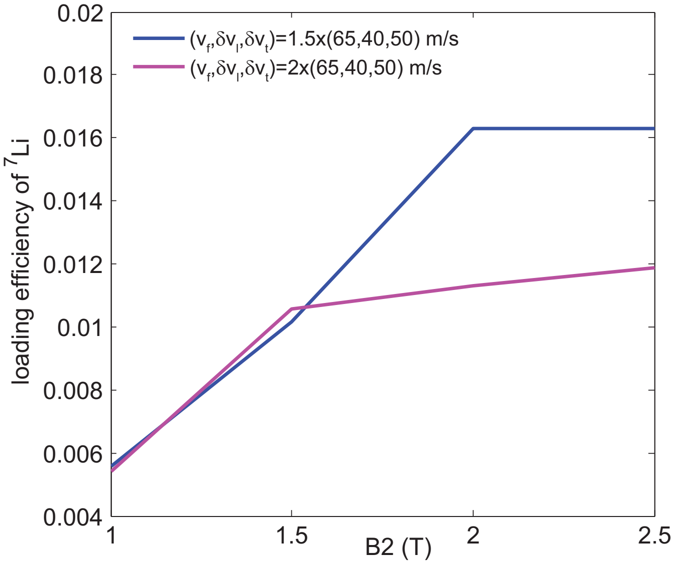

Figure 6.1: Simulated loading efficiency of ^{7}Li beams with $(v_f, \delta v_l, \delta v_t)$=1.5 × $(65, 40, 50)$ m/s is plotted in blue trace and $(v_f, \delta v_l, \delta v_t)$=2 × $(65, 40, 50)$ m/s is depicted in magenta trace. Other simulation parameters: trap is at 140 A and locates at 30 cm; magnetic lens locates at 6 cm.

high loading efficiency of 1.6% at $(B_1, B_2) = (4.9, 2)$ T, which is almost two orders of magnitude larger than loading CaF. The corresponding capture velocity and trap depth for Li is $v_c = 111 - 130$ m/s and 1.95 K, respectively. The capture velocity is higher than the typical peak velocity of the two-stage source operating at low flows and low YAG energies. To obtain a fast Li beam, we can simply increase the YAG energy and the repetition rate. There is no leakage to dark states during the pumping process, which makes the optical pumping process efficient. This loading method allows accumulating multiple pulses of Li atoms. Using the cryogenic shutter with an opening duration of 15 ms, we expect to load roughly 10 atomic Li pulses. Therefore, we project a loaded Li number of 2×10^{11} in the trap. We believe observing Li-molecule collisions is within reach given the attained trap lifetime of molecules. Potential ways to improve the trap vacuum have been discussed in Sec. 3.4, which should increase the trap lifetime significantly. Finally, we expect to further increase the loaded Li numbers by simply implementing transverse laser cooling of Li beams outside the cell.

6.1.3 Controlled chemical reaction

Li + CaH → LiH + Ca chemical reaction is exothermic by 0.67 eV [87]. Unpolarized Li+CaH reactants were measured to react at a rate of 3.6×10^{-10} cm^3/s at ~ 1 K [89]. By confining both species inside the magnetic trap, we realize a spin polarized sample. According to Ref. [87], the interaction potential between spin polarized Li + CaH has a potential barrier. This can be intuitively understood based on the Pauli exclusion principle [6]. Therefore, we expect this cold chemical reaction channel to be forbidden in our system, which is a big step toward controlled chemical reaction.

The suppression of chemical reactions using external magnetic field has been observed in a magnetically trapped N-NH pair. The loss rate of the trapped NH due to the presence N atoms was measured to be 9×10^{-13} cm^3/s [7], which is an order of smaller than the calculated chemical reaction rate of 3×10^{-11} cm^3/s [4]. A comparison between the measured trap loss rate of CaH due to Li and the measured reaction rate provides a direct evidence of cold control chemistry.

6.1.4 Evaporative cooling of Li in the trap

If the nature of Li-CaH collisions turns out to be favorable, we will need to further cool the Li atoms in the trap, which will then cool the CaH molecules. One way to reduce the temperature of the loaded Li atoms is evaporative cooling.

Since the initially loaded Li cloud samples a field up to 4.9 T, evaporative cooling using a RF knife requires a high power microwave source with a frequency > 30 GHz. The power of the microwave needed can be estimated using Landau-Zener approximation, $P_{LFS}(t \rightarrow \infty) = e^{-\frac{2\pi\Omega^2}{\dot{\Delta}}} \sim 0.5$. Here, we assume the avoided crossing is created by the magnetic field of the microwave source with $\Omega = \mu_B \times B_{MW}/h$, causing 50% of the LFS to become the HFS. We assume the Li atoms are decelerated to a kinetic energy of 0.5 K near the trap edge, which corresponds to a velocity of 34 m/s. The time derivative of the frequency difference between the LFS and HFS is $\dot{\Delta} = \frac{2\mu_B}{h} \times \frac{\partial B}{\partial x} \times v = 9.5 \times 10^{13}\ \mathrm{s}^{-2}$, where we take the trap field gradient to be 1 T/cm. Therefore, the magnetic field of the microwave needed is $B_{MW} = 2.3 \times 10^{-4}$ T, corresponding to a microwave power of 10 kW for illuminating the trapped cloud with a radius of 1.8 cm. Note that we use the trajectory simulation results of CaH in Sec. 5.2 to estimate the size of the trapped cloud and the velocity at high fields. The microwave power needed is not feasible in our setup.

By ramping down one coil of the quadrupole trap while keeping the other at a constant current, the trap center can be shifted so that the outer orbits of the trapped cloud intersect a physical wall of the cell. This method preferentially removes more energetic species and leads to evaporation. This type of surface evaporation had been implemented in metastable ^{4}He, resulting in cooling of the sample from 0.4 K to 1.4 mK in 200 s (Ref. [90], p. 121). To implement a similar surface evaporation on loaded Li atoms in our system, we will need to introduce one more current lead in order to independently control the two coils. As discussed in Sec. 4.4, the heatload from the three current leads is close to the cooling capacity of the pulse tube cooler.

Introducing a fourth lead may be technically challenging. An alternative approach is to introduce a movable cold surface from one of the ports of the magnetic cask to act as a solid knife. The distance of cold surface to the trapped cloud can be controlled by a linear motor feedthrough from the room temperature side. The issue of reduced dimensionality evaporation would need to be addressed for any surface evaporation scheme.

6.2 Laser cooling and Sisyphus cooling of CaF in the trap

Laser cooling of CaF ($N = 1$) is feasible by driving a $X^2\Sigma^+(v = 0, N = 1) \rightarrow A^2\Pi_{1/2}(v' = 0, J' = 1/2)$ transition, where the rotational leakage can be suppressed after spontaneous emission. This direction is pursued by two research groups currently [91,92]. Since the Franck-Condon factors of the $X-A$ transition are $q_{v'=0,v=0} = 0.964$ and $q_{v'=0,v=1} = 0.035$ [93], at least one vibrational repump laser is necessary for cycling 1000 photons. In addition, the $X-A$ transition is not suitable for laser cooling of CaF ($N = 1$) in our quadrupole trap due to a large Zeeman broadening. By contrast, the X and B states have very similar g factors so that the measured trapped spectrum has a width of only 140 MHz, as shown in Fig. 3.11. In addition, the Franck-Condon factors of the $X - B$ transition are $q_{v'=0,v=0} = 0.999$ and $q_{v'=0,v=1} = 1.34 \times 10^{-3}$ [61], which is even more diagonal than the $X - A$ transition. We may be able to cool the trapped CaF ($N = 1$) with the scattering of 1000 photons without any vibrational repump lasers.

The next question we need to consider is how many photons we can scatter after considering the potential dark states, including the rotation, hyperfine, and Zeeman dark states. For the $X^2\Sigma^+(v=0, N=1) \rightarrow B^2\Sigma^+(v'=0, N'=0)$ transition, $N'=0$ state can only decay back to $N=1$ state, and hence the rotational leakage can be suppressed as well. Inside the trap, the low-field seeking manifold consists of several hyperfine levels, which may turn into dark states but remain trapped after scattering photons. If the molecules decay to the high-field seeking states, they would be lost from the trap. We will first discuss how many photons we can scatter before losing molecules to HFS states. Next, we will discuss how to remix the hyperfine states within the LFS manifold.

6.2.1 Leakage to HFS state-hyperfine interaction ignored

Let's start with a simplified situation where the hyperfine interactions are ignored. The Hamiltonian can be written as

$$H = \gamma_v \vec{N} \cdot \vec{S} + g_S \mu_B B_Z T^1_{p=0}(\vec{S}). \tag{6.1}$$

Fig. 6.2 shows the Zeeman levels of the CaF in $X^2\Sigma^+(N=1)$ and $B^2\Sigma^+(N'=0)$ states. The optical transitions for the LFS are shown in green with the appropriate polarizations. At low magnetic fields, the good quantum numbers are $|N, S, J, m_J\rangle$. At high fields, the good quantum numbers to describe the system are $|N, m_N; S, m_S\rangle$. Since the spin-rotational interaction of CaF in the X state is weak ($\gamma_v = 39.6$ MHz [74]), we can use $|N, m_N; S, m_S\rangle$ basis set at a field of $B > h \times \gamma_v / \mu_B \approx 2.8 \times 10^{-3}$ T. In addition, the projection of electronic spin in the field should be preserved during the optical transition at high magnetic fields. The selection rule should be $\Delta N = 0, \pm 1$

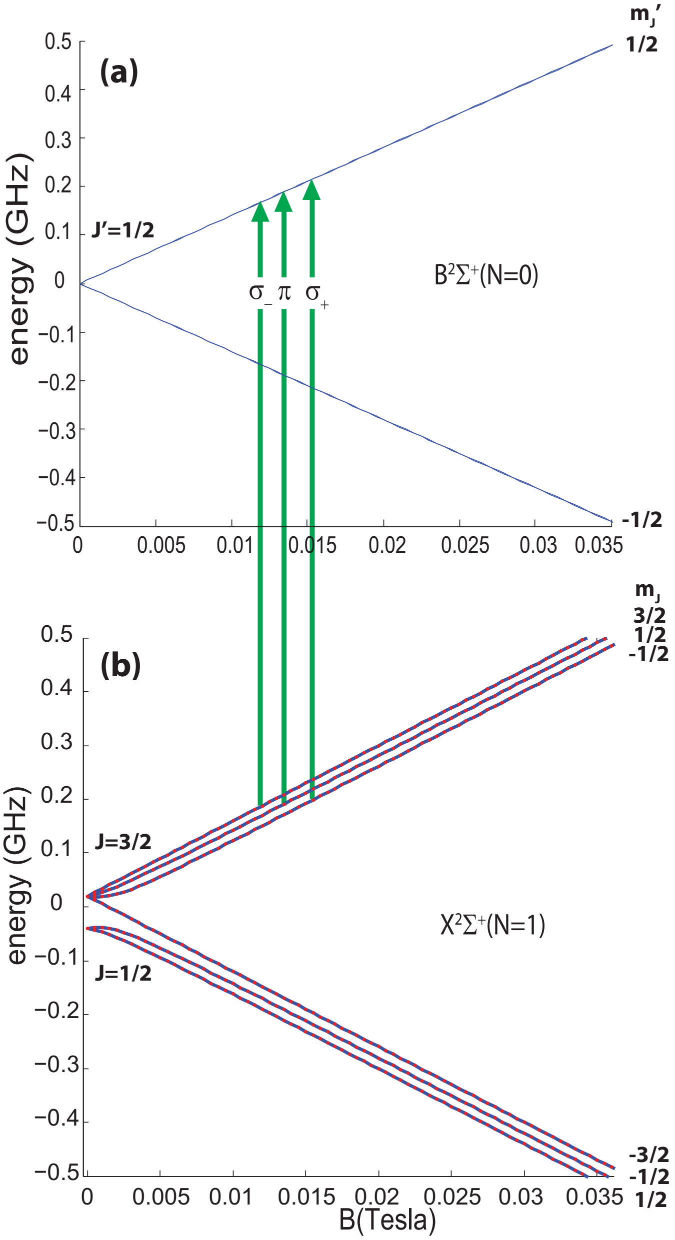

Figure 6.2: Calculated Zeeman level of CaF in (a) $B^2\Sigma^+$ ($N' = 0$) and (b) $X^2\Sigma^+$ ($N = 1$). The solutions shown in blue traces in (b) are solved in fully coupled molecular bases $|N, S, J, m_J\rangle$ and in red are in decoupled bases $|N, m_N, S, m_N\rangle$. Here, the hyperfine interaction is ignored. The laser transitions with the polarizations involved in exciting the LFS states are shown in green arrows.

and $\Delta m_N = 0, \pm 1$.

If we excite the LFS to the excited state, $|m'_J = 1/2\rangle = |N' = 0, m'_N = 0; S' = 1/2, m'_S = 1/2\rangle$, there's some probability that the molecules would end up in the HFS ($|m_J = \pm 1/2\rangle$) due to the spin-rotational interaction which mixes the $|m_S = \pm 1/2\rangle$ in the field. The amplitude of the mixing between the $|m_S = \pm 1/2\rangle$ states in the field can be estimated based on the perturbation theory. The HFS in $|m_J = \pm 1/2\rangle$ can be expressed as

$$\begin{aligned} |\mathrm{HFS}(m_J = -1/2)\rangle &\approx |m_N = 0, m_S = -1/2\rangle + \frac{\gamma_v}{2\mu_B \times B} |m_N = -1, m_S = 1/2\rangle \\ |\mathrm{HFS}(m_J = 1/2)\rangle &\approx |m_N = 1, m_S = -1/2\rangle + \frac{\gamma_v}{2\mu_B \times B} |m_N = 0, m_S = 1/2\rangle \end{aligned} \tag{6.2}$$

Here, the mixing coefficient $\frac{\gamma_v}{2\mu_B \times B} = 4 \times 10^{-3}$ at $B = 0.35$ T, which is an order of magnitude smaller than the avoided crossing of the $N = 1$ state. The possibility of ending up in HFS relative that of the LFS is approximately

$$\begin{aligned} \frac{P_{HFS}}{P_{LFS}} &= \frac{|\langle m'_J = 1/2| \vec{d} \cdot \vec{E} \, |HFS\rangle|^2}{|\langle m'_J = 1/2| \vec{d} \cdot \vec{E} \, |LFS\rangle|^2} \\ &\approx (\frac{\gamma}{2\mu_B \times B})^2 \approx 10^{-5}, \end{aligned} \tag{6.3}$$

where the coefficient is evaluated at $B = 0.35$ T. This means that we can scatter up to 10^5 photons without decaying to the HFS state at $B > 0.35$ T. Note again that the hyperfine interaction is ignored for now. The above arguments are based on the perturbation theory. We can obtain the exact energy levels by numerically diagonalizing the Hamiltonian (Eq. 6.1). At $B = 0.35$ T, the eigenvectors expressed in $|N, m_N; S, m_S>$ basis set are

$$\begin{aligned}
|m_J = 3/2\rangle &= |1, 1/2\rangle \\
|m_J = 1/2\rangle &= 0.0029\,|1, -1/2\rangle + |0, 1/2\rangle \\
|m_J = -1/2\rangle &= 0.0029\,|0, -1/2\rangle + |-1, 1/2\rangle \\
|m_J = -3/2\rangle &= |-1, -1/2\rangle \\
|m_J = -1/2\rangle &= |0, -1/2\rangle - 0.0029\,|-1, 1/2\rangle \\
|m_J = 1/2\rangle &= |1, -1/2\rangle - 0.0029\,|0, 1/2\rangle
\end{aligned} \tag{6.4}$$

Here, the eigenvectors are arranged in descending energies. The quantum numbers, $N = 1$ and $S = 1/2$, are omitted on the right hand side of the equations. The first three states belong to the low-field seeking manifold and the last three are the HFS. The coefficients obtained from the numerical results are consistent with the estimation based on the perturbation theory.

6.2.2 Leakage to HFS state-hyperfine interaction included

Since the Fermi contact interaction, $b_F = 122.6$ MHz, is larger than the spin-rotational interaction, $\gamma_v = 39.6$ MHz, for CaF, we should consider the following Hamiltonian including the hyperfine interaction:

$$H = B_v N \times (N+1) + \gamma_v \vec{N} \cdot \vec{S} + g_S \mu_B B_Z T^1_{p=0}(\vec{S}) - g_I \mu_B B_Z T^1_{p=0}(\vec{I}) + b_F \vec{I} \cdot \vec{S}, \tag{6.5}$$

where $g_I = 5.258$ [94] and $B_v = 0.342488$ cm^{-1} [61]. To first order, the mixing between $|m_S = \pm 1/2>$ in the HFS due to the hyperfine interaction alone can be estimated using the perturbation theory:

$$
\begin{aligned}
|\mathrm{HFS}\rangle &\approx |m_N, m_S = -1/2, m_I = 1/2\rangle + \frac{b}{2\mu_B \times B}\,|m_N, m_S = 1/2, m_I = -1/2\rangle \\
&= |m_N, m_S = -1/2, m_I = 1/2\rangle + 10^{-2}\,|m_N, m_S = 1/2, m_I = -1/2\rangle \qquad (6.6)
\end{aligned}
$$

where the mixing coefficient is estimated at $B = 0.35$ T, corresponding to a ratio of $\frac{P_{HFS}}{P_{LFS}} \approx 10^{-4}$ for decaying to the HFS state due to the hyperfine interaction.

The Zeeman levels obtained by diagonalizing the Hamiltonian in the fully coupled basis sets ($|N, S, J, F, m_F\rangle$) are shown in Fig. 6.3.

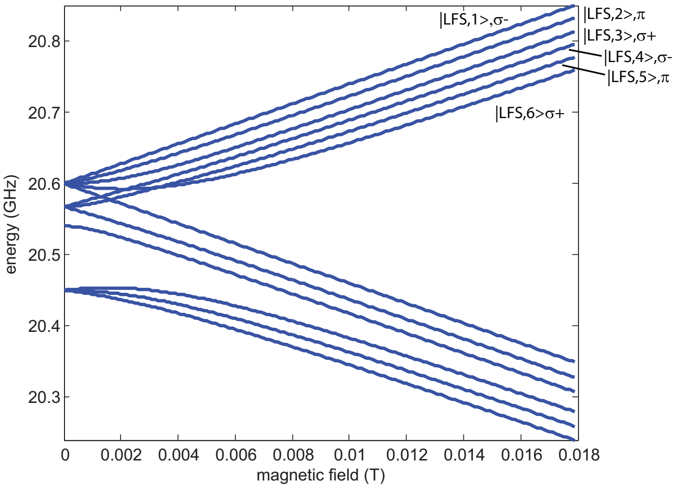

Figure 6.3: Calculated Zeeman level of CaF $X^2\Sigma^+(N = 1)$ based on Eq. 6.5. The basis states are $|N, S, J, F, m_F\rangle$. Here, we assign the six LFS states to $|\mathrm{LFS,1}\rangle - |\mathrm{LFS,6}\rangle$ in order of decreasing energies.

To get a sense of the laser polarizations needed for exciting the LFS, we can express the eigenvectors in the decoupled basis sets, $|m_N, m_S, m_I>$. At $B = 0.35$ T, the six LFS states obtained from diagonalizing $H = \gamma\vec{N}\cdot\vec{S} + g_S\mu_B B_Z T^1_{p=0}(\vec{S}) + b_F\vec{I}\cdot\vec{S}$ in the decoupled basis sets are

$$\begin{aligned}
|\text{LFS,1}(m_F = 2)\rangle &= |1, 1/2, 1/2\rangle \\
|\text{LFS,2}(m_F = 1)\rangle &= 0.0042\,|1, 1/2, -1/2\rangle + 0.0029\,|1, -1/2, 1/2\rangle + |0, 1/2, 1/2\rangle \\
|\text{LFS,3}(m_F = 0)\rangle &= 0.0043\,|0, 1/2, -1/2\rangle + 0.0029\,|0, -1/2, 1/2\rangle + |-1, 1/2, 1/2\rangle \\
|\text{LFS,4}(m_F = 1)\rangle &= |1, 1/2, -1/2\rangle + 0.0062\,|1, -1/2, 1/2\rangle - 0.0043\,|0, 1/2, 1/2\rangle \\
|\text{LFS,5}(m_F = 0)\rangle &= 0.0029\,|1, -1/2, -1/2\rangle + |0, 1/2, -1/2\rangle + 0.0063\,|0, -1/2, 1/2\rangle \\
&- 0.0043\,|-1, 1/2, 1/2\rangle \\
|\text{LFS,6}(m_F = -1)\rangle &= 0.0029\,|0, -1/2, -1/2\rangle + |-1, 1/2, -1/2\rangle + 0.0063\,|-1, -1/2, 1/2\rangle
\end{aligned} \tag{6.7}$$

Here, the eigenvectors are arranged in order of decreasing energies. The mixing coefficient between $|m_S = \pm 1/2\rangle$ is consistent with the estimation from the perturbation theory. The polarizations that excite $|\text{LFS,1}\rangle - |\text{LFS,3}\rangle$ are σ_-, π, and σ_+ and denoted in Fig. 6.3.

6.2.3 Scattering multiple photons and laser cooling of CaF

Since we do not need to worry about decaying to the HFS states at fields $B >$ 0.35 T, the leakage into the dark vibrational state is going to limit the number of scattered photons to be 1000. After we loaded the molecules, we found that we could optically pump the molecules away in the detection process (See Fig. 3.13(b)). The detection beam has a diameter of ≈ 2 mm and is sent into the radial direction of the quadrupole trap. In this configuration, most of the molecules are excited via σ_+ and σ_- polarizations, where the magnetic field direction is mostly pointing along the radial direction. Only a small portion of molecules moving close to the trap center can be excited via π polarization, where the field direction is not well defined. From Fig. 6.2, we learn that one out of the three low-field seeking states has to be excited via the π polarization. This means there's one dark state during the detection process. Molecules landing in this state still remain trapped. This statement is still valid even if we include the hyperfine interactions, where two out of the six low-field seeking states need to be addressed via the π polarization, as shown in Eq. 6.7.

These dark states may be remixed by using another laser beam with a larger diameter along the radial direction, which can interrogate more molecules near the trap center. The clearance of the holes on the magnet bobbin is 1.19 cm, which sets the size of the remixing beam along the radial direction. The frequency of remixing beam should be resonant with molecules near the trap center. Fig. 6.4 shows the field direction of our quadurpole trap, where the z axis is along the magnet bore. Molecules at $|Z| > 0$ and within the diameter of the remixing beam would be excited via the π polarization. During the remixing process, the multichannel scaler can be switched off to prevent the scattered photons overwhelming the background count rate. It can be switched back on when we need to detect the trapped molecules.

For the $X - B$ transition of CaF, the trapped spectrum with a width of 140 MHz is centered at 100 MHz bluer than the zero field frequency due to the magnetic field (See Fig. 3.11). The radius of initial trapped cloud is 2.5 cm according to the trajectory simulation. If we want to laser cool the entire molecular cloud, we could use a cooling laser with a frequency that is blue detuned relative to the zero field value but slightly red detuned relative to the most energetic molecules near trap edge. To

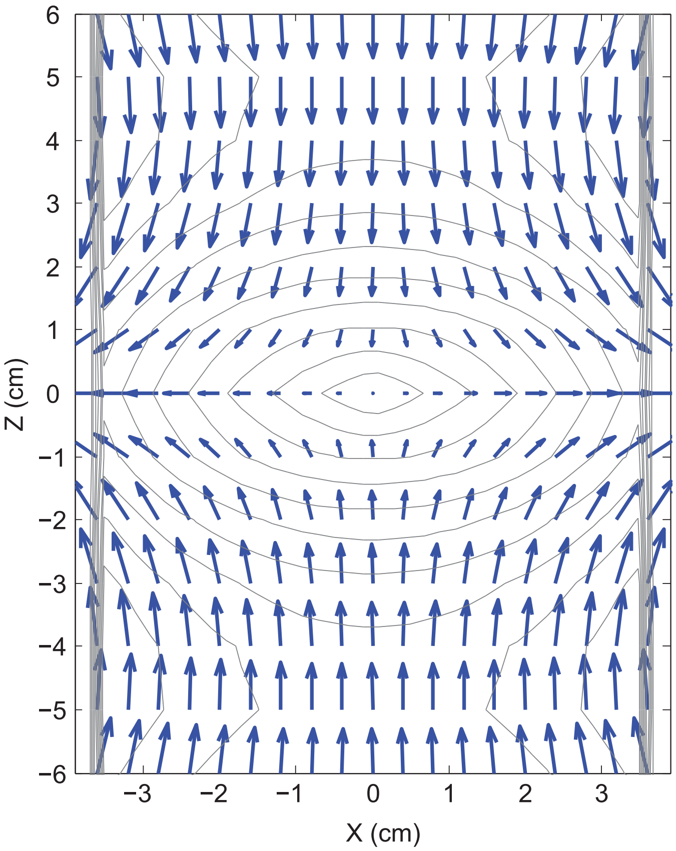

Figure 6.4: Magnetic field profile and direction of the quadrupole trap used in our experiment. The cask of our quadrupole trap has an inner radius (in X direction) and length (along Z direction) of 3.91 cm and 28.96 cm, respectively.

avoid heating the colder molecules orbiting near the trap center, we will need to send a donut-shaped cooling laser along the magnet bore which physically addresses the molecules reaching high fields. The frequency of cooling laser can be swept down from the blue side of the trapped spectrum down to the zero field value. The shape of the laser should transform from a donut shape to a round gaussian beam simultaneously. Using a large diameter and linear polarized laser beam along the magnet bore has the advantage of addressing molecules in all of the hyperfine states. For example, molecules moving close to $Z = 0$ and on the $X - Y$ plane can be excited via the π

polarization; molecules moving near $X = 0$ (or the central axis of the magnet) can be addressed via the σ_+ and σ_- polarizations.

The velocity change due to 1000 photon kicks is 12.7 m/s for CaF using the 531 nm laser. Given that the capture velocity of CaF ($N = 1$) is roughly 30 m/s, we can can estimate the reduction of the kinetic energy to be 67% via 1000 photons.

6.2.4 Prospects of Sisyphus cooling of CaF in the trap

Sisyphus cooling relies on repetitively converting the kinetic energy of the species of interest to the potential energy. Optical pumping is employed in each cooling cycle so that the scattering photons carry away the entropy and render the process irreversible. It has been employed to reduce the temperature of electrically trapped CH_3F molecules by a factor of 13.5 [95]. Since we could scatter up to 1000 photons within the LFS manifold of CaF ($v = 0, N = 1$), we may be able to use Sisyphus cooling to lower the temperature of our trapped molecules as well.

The key idea of Sisyphus cooling is the slopes of the six low-field seeking states are not exactly the same in the trap. If the molecules can preferentially climb up one steeper potential hill to the trap edge and then roll back down to the trap center along another shallower potential, we can remove some of the kinetic energy in each round trip.

Fig. 6.3 shows the Zeeman levels of the six low-field seeking states at low fields, which indicates $|LFS, 1\rangle$ has the steepest slope. However, the situation changes at larger fields. Fig. 6.5 shows the energy difference between the first three low-field seeking states. At $B < B_1 = 0.03$ T, $|m_F = 2\rangle$ has the steepest slope. However,

$|m_F = 2\rangle$ is less steep than $|m_F = 1\rangle$ and $|m_F = 0\rangle$ at B > B1, corresponding to a decreasing energy difference versus field.

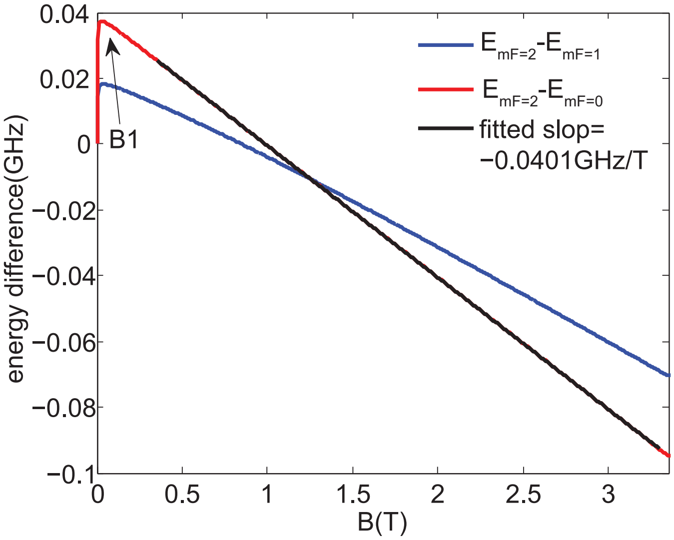

Figure 6.5: Energy difference between the first three LFS states, $|m_F = 2>$, $|m_F = 1>$, and $|m_F = 0>$ of CaF ($N = 1$). $B_1 = 0.03$ T in the graph; The slope of the $E_{m_F=2} - E_{m_F=0}$ is -0.0401 GHz/T.

Based on Fig. 6.5, we should be able to perform Sisyphus cooling using the different slopes of the $|m_F = 2\rangle$ and $|m_F = 0\rangle$ states. Fig. 6.6 shows the schematic of Sisyphus cooling. We can let the molecules roll up to the trap edge along $|m_F = 0\rangle$, which has a steeper slope than $|m_F = 2\rangle$. We optically pump the molecules at high fields to $|m_F = 2\rangle$ and let them roll back down to the trap center along the shallower slope of $|m_F = 2\rangle$. To complete one cooling cycle, we optically pump the molecules back to $|m_F = 0\rangle$ at low fields $B > B_{min}$, where we can scatter multiple photons (e.g. $B_{min} = 0.35$ T). The first pumping laser f_1 of the Sisyphus cooling, which addresses the $|m_F = 0\rangle$ at high fields, should be σ_+ polarized. If we send one circular polarized laser into a quadrupole trap, the molecules see σ_+ polarization on one side of the trap and σ_- polarization on the other side. The chance of pumping

$|m_F = 2\rangle$ at high fields via f_1 on the other side of the trap depends on the laser detuning in the fields. According to Fig. 6.5, $|m_F = 2\rangle$ and $|m_F = 0\rangle$ are degenerate at B$_{deg}$ = 1 T. To first order, we should be able to perform Sisyphus cooling between B$_{max}$=3.3 T and B$_{deg}$ = 1 T. Experimentally, we can send a blue detuned σ_+ polarized laser (f_1=f_0+$\Delta g(m_F = 0 \to m'_F) \times B_{max}$) to pump $|m_F = 0\rangle$ starting from B_{max} = 3.3 T. Here, the blue detuned frequency is relative to zero field value f_0 since $\Delta g(m_F = 0 \to m'_F) > 0$ based on the obtained trapped spectrum. The $|m_F = 2\rangle$ state will not be affected since it has lower energies than $|m_F = 0\rangle$ when $B > B_{dge} = 1$ T. A second less blue detuned, σ_- polarized laser (f_2) can be used to pump $|m_F = 2\rangle$ at B_{deg} = 1 T. To avoid accumulating the molecules to the dark state, $|m_F = 1\rangle$, we only need to make sure that 2nd pumping beam has a large diameter so that the $|m_F = 1\rangle$ state can be addressed when the polarization direction of 2nd pumping laser is parallel to the magnetic field.

We would like to know the amount of cooling we could obtain. After the Nth cooling cycle, the largest magnetic field the molecules can reach, $B(N + 1)$, is given by

$$\begin{aligned} \mu_B \times B(N+1) &= \mu_B \times B(N) - h\Delta S(B(N) - B_{deg}) \\ \frac{\mu_B \times \delta B}{\delta N} &= -h\Delta S \times (B(N) - B_{deg}) \end{aligned} \tag{6.8}$$

where ΔS is the slope of the frequency difference between two LFS states involved in the Sisyphus cooling, as shown in Fig. 6.5. B_{deg}= 1 T is where we repump the

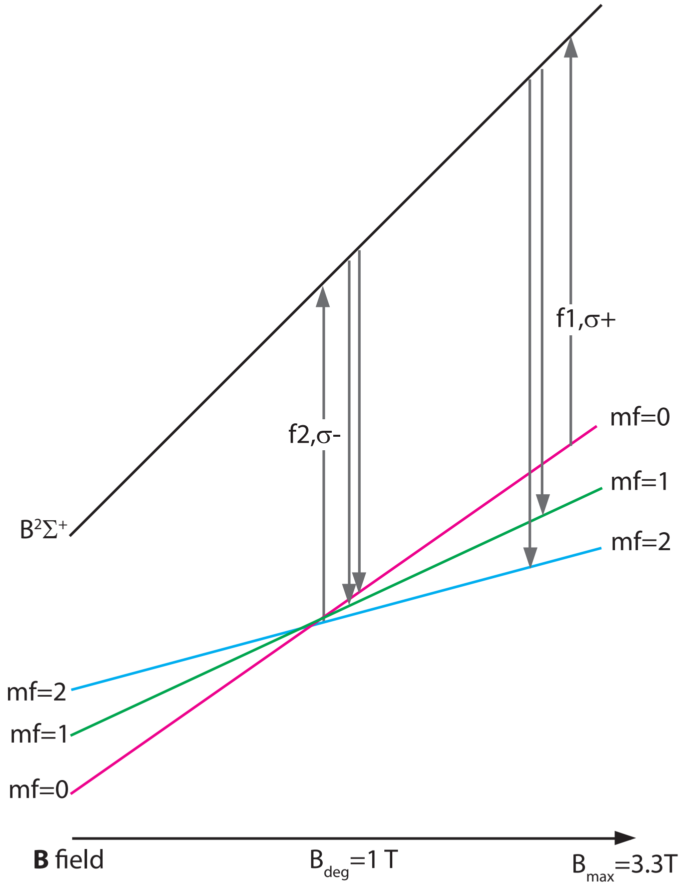

Figure 6.6: Schematic for performing Sisyphus cooling between B_{max} and $B_{deg} = 1$ T, where $|m_F = 2>$ and $|m_F = 0>$ are degenerate.

molecules. We can integrate Eqn. 6.8

$$\begin{aligned}\int \frac{\mu_B \times \delta B}{B - B_{deg}} &= -h\Delta S \int \delta N \\ \rightarrow \frac{B_f - B_{deg}}{B_i - B_{deg}} &= e^{-h\Delta SN/\mu_B} = 0.057\end{aligned} \tag{6.9}$$

Here, we take the slope to be $\Delta S = 0.0401$ GHz/T and number of cycling to be $N = 1000$. Assuming $B_i = 3.3$ T is the initial field of the molecules and $B_{deg} = 1$ T, we obtain the field of the molecules after cooling to be $B_f = 1.13$ T. This corresponds to a reduction of kinetic energy of 66%.

6.3 Prospect of laser cooling Li in the trap

To evaluate the possibility of laser cooling of Li in our deep quadrupole trap, where the field gradient is ~ 1 T/cm, we will need to calculate the Zeeman levels of Li. Fig. 6.7 plots the Zeeman levels of ^{7}Li in ^{2}P state. The Hamiltonian we use is

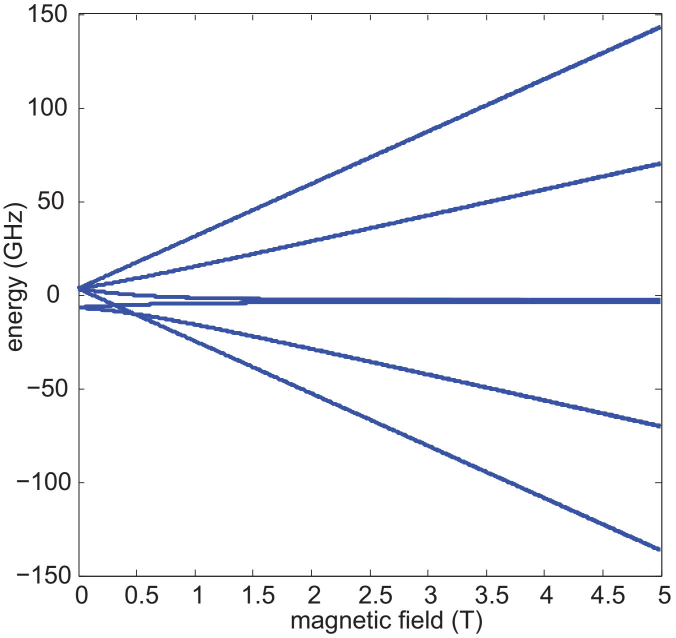

Figure 6.7: Calculated Zeeman levels of ^{7}Li in ^{2}P state.

$$\begin{aligned} H = & \\ & f\vec{L}\cdot\vec{S} - \vec{\mu}_S \cdot B - \vec{\mu}_L \cdot B - \vec{\mu}_I \cdot B + \\ & A\vec{I}\cdot\vec{J} + \frac{B}{2I(2I-1)(2J)(2J-1)}[3(\vec{I}\cdot\vec{J})(2\vec{I}\cdot\vec{J}+1) - 2I(I+1)J(J+1)], \end{aligned} \tag{6.10}$$

where $f = 6.7$ GHz. The hyperfine constant for $J = 1/2$ is $A = 46$ MHz; for $J = 3/2$, $A = -3.08$ MHz and $B = 0.04$ MHz [96–98].

For simplicity, let's ignore the hyperfine interaction and express the eigenstates in $|m'_L, m'_S\rangle$ basis. At $B = 5$ T, the eigenstates arranged in decreasing energies are

$$\begin{aligned}
|m'_J = 3/2\rangle &= |1, 1/2\rangle \\
|m'_J = 1/2\rangle &= 0.9979\,|0, 1/2\rangle + 0.064\,|1, -1/2\rangle \\
|m'_J = -1/2\rangle &= 0.9975\,|-1, 1/2\rangle + 0.071\,|0, -1/2\rangle \\
|m'_J = 1/2\rangle &= 0.0641\,|0, 1/2\rangle + 0.9979\,|1, -1/2\rangle \\
|m'_J = -1/2\rangle &= 0.0706\,|-1, 1/2\rangle + 0.9975\,|0, -1/2\rangle \\
|m'_J = -3/2\rangle &= |-1, -1/2\rangle
\end{aligned} \tag{6.11}$$

The low-field seeking state $|m'_J = 1/2\rangle$ has a similar g factor to the Li in the ground state $|m_J = 1/2\rangle$, and chance of decaying to the high-field state after spontaneous emission is $\propto (0.06)^2 \sim 10^{-3}$.

However, the mixing between the low-field seeking and high-field seeking states becomes more prominent at lower fields. At $B = 2$ T, the eigenstates become

$$\begin{aligned}
|m'_J = 3/2\rangle &= |1, 1/2\rangle \\
|m'_J = 1/2\rangle &= 0.9892\,|0, 1/2\rangle + 0.1467\,|1, -1/2\rangle \\
|m'_J = -1/2\rangle &= 0.9831\,|-1, 1/2\rangle + 0.1832\,|0, -1/2\rangle \\
|m'_J = 1/2\rangle &= 0.1467\,|0, 1/2\rangle + 0.9892\,|1, -1/2\rangle \\
|m'_J = -1/2\rangle &= 0.1832\,|-1, 1/2\rangle + 0.9831\,|0, -1/2\rangle \\
|m'_J = -3/2\rangle &= |-1, -1/2\rangle
\end{aligned} \tag{6.12}$$

The number of photons we can cycle between $|m_J = 1/2\rangle \rightarrow |m'_J = 1/2\rangle$ is down to $\sim$

100. The other possibility is to utilize the other transition $|m_J = 1/2\rangle \rightarrow |m'_J = 3/2\rangle$, which is a closed cycling transition. However, the energy difference of these two states has a slope of 14 GHz/T. At any given laser detuning, only a small fraction of atoms would be resonant with the cooling laser. The laser cooling efficiency for Li would be less than CaF ($N = 1$).

6.4 Optical loading of triatomic molecules

Cooling diatomic molecules is certainly more challenging than atoms. However, more interesting physics reveals at lower temperatures due to the advance of the new cooling and trapping techniques. Cold diatomic molecules provide a rich system for studying cold controlled chemistry, search for variation of fundamental constants and physics beyond the standard model, and novel quantum physics, as discussed in Ch. 1. Since the optical loading technique demonstrated here only relies on scattering two photons, it could be extended to even more complex molecules with more vibrational degrees of freedom than diatomic molecules, which makes laser cooling infeasible.

Polyatomic molecules have been discovered in interstellar clouds [1], including prebiotic molecules (e.g. $HCOOCH_3$) [99]. Their rich internal states could be used in quantum computation [100] and provide another platform for determining the variation of fundamental constants [101]. The cold He-polyatomic molecule collisions are an active research area [1, 99] to extract the rotational cross sections for understanding the internal distributions of polyatomic molecules in the interstellar cloud. In addition, a rigorous quantum mechanical theory is employed in Ref. [102, 103] to study cold collisions between triatomic molecules with He atoms in the magnetic trap. One particular collision system–He-CH_2–shows interesting collisional properties [102]. Depending on the relative orientations of the nuclear spins of H atoms, the inelastic collision cross sections of ortho-CH_2 and para-CH_2 can differ by orders of magnitudes. This may find applications in separating isomers. It is also found that several triatomic species have a favorable collisional properties with He.

The trapped polyatomic molecules, including CH_3F, CH_3Cl, CH_2O, NH_3, ND_3 [23, 95, 104, 105], realized in the laboratories so far are produced either from Stark decelerators or electrically filtering of gas-phase molecules using guides. These slow molecules are then loaded into electric traps. The optical loading method we developed could extend trapping to magnetic, polyatomic molecules.

One example for demonstrating optical loading could be CaOH. The electronic structure of the triatomic molecule CaOH is similar to CaF [106, 107]. It was experimentally determined that $\tilde{X}^2\Sigma^+$, $\tilde{A}^2\Pi$ and $\tilde{B}^2\Sigma^+$ states of CaOH, all relevant to the proposed optical pumping procedure, have a linear geometry in the lowest vibrational mode [107]. Since the rotational constant for CaOH ($B_0 \approx 0.33$ cm^{-1} [107]) is comparable to that of CaF, there should be no avoided crossing for CaOH $X^2\Sigma^+(N = 1)$ up to 3.6 T. Here, we consider the anisotropic hyperfine interaction as a dominant coupling mechanism, which leads to the avoided crossings between equal parity rotational levels [108] as in CaF. There are other triatomic molecules with similar electric structures to CaF, which are also suitable for our loading technique. For example, SrOH has a linear geometry, an unpaired electron in the ground state, sizable rotational constant of $B_0 \sim 0.25$ cm^{-1} [107, 109], and was previously detected in cold molecular beams [110]. These triatomic molecules could be accumulated in a magnetic trap for the first time using the current scheme, with the scattering of only a few photons.

6.5 Slower beam for large molecules

The only hurdle we can envision to optically load large molecules with small rotational constants lies on a low trap depth arising from the avoided crossings. A lower trap depth means a reduced capture velocity and calls for methods to deliver an even slower molecular beam. There are two potential ways to produce a slower beam. One approach is to continue engineering the two-stage cell design. Developing the current two-stage source has reduced the molecular velocity by nearly 100 m/s, compared to the single-stage source, enabling the direct trap loading of CaF. The other approach we could take is to combine a few electromagnetic slowing stages with the current two-stage buffer-gas beam.

Based on the CaH beam work described in Sec. 2.3, we have delivered a near effusive beam simply by using a mesh geometry to engineer the He-molecule collisions inside the slowing cell and in the beam. The peak forward velocity of CaH molecules using a fine mesh is reduced by 15 m/s compared to the coarse mesh. Using such a cell geometry would be advantageous for large molecules since the beam velocity approaches the thermal velocity of the heavy molecules. Although laser ablation has been used so far to produce CaH and CaF molecules, other ways to introduce the species of interest into the buffer-gas cell, such as an oven source and injection of gas-phase molecules [37], have been employed in our group. A near effusive beam would benefit from a colder initial molecular temperature, which is found to be difficult using laser ablation due to a large amount of energy introduced.

The maximum energy per stage that can be removed in a magnetic or electric decelerator is $\mu \cdot B$ or $D \cdot E$ respectively, corresponding to an energy of ~ 1 K. This means that hundreds of stages are typically needed in order to decelerate the fast molecules in supersonic beams, while only a few stages can provide significant deceleration at our beam's modest velocity of $v_f \sim 60$ m/s, which corresponds to 9 K in energy for CaH and 13 K for CaF. The decelerators we envision to use are *moving trap* type decelerators [111, 112], which not only slow down the longitudinal velocity of species but provide a transverse confinement. This is crucial for retaining the flux of slow molecules before trap loading. Therefore, these moving trap decelerators show high stability even at low velocities.

6.6 Kinetic cooling of large molecules

Since the technology of producing atoms at a temperature of ~ 10 μK in a magneto-optical trap (MOT) is mature, it has been proposed to employ these cold atoms to stop fast molecules from supersonic beams [113]. After one elastic collision event, the probability F of reducing the kinetic energy of the molecule from E_M to E'_M is given by [113]

$$F = \frac{1}{2}\{[\frac{E'_M}{E_M} - \frac{m_M^2 + m_A^2}{(m_M + m_A)^2}]/[2\mu_{M,A}]/(m_M + m_A) + 1\}, \tag{6.13}$$

where m_M, m_A, and $\mu_{M,A}$ are the molecular mass, atomic mass, and the reduced mass. The atoms are assumed to be stationary initially. If the molecular mass is equal to the atomic mass, Eq. 6.13 is reduced to a simple relation $F = E'_M/E_M$. More specifically, if we want to reduce the kinetic energy of the slow molecule from $E_M = 1$

K down to $E'_M = 10$ mK, the chance is 10^{-2} after each elastic collision. According to Eq. 6.13, we can estimate the possibility of reducing the molecular energy to 10 mK if the molecular mass differs the atomic mass by 15%, yielding $F = 5.2 \times 10^{-3}$ for $m_M = 1.15 \times m_A$ and $F = 3.4 \times 10^{-3}$ for $m_M = 0.85 \times m_A$.

Using a two-stage buffer-gas beam, direct magneto-optical trap loading has recently been accomplished for a number of atomic species with complex level structure, including Yb, Tm, Er and Ho [92]. The reported Yb number is 4×10^8. If we assume the diameter of the Yb atoms to be 3 mm, we obtain a density of 2.8×10^{10} cm^{-3}. The mean free path of the molecules passing through of the Yb atoms is 3.5×10^3 cm if we assume the elastic cross section is 10^{-14} cm^{-2}. For each molecule passing through the Yb cloud, there is a probability of 10^{-4} to encounter one elastic collision.

Due to the small chance of receiving one elastic collision, the molecular beam suitable for this type of loading should be in continuous mode. These type of beams have been realized for benzonitrile (C_7H_5N), fluorobenzene (C_6H_5F), and anisole (C_7H_8O) [114] by injecting these gas-phase molecules into a cell at 4.7 K. The molecular beam from such a single-stage cell has a peak forward velocity of 67 m/s (~ 27 K kinetic energy) and a flux of 10^{15} molecules/s. If we assume the lifetime of the Yb MOT is 100 ms, we should be able to produce $\sim 10^4$ large molecules at a temperature of 270 mK if the MOT is located 30 cm away from the beam cell. Note that we assume the mass of the big molecule is similar to Yb and assume the transverse temperature of the beam is the same as the cell temperature. The loaded number can be improved if the MOT number can be increased. The forward velocity of beam can be reduced if the the cell is colder and the two-stage cell is employed. After lowering the temperature of the molecules further down to 10 mK, it may be possible to trap the molecules in their absolute ground state.

Bibliography

[1] Evelyne Roueff and François Lique, Chemical reviews (2013).

[2] Eric Herbst, Chemical Society Reviews **30**, 168 (2001).

[3] David Edvardsson, Christopher F. Williams, and David C. Clary, Chemical Physics Letters **431**, 261 (2006).

[4] Terry J. Frankcombe and Gunnar Nyman, Journal of Physical Chemistry A **111**, 13163 (2007).

[5] D. R. Flower, Physics Reports **174**, 1 (1989).

[6] R. V. Krems, Phys. Chem. Chem. Phys. **10**, 4079 (2008).

[7] M. T. Hummon, T. V. Tscherbul, J. Kłos, H.-I Lu, E. Tsikata, W. C. Campbell, A. Dalgarno, and J. M. Doyle, Phys. Rev. Lett. **106**, 053201 (2011).

[8] J. J. Hudson, D. M. Kara, I. J. Smallman, B. E. Sauer, M. R. Tarbutt, and E. A. Hinds, Nature **473**, 493 (2011).

[9] A. C. Vutha, W. C. Campbell, Y. V. Gurevich, N. R. Hutzler, M. Parsons, D. Patterson, E. Petrik, B. Spaun, J. M. Doyle, G. Gabrielse, and D. DeMille, J. Phys. B **43**, 074007 (2010).

[10] Eric R. Hudson, H. J. Lewandowski, Brian C. Sawyer, and Jun Ye, Phys. Rev. Lett. **96**, 143004 (2006).

[11] S. Truppe, R. J. Hendricks, S. K. Tokunaga, H. J. Lewandowski, M. G. Kozlov, Christian Henkel, E. A. Hinds, and M. R. Tarbutt, Nature communications **4**, 2600 (2013).

[12] S. Ospelkaus, K.-K. Ni, D. Wang, M. H. G. de Miranda, B. Neyenhuis, G. Quéméner, P. S. Julienne, J. L. Bohn, D. S. Jin, and J. Ye, Science **327**, 853 (2010).

[13] K.-K. Ni, S. Ospelkaus, D. Wang, G. Quéméner, B. Neyenhuis, M. H. G. de Miranda, J. L. Bohn, J. Ye, and D. S. Jin, Nature **464**, 1324 (2010).

[14] M. H. G. de Miranda, A. Chotia, B. Neyenhuis, D. Wang, G. Quéméner, S. Ospelkaus, J. L. Bohn, J. Ye, and D. S. Jin, Nature Phys. **7**, 502 (2011).

[15] Bo Yan, Steven A. Moses, Bryce Gadway, Jacob P. Covey, Kaden R. A. Hazzard, Ana Maria Rey, Deborah S. Jin, and Jun Ye, Nature **501**, 521 (2013).

[16] A. Micheli, G. K. Brennen, and P. Zoller, Nature Physics **2**, 341 (2006).

[17] H. P. Büchler, E. Demler, M. Lukin, A. Micheli, N. Prokof'ev, G. Pupillo, and P. Zoller, Phys. Rev. Lett. **98**, 060404 (2007).

[18] A. Micheli, G. Pupillo, H. P. Büchler, and P. Zoller, Phys. Rev. A **76**, 043604 (2007).

[19] Mikhail Lemeshko, Roman V. Krems, and Hendrik Weimer, Phys. Rev. Lett. **109**, 035301 (2012).

[20] Lincoln D. Carr, David DeMille, Roman V. Krems, and Jun Ye, New Journal of Physics **11**, 055049 (2009).

[21] Bretislav Friedrich and John M. Doyle, ChemPhysChem **10**, 604 (2009).

[22] Melanie Schnell and Gerard Meijer, Angew. Chem. Int. Ed. **48**, 6010 (2009).

[23] Mikhail Lemeshko, Roman V. Krems, John M. Doyle, and Sabre Kais, Molecular Physics **111**, 1648 (2013).

[24] Andrew Kerman, Jeremy Sage, Sunil Sainis, Thomas Bergeman, and David DeMille, Phys. Rev. Lett. **92**, 033004 (2004).

[25] Kevin Jones, Eite Tiesinga, Paul Lett, and Paul Julienne, Reviews of Modern Physics **78**, 483 (2006).

[26] K.-K. Ni, S. Ospelkaus, M. H. G. de Miranda, A. Pe′er, B. Neyenhuis, J. J. Zirbel, S. Kotochigova, P. S. Julienne, D. S. Jin, and J. Ye, Science **322**, 231 (2008).

[27] Cheng Chin, Rudolf Grimm, Paul Julienne, and Eite Tiesinga, Reviews of Modern Physics **82**, 1225 (2010).

[28] Coralie Berteloite, Manuel Lara, Astrid Bergeat, Sébastien D. Le Picard, Fabrice Dayou, Kevin M. Hickson, André Canosa, Christian Naulin, Jean-Michel Launay, Ian R. Sims, and Michel Costes, Physical Review Letters **105**, 203201 (2010).

[29] A. B. Henson, S. Gersten, Y. Shagam, J. Narevicius, and E. Narevicius, Science **338**, 234 (2012).

[30] Hendrick L. Bethlem, Floris M. H. Crompvoets, Rienk T. Jongma, Sebastiaan Y. T. van de Meerakker, and Gerard Meijer, Phys. Rev. A **65**, 053416 (2002).

[31] Sebastiaan Y. T. van de Meerakker, Paul H. M. Smeets, Nicolas Vanhaecke, Rienk T. Jongma, and Gerard Meijer, Phys. Rev. Lett. **94**, 023004 (2005).

[32] Steven Hoekstra, Markus Metsälä, Peter C. Zieger, Ludwig Scharfenberg, Joop J. Gilijamse, Gerard Meijer, and Sebastiaan Y. T. van de Meerakker, Phys. Rev. A **76**, 063408 (2007).

[33] Takamasa Momose, Yang Liu, Sida Zhou, Pavle Djuricanin, and David Carty, Phys. Chem. Chem. Phys. **15**, 1772 (2013).

[34] Edvardas Narevicius, Adam Libson, Christian Parthey, Isaac Chavez, Julia Narevicius, Uzi Even, and Mark Raizen, Phys. Rev. A **77**, 051401 (2008).

[35] R. Fulton, A. I. Bishop, M. N. Shneider, and P. F. Barker, Nature Physics **2**, 465 (2006).

[36] W. C. Campbell and J. M. Doyle, in *Cold molecules: theory, experiment, applications*, edited by Roman V. Krems, W. C. Stwalley, and B. Friedrich (CRC Press, ADDRESS, 2009), Chap. 13, pp. 473–508.

[37] David Patterson and John M. Doyle, Molecular Physic **110**, 1757 (2012).

[38] D. Egorov, W. C. Campbell, B. Friedrich, S. E. Maxwell, E. Tsikata, L. D. Buuren, and J. M. Doyle, The European Physical Journal D **31**, 307 (2004).

[39] N. R. Hutzler, M. F. Parsons, Y. V. Gurevich, P. W. Hess, E. Petrik, B. Spaun, A. C. Vutha, D. DeMille, G. Gabrielse, and J. M. Doyle, Phys. Chem. Chem. Phys. **13**, 18976 (2011).

[40] Jonathan D. Weinstein, Robert deCarvalho, Karine Amar, Andreea Boca, Brian C. Odom, Bretislav Friedrich, and John M. Doyle, The Journal of Chemical Physics **109**, 2656 (1998).

[41] Wesley C. Campbell, Edem Tsikata, Hsin-I Lu, Laurens D. van Buuren, and John M. Doyle, Phys. Rev. Lett. **98**, 213001 (2007).

[42] Michael Stoll, Joost Bakker, Timothy Steimle, Gerard Meijer, and Achim Peters, Phys. Rev. A **78**, 032707 (2008).

[43] Cindy I. Hancox, S. Charles Doret, Matthew T. Hummon, Linjiao Luo, and John M. Doyle, Nature **431**, 281 (2004).

[44] David Patterson and John M. Doyle, The Journal of chemical physics **126**, 154307 (2007).

[45] J. F. Barry, E. S. Shuman, and D. DeMille, Phys. Chem. Chem. Phys. **13**, 18936 (2011).

[46] E. S. Shuman, J. F. Barry, D. R. Glenn, and D. DeMille, Phys. Rev. Lett. **103**, 223001 (2009).

[47] E. S. Shuman, J. F. Barry, and D. Demille, Nature **467**, 820 (2010).

[48] J. F. Barry, E. S. Shuman, E. B. Norrgard, and D. Demille, Phys. Rev. Lett. **108**, 103002 (2012).

[49] Matthew T. Hummon, Mark Yeo, Benjamin K. Stuhl, Alejandra L. Collopy, Yong Xia, and Jun Ye, Phys. Rev. Lett. **110**, 143001 (2013).

[50] Benjamin K. Stuhl, Matthew T. Hummon, Mark Yeo, Goulven Quéméner, John L. Bohn, and Jun Ye, Nature **492**, 396 (2012).

[51] E. Tsikata, W. C. Campbell, M. T. Hummon, H.-I Lu, and J. M. Doyle, New J. Phys. **12**, 065028 (2010).

[52] Eric A. Cornell, Chris Monroe, and Carl E. Wieman, Physical Review Letters **67**, 2439 (1991).

[53] Markus Falkenau, Valentin V. Volchkov, Jahn Rührig, Axel Griesmaier, and Tilman Pfau, Phys. Rev. Lett. **106**, 163002 (2011).

[54] A. Ostendorf, C. Zhang, M. A. Wilson, D. Offenberg, B. Roth, and S. Schiller, Physical Review Letters **97**, 243005 (2006).

[55] Wade G. Rellergert, Scott T. Sullivan, Steven J. Schowalter, Svetlana Kotochigova, Kuang Chen, and Eric R. Hudson, Nature **495**, 490 (2013).

[56] Nicholas R. Hutzler, Hsin-I Lu, and John M. Doyle, Chemical reviews **112**, 4803 (2012).

[57] Joop J. Gilijamse, Steven Hoekstra, Samuel A. Meek, Markus Metsälä, Sebastiaan Y. T. van de Meerakker, Gerard Meijer, and Gerrit C. Groenenboom, The Journal of Chemical Physics **127**, 221102 (2007).

[58] S. E. Maxwell, N. Brahms, R. deCarvalho, D. R. Glenn, J. S. Helton, S. V. Nguyen, D. Patterson, J. Petricka, D. DeMille, and J. M. Doyle, Physical Review Letters **95**, 173201 (2005).

[59] Hsin-I Lu, Julia Rasmussen, Matthew J. Wright, Dave Patterson, and John M. Doyle, Physical chemistry chemical physics : PCCP **13**, 18986 (2011).

[60] R. W. Field, Daivd O. Harris, and Takehiko Tanaka, Journal of molecular spectroscopy **57**, 107 (1975).

[61] M. Dulick, Peter F. Bernath, and Robert W. Field, Can. J. Phys. **58**, 703 (1980).

[62] Dimitri Michael Egorov, Ph.D. thesis, Harvard University, 2004.

[63] Wesley C. Campbell, Ph.D. thesis, Harvard University, 2008.

[64] Robert C. Hilborn, American Journal of Physics **50**, 982 (1982).

[65] Jinha Kim, Ph.D. thesis, Harvard University, 1997.

[66] Robert Michniak, Ph.D. thesis, Harvard University, 2004.

[67] S. Charles Doret, Colin B. Connolly, Wolfgang Ketterle, and John M. Doyle, Phys. Rev. Lett. **103**, 103005 (2009).

[68] J. Riedel, S. Hoekstra, W. Jäger, J. J. Gilijamse, S. Y. T. Meerakker, and G. Meijer, The European Physical Journal D **65**, 161 (2011).

[69] Jonathan David Weinstein, Ph.D. thesis, Harvard University, 2002.

[70] L. A. Kaledin, J. C. Bloch, M. C. McCarthy, and R. W. Field, Journal of molecular spectroscopy **197**, 289 (1999).

[71] G. Herzberg, *Molecular Spectra and Molecular Structure: Spectra of Diatomic Molecules , 2nd ed.* (Krieger, ADDRESS, 1989).

[72] John Brown and Alan Carrington, in *Rotational Spectroscopy of Diatomic Molecules* (Cambridge University Press, ADDRESS, 2003).

[73] R. V. Krems, D. Egorov, J. S. Helton, K. Maussang, S. V. Nguyen, and J. M. Doyle, The Journal of chemical physics **121**, 11639 (2004).

[74] W. J. Childs, G. L. Goodman, and L. S. Goodman, Journal of Molecular Spectroscopy **86**, 365 (1981).

[75] Amar C. Vutha, European Journal of Physics **31**, 389 (2010).

[76] K. Maussang, D. Egorov, J. S. Helton, S. V. Nguyen, and J. M. Doyle, Phys. Rev. Lett. **94**, 123002 (2005).

[77] T. C. Steimle, Jamie Gengler, and Jinhai Chen, Can. J. Chem. **82**, 779 (2004).

[78] R. R. Chaustowski, V. Y. F. Leung, and K. G. H. Baldwin, Appl. Phys. B **86**, 491 (2007).

[79] J. G. E. Harris, R. A. Michniak, S. V. Nguyen, W. C. Campbell, D. Egorov, S. E. Maxwell, L. D. van Buuren, and J. M. Doyle, Review of Scientific Instruments **75**, 17 (2004).

[80] M. F. Ashby, in *Materials Selection in Mechanical Design* (Pergamon Press lnc., ADDRESS, 1992).

[81] E. D. Marquartdt, J. P. Le, and Ray Radebaugh, 11th International Cryocooler Conference (2000).

[82] Clark S. Lindsey, Runge-Kutta 2nd Order, `http://tinyurl.com/pfu82lv`.

[83] J. B. Hasted, *Physics of Atomic Collisions* (Elsevier, New York, ADDRESS, 1972).

[84] Nathaniel Brahms, Ph.D. thesis, Harvard University, 2008.

[85] Alisdair O. G. Wallis and Jeremy M. Hutson, Phys. Rev. Lett. **103**, 183201 (2009).

[86] Manuel Lara, John Bohn, Daniel Potter, Pavel Soldán, and Jeremy Hutson, Phys. Rev. A **75**, 012704 (2007).

[87] T. V. Tscherbul, J. Kłos, and A. A. Buchachenko, Phys. Rev. A **84**, 040701 (2011).

[88] R. V. Krems, A. Dalgarno, N. Balakrishnan, and G. C. Groenenboom, Physical Review A **67**, 060703 (2003).

[89] Vijay Singh, Kyle S. Hardman, Naima Tariq, Mei-Ju Lu, Aja Ellis, Muir J. Morrison, and Jonathan D. Weinstein, Phys. Rev. Lett. **108**, 203201 (2012).

[90] Scott Nguyen, Ph.D. thesis, Harvard University, 2006.

[91] V. Zhelyazkova, A. Cournol, T. E. Wall, A. Matsushima, J. J. Hudson, E. A. Hinds, M. R. Tarbutt, and B. E. Sauer, laser cooling and slowing of CaF molecules, arXiv:1308.0421 (2013) (unpublished).

[92] B. Hemmerling, G. K. Drayna, E. Chae, A. Ravi, and J. M. Doyle, arXiv:1310.3239 [physics.atom-ph] (unpublished).

[93] Marina Pelegrini, Ciro S. Vivacqua, Orlando Roberto-neto, Fernando R. Ornellas, and Francisco B. C. Machado, Brazilian Journal of Physics **35**, 950 (2005).

[94] N. Stone, Atomic Data and Nuclear Data Tables **90**, 75 (2005).

[95] Martin Zeppenfeld, Barbara G. U. Englert, Rosa Glöckner, Alexander Prehn, Manuel Mielenz, Christian Sommer, Laurens D. van Buuren, Michael Motsch, and Gerhard Rempe, Nature **491**, 570 (2012).

[96] Dipankar Das and Vasant Natarajan, Physical Review A **75**, 052508 (2007).

[97] Dipankar Das and Vasant Natarajan, J. Phys. B: At. Mol. Opt. Phys. **40**, 035001 (2008).

[98] K. G. Libbrecht, R. A. Boyd, P. A. Willems, T. L. Gustavson, and D. K. Kim, American Journal of Physics **63**, 729 (1995).

[99] Alexandre Faure, Krzysztof Szalewicz, and Laurent Wiesenfeld, The Journal of chemical physics **135**, 024301 (2011).

[100] Carmen M. Tesch and Regina de Vivie-Riedle, Physical Review Letters **89**, 157901 (2002).

[101] M. G. Kozlov, Physical Review A **87**, 032104 (2013).

[102] T. V. Tscherbul, T. A. Grinev, H.-G. Yu, A. Dalgarno, Jacek Kłos, Lifang Ma, and Millard H. Alexander, The Journal of chemical physics **137**, 104302 (2012).

[103] T. V. Tscherbul, H.-G. Yu, and A. Dalgarno, Physical Review Letters **106**, 073201 (2011).

[104] H. L. Bethlem, G. Berden, F. M. H. Crompvoets, R. T. Jongma, A. J. A. van Roij, and G. Meijer, Nature **406**, 491 (2000).

[105] T. Rieger, T. Junglen, S. A. Rangwala, P. W. H. Pinkse, and G. Rempe, Physical Review Letters **95**, 173002 (2005).

[106] Peter F. Bernath, Science **254**, 665 (1991).

[107] Robert C. Hilborn, Zhu Qingshi, and David O. Harris, J. Mol. Spectrosc. **97**, 73 (1983).

[108] Nathan Brahms, Timur V. Tscherbul, Peng Zhang, Jacek Kłos, Robert C. Forrey, Yat Shan Au, Hossein R. Sadeghpour, Alex Dalgarno, John M. Doyle, and Thad G. Walker, Phys. Chem. Chem. Phys. **13**, 19125 (2011).

[109] Jun Nakagawa, Richard F. Wormsbecher, and David O. Harris, J. Mol. Spectrosc. **97**, 37 (1983).

[110] T. C. Steimle, D. A. Fletcher, K. Y. Jung, and C. T. Scurlock, J. Chem. Phys. **96**, 2556 (1992).

[111] Etay Lavert-Ofir, Sasha Gersten, Alon B Henson, Itamar Shani, Liron David, Julia Narevicius, and Edvardas Narevicius, New J. Phys. **13**, 103030 (2011).

[112] Marina Quintero-Pérez, Paul Jansen, Thomas E. Wall, Joost E. van den Berg, Steven Hoekstra, and Hendrick L. Bethlem, Physical Review Letters **110**, 133003 (2013).

[113] Ken Takase, Larry A. Rahn, David W. Chandler, and Kevin E. Strecker, New Journal of Physics **11**, 055033 (2009).

[114] David Patterson and John M. Doyle, slow, Continuous Beams of Large Gas Phase Molecules, In preparation (unpublished).